Spectator-Tagged Deeply Virtual Compton Scattering on Light Nuclei

W. R. Armstrong[†‡], J. Arrington, I. Cloët, A. Freese, K. Hafidi[†], M. Hattawy, S. Johnston, D. Potterveld, P. Reimer, S. Riordan, Z. Ye

Argonne National Laboratory, Lemont, IL 60439, USA

J. Ball, M. Defurne, M. Garçon, H. Moutarde, S. Procureur, F. Sabatié

CEA, Centre de Saclay, Irfu/Service de Physique Nucléaire, 91191 Gif-sur-Yvette, France

W. Cosyn

Department of Physics and Astronomy, Proeftuinstraat 86, Ghent University, 9000 Ghent, Belgium

M. Mazouz

Faculté des Sciences de Monastir, 5000 Tunisia

A. Accardi

Hampton University, Hampton, VA 23668, USA

J. Bettane, R. Dupré[†], M. Guidal, D. Marchand, C. Muñoz, S. Niccolai, E. Voutier

Institut de Physique Nucléaire, CNRS-IN2P3, Univ. Paris-Sud, Université Paris-Saclay, 91406 Orsay Cedex, France

K. P. Adhikari, J. A. Dunne, D. Dutta, M. L. Kabir, L. El Fassi, L. Ye

Mississippi State University, Mississippi State, MS 39762, USA

M. Amaryan, G. Charles, G. Dodge

Old Dominion University, Norfolk, VA 23529, USA

V. Guzey

Petersburg Nuclear Physics Institute, National Research Center "Kurchatov Institute",

[‡]Contact person
[†]Spokesperson

Gatchina, 188300, Russia

N. Baltzell, F. X. Girod, V. Kubarovsky, K. Park, S. Stepanyan

Thomas Jefferson National Accelerator Facility, Newport News, VA 23606, USA

B. Duran, S. Joosten, Z.-E. Meziani†, M. Paolone, M. Rehfuss, N. Sparveris

Temple University, Philadelphia, PA 19122, USA

F. Cao, K. Joo, A. Kim, N. Markov

University of Connecticut, Storrs, CT 06269, USA

S. Scopetta

Università di Perugia, INFN, Italy

B. McKinnon

University of Glasgow, Glasgow G12 8QQ, United Kingdom

W. Brooks, A. El-Alaoui

Universidad Técnica Federico Santa María, Valparaíso, Chile

S. Liuti

University of Virginia, Charlottesville, VA 22903, USA

D. Jenkins

Virginia Polytechnic Institute and State University, Blacksburg, VA 24061, USA

a CLAS Collaboration Proposal

Jefferson Lab PAC 45

Nuclear Exclusive and Semi-inclusive Measurements with a New CLAS12 Low Energy Recoil Tracker

ALERT Run Group[†]

EXECUTIVE SUMMARY

In this run group, we propose a comprehensive physics program to investigate the fundamental structure of the ^{4}He nucleus. An important focus of this program is on the coherent exclusive Deep Virtual Compton Scattering (DVCS) and Deep Virtual Meson Production (DVMP) with emphasis on ϕ meson production. These are particularly powerful tools enabling model-independent nuclear 3D tomography through the access of partons' position in the transverse plane. These exclusive measurements will give the chance to compare directly the quark and gluon radii of the helium nucleus. Another important measurement proposed in this program is the study of the partonic structure of bound nucleons. To this end, we propose next generation nuclear measurements in which low energy recoil nuclei are detected. The tagging of recoil nuclei in deep inelastic reactions is a powerful technique, which will provide unique information about the nature of medium modifications through the measurement of the EMC ratio and its dependence on the nucleon off-shellness. Finally, we propose to measure incoherent spectator-tagged DVCS on light nuclei (d, ^{4}He) where the observables are sensitive to the Generalized Parton Distributions (GPDs) of a quasi-free neutron for the case of the deuteron, and bound proton and neutron for the case of ^{4}He. The objective is to study and separate nuclear effects and their manifestation in GPDs. The fully exclusive kinematics provide a novel approach for studying final state interactions in the measurements of the beam spin asymmetries and the off-forward EMC ratio.

At the heart of this program is the Low Energy Recoil Tracker (ALERT) combined with the CLAS12 detector. The ALERT detector is composed of a stereo drift chamber for track reconstruction and an array of scintillators for particle identification. Coupling these two types of fast detectors will allow ALERT to be included in the trigger for efficient

[†]Contact Person: Kawtar Hafidi (kawtar@anl.gov)

background rejection, while keeping the material budget as low as possible for low energy particle detection. ALERT will be installed inside the solenoid magnet instead of the CLAS12 Silicon Vertex Tracker and Micromegas tracker. We will use an 11 GeV longitudinally polarized electron beam (80% polarization) of up to 1000 nA on a gas target straw filled with deuterium or ^{4}He at 3 atm to obtain a luminosity up to 6×10^{34} nucleon cm^{-2}s^{-1}. In addition we will need to run hydrogen and ^{4}He targets at different beam energies for detector calibration. The following table summarizes our beam time request:

Configurations	**Proposals**	**Targets**	**Beam time request**	**Beam current**	**Luminosity***
			days	nA	n/cm^2/s
Commissioning	All†	^{1}H, ^{4}He	5	Various	Various
A	Nuclear GPDs	^{4}He	10	1000	6×10^{34}
B	Tagged EMC & DVCS	^{2}H	20	500	3×10^{34}
C	All†	^{4}He	20	500	3×10^{34}
TOTAL			**55**		

*This luminosity value is based on the effective part of the target. When accounting for the target's windows, which are outside of the ALERT detector, it is increased by 60%.

†"All" includes the four proposals of the run group: Nuclear GPDs, Tagged EMC, Tagged DVCS and Extra Topics. Note that the beam time request is only driven by the three first proposals.

Abstract

The three-dimensional picture of quarks and gluons in the proton is set to be revealed through Deeply virtual Compton scattering while a critically important puzzle in the one-dimensional picture remains, namely, the origins of the EMC effect. Incoherent nuclear DVCS, i.e. DVCS on a nucleon inside a nucleus, can reveal the 3D partonic structure of the *bound nucleon* and shed a new light on the EMC effect. However, the Fermi motion of the struck nucleon, off-shell effects and final-state interactions (FSIs) complicate this parton level interpretation. We propose here a measurement of incoherent DVCS with a tagging of the recoiling spectator system (nucleus A-1) to systematically control nuclear effects. Through spectator-tagged DVCS, a fully detected final state presents a *unique opportunity* to systematically study these nuclear effects and cleanly observe possible modification of the nucleon's quark distributions.

We propose to measure the DVCS beam-spin asymmetries (BSAs) on ^{4}He and deuterium targets. The reaction $^4\mathrm{He}(e, e'\gamma\, p\, ^3\mathrm{H})$ with a fully detected final state has the rare ability to simultaneously quantify FSIs, measure initial nucleon momentum, and provide a sensitive probe to other nuclear effects at the parton level. The DVCS BSA on a (quasi-free) neutron will be measured by tagging a spectator proton with a deuteron target. Similarly, a bound neutron measurement detects a spectator ^{3}He off a ^{4}He target. These two observables will allow for a self-contained measurement of the neutron *off-forward EMC Effect*.

We will also measure the impact of final state interactions on incoherent DVCS when the scattered electron, the real photon, and the struck proton are detected in the final state. This will help understand the measurements performed on helium during the previous CLAS E-08-024 experiment and will allow better measurements of the same channel where both statistics and kinematic coverage are extended. The measurement of neutron DVCS by tagging the recoil proton from a deuterium target is highly complementary to the approved CLAS12 experiment E12-11-003 which will also measure quasi-free neutron DVCS by detecting the scattered neutron.

Contents

Abstract **5**

Preface to the PAC45 Edition **9**

Introduction **10**

1 Physics Motivations **13**
1.1 Nuclear Effects . . . 13
1.1.1 The EMC Legacy . . . 13
1.1.2 Measuring Medium Modified Nucleons . . . 14
1.1.3 Why *Tagged* DVCS? . . . 15
1.2 Generalized Parton Distributions . . . 16
1.2.1 Spin Sum Rule . . . 16
1.2.2 Polarized EMC Effect . . . 17
1.2.3 Models of Nuclear Effects . . . 18
1.3 Motivation Summary . . . 20

2 Formalism and Experimental Observables **23**
2.1 Deeply Virtual Compton Scattering . . . 23
2.1.1 DVCS Beam Spin Asymmetry . . . 26
2.2 Tagged DVCS Reactions . . . 27
2.2.1 n-DVCS with a ^{2}H Target . . . 27
2.2.2 n-DVCS and p-DVCS with a ^{4}He Target . . . 28

3 Experimental Setup **31**
3.1 The CLAS12 Spectrometer . . . 32
3.2 Available options for a Low Energy Recoil Detector . . . 33
3.2.1 CLAS12 Central Detector . . . 33
3.2.2 BONuS12 Radial Time Projection Chamber . . . 34
3.2.3 Summary . . . 35
3.3 Design of the ALERT Detector . . . 36
3.3.1 The Drift Chamber . . . 36

3.3.2 The Scintillator Array . . . 41
3.3.3 Target Cell . . . 43
3.4 Simulation of ALERT and reconstruction . . . 43
3.4.1 Simulation of ALERT . . . 45
3.4.2 Track Fitting . . . 46
3.4.3 Particle identification in ALERT . . . 46
3.5 Drift chamber prototype . . . 48
3.6 Technical contributions from the research groups . . . 51
3.6.1 Argonne National Laboratory and Temple University . . . 51
3.6.2 Institut de Physique Nucléaire d'Orsay . . . 52
3.6.3 Jefferson Laboratory . . . 52

4 Proposed Measurements **54**
4.1 Asymmetry Extraction Procedure . . . 54
4.2 Kinematic Coverage . . . 55
4.3 Projections . . . 58
4.3.1 Beam Spin Asymmetry Extraction . . . 58
4.3.2 Systematic Uncertainties . . . 66

5 Summary and Answers to PAC44 **67**
5.1 Answers to PAC44 issues . . . 67
5.2 Summary and Beam Time Request . . . 70
5.3 Relation to other experiments . . . 70

A The Kinematics of Spectator-Tagged DVCS **72**
A.1 Incoherent DVCS Kinematic Variables . . . 72
A.1.1 Experimentally Measured Variables . . . 72
A.1.2 Momentum Transfer . . . 74
A.1.3 $t_{\min}$ and $t_{\max}$ . . . 76
A.2 Plane Wave Impulse Approximation . . . 78
A.2.1 PWIA Definition . . . 78
A.2.2 FSI and Off-shellness . . . 79
A.2.3 Measuring Off-shellness in the PWIA . . . 79
A.2.4 Photon Energy as FSI Indicator . . . 80
A.3 Toy Model of FSIs . . . 82
A.3.1 Modeling the FSI . . . 82
A.3.2 Toy MC Results . . . 84
A.3.3 Concluding Remarks . . . 87

B DVCS Formalism **89**
B.1 Theory bound nucleon DVCS . . . 89

C Detailed Experimental Projections **97**
C.1 Kinematic Coverage 97
C.2 Projections for $\sin\phi$ harmonic of the BSA 98
C.2.1 Off-forward EMC Effect Ratio 99

Preface to the PAC 45 Edition

This proposal was submitted to the PAC44 and was deferred as part of the run group proposal. PAC44 raised a few issues that we specifically address in section 5.1. However, here we take a moment to comment on their concern regarding the final state interactions because it is directed at this proposal and not the whole run group.

The PAC44 was skeptical about the kinematic cuts which identify FSIs and our claim to unambiguously identify FSIs. Paraphrased, our initial statement, "we can unambiguously identify *FSI-free* kinematics in a model independent way", was revised to be: "we can unambiguously identify kinematics with *significant FSIs* in a model independent way." The main distinction is FSI-free kinematics will always require a model while the inverse is not necessarily true. The nuance being that kinematics which are identical to the plane wave impulse approximation result could have FSIs that must be modeled at the amplitude level.

In order to make clear our approach, this updated version of the proposal dedicates a new appendix (A) to the unique kinematic leverage that spectator-tagged DVCS affords in understanding FSIs. The reader is urged to read this section before Chapter 1 as it should clarify concerns in regard to the FSIs.

Introduction

Deeply virtual Compton scattering is widely used to extract information about the generalized parton distributions of the nucleon. Its usefulness comes from the fact that the final state photon does not interact strongly (at leading order), requiring no additional non-perturbative formation mechanism. That is, the process in which the active quark radiates a final state photon is well understood, therefore, it is very useful for extracting information about the unknown non-perturbative vertex shown in Figure 1.

The extracted GPDs offer a three dimensional picture of how quarks and gluons are distributed in the nucleon. DVCS measurements on the proton [1, 2, 3, 4] and neutron [5] have already begun to provide insight into this slowly developing picture of the nucleon, however, without a free neutron target a flavor separation will always require using a quasi-free neutron target bound in light nuclei such as deuterium or ^{3}He. Such an extraction requires control of numerous nuclear effects: Fermi motion, off-shellness of the nucleons, mean field modified nucleons, short-range correlations (SRC), and final-state interactions.

Most observables involving nuclear targets (*e.g.*, inclusive deep-inelastic scattering (DIS), tagged DIS, inclusive quasi-elastic, semi-inclusive nucleon knockout, and polarization transfer in quasi-elastic scattering) are sensitive to many of these nuclear effects. Some experiments have been conducted in such a way as to mitigate or provide some systematic control over the size of these effects [6, 7, 8]. However, as discussed in the next chapter, the very nature of each experiment often precludes control of one or more nuclear effect mentioned above. Therefore, it is difficult to unambiguously draw conclusions from these measurements as to whether a nucleon is modified in a nuclear environment.

Much like the DVCS observables' ability to cleanly access information about the GPDs, tagged incoherent DVCS analogously provides a method for cleanly extracting nuclear effects from the observables. In a fully exclusive reaction, the over-determined kinematics yield two measurements of the same momentum transfer (see Figure 1). Within the plane wave Born approximation (PWBA), the momentum transfer between the virtual and real photon is completely insensitive to FSIs. On the other side of the diagram, the momentum transfer

calculated between the initial and final nucleon is quite sensitive to FSIs under the assumption that the plane wave impulse approximation (PWIA) holds[1]. That is to say, any relative deviation between the two momentum transfers can be attributed to the breakdown of the PWIA. In this way we can identify the kinematics where FSIs are significant and where they are minimal. Unlike, fully exclusive quasi elastic knockout reactions, tagged DVCS has a unique opportunity to simultaneously probe nuclear effects at the parton level.

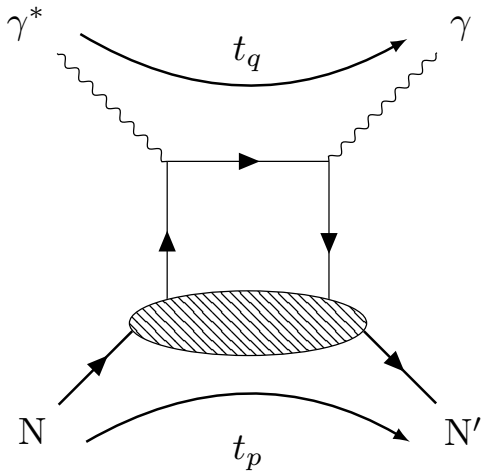

Figure 1: The DVCS handbag diagram showing the two ways the momentum transfer can be calculated. The hatched vertex represents the non-perturbative GPD.

Therefore, we propose to measure tagged DVCS beam spin asymmetries on two nuclear targets (^{2}H and ^{4}He) to unambiguously determine if the nucleon is modified in a nuclear environment. We will measure three beam spin asymmetries through tagged incoherent DVCS using two gas targets. The experiment requires the measurement of the three main processes:

1. $^4\mathrm{He} + \gamma^* \longrightarrow \gamma + p + {}^3\mathrm{H}$
2. $^4\mathrm{He} + \gamma^* \longrightarrow \gamma + (n) + {}^3\mathrm{He}$
3. $^2\mathrm{H} + \gamma^* \longrightarrow \gamma + (n) + p$

The first process provides a measurement of bound proton DVCS, but more importantly, by also detecting the final state proton, provides the over-determined kinematics needed to systematically probe the size of FSIs. This measurement is of critical importance to unwinding the nuclear effects when analyzing the last two processes, bound and quasi-free neutron DVCS, where the active nucleon (a neutron) goes undetected. A self-contained

[1]See appendix A for a detailed discussion of kinematics and the PWIA.

analysis of the nuclear effects on a neutron will be compared to a similar analysis of the proton. In addition to the proposed measured bound proton results, the latter will make use of previously measured results and already approved free proton DVCS [9, 10] experiments. In this way we will extract for both the proton and neutron an "off-forward EMC effect", *i.e.*, the ratio of a bound nucleon's off-forward structure function in ^{4}He to a free nucleon's off-forward structure function.

A large acceptance detector system capable of running at high luminosity along with the ability to detect or "tag" the low energy recoil spectator system is needed to perform such measurements. The ideal choice for this experiment is clearly CLAS12 augmented with *a low energy recoil tracker* (ALERT) that cleanly identifies the recoiling spectator system down to the lowest possible momentum. The ALERT detector consists of a small drift chamber that is insensitive to minimum ionizing particles, and a surrounding scintillator hodoscope that principally provides TOF information.

The outline of this proposal is as follows. Chapter one will provide a detailed motivation for the experiment. Chapter two will present the formalism and the observables we aim to measure. Chapter three presents a discussion of detector requirements, specifically, the detectors of CLAS12 and the need for a new low energy recoil recoil detector. Chapter four will discuss the experimental outputs, kinematic coverage, projected results, and required beam time for the proposed experiment. The first time reader is encouraged to first read the Appendix A which covers in detail the kinematics, PWIA, and FSIs.

Chapter 1

Physics Motivations

Before diving into the details of tagged incoherent DVCS, we will first explain why an understanding of the nature and origins of nuclear effects is important for determining the nucleon structure at the parton level. We will begin this chapter with a discussion of nuclear effects and the challenges they present to experiment. This is followed by a quick overview of GPDs and their importance to understand the partonic structure of nuclear matter. The kinematics of incoherent DVCS are discussed, highlighting the critical importance of the spectator tagging method. We will emphasize the unique opportunity tagged DVCS has to finally settle the more than three decades old question: *is the partonic structure of the nucleon modified in presence of a nuclear medium?*

1.1 Nuclear Effects

1.1.1 The EMC Legacy

Measurements of the longitudinal parton distribution functions (PDFs) with polarized beams and targets have provided a detailed one dimensional mapping of the quark distributions in the nucleon. QCD has been successful in describing the evolution of these distributions across scales differing by many orders of magnitude. The European Muon Collaboration not only observed the so-called "EMC effect", but they also created the poorly named "spin crisis". The EMC effect originates from their observation that the naive expectation of the quark distributions in nuclei, *i.e.*, they are the sum of the quark distributions for A free nucleons, was not observed [11]. However, consensus has yet to be reached in how to explain

this effect. The spin crisis began when it was discovered that the spin of the quarks only carry a small fraction of the nucleon's total spin. It was soon understood that, through the non-perturbative dynamics of QCD, the remaining angular momentum will likely come in the form of quark orbital angular momentum (OAM) and gluon angular momentum. The EMC experiments gave us a "crisis" that was quickly understood, and an empirical "effect" whose origins remain ambiguous more than 3 decades later.[1]

1.1.2 Measuring Medium Modified Nucleons

The EMC effect showed the possibility of medium modifications to the nucleon may be significant in deep inelastic scattering[2]. However, the degree to which these modifications can be cleanly studied in inclusive or semi-inclusive processes is made difficult by the possible presence of final state interactions. Furthermore, when considering the Fermi motion of a bound nucleon, there is a probability of finding a nucleon moving with large relative momenta which corresponds to a configuration where the two nucleons are separated by a small distance. By selecting these dense configurations through spectator tagging in hard processes, it is not unreasonable to expect sizable modifications relative to the mean field nucleons [12]. Therefore, knowing precisely the initial momentum of the struck nucleon is key for understanding the short and long range nuclear effects. Isolating the configuration space effects from the FSIs presents a significant obstacle to drawing a definitive conclusion about medium modifications.

Similar medium modifications are expected to manifest themselves in the elastic form factors of bound nucleons. Observation of saturation of the Coulomb sum rule (CSR), which is accessible through measurements of the longitudinal response function in quasi-elastic scattering off nuclei, has been debated for some time [13, 14]. An observed quenching of the sum rule would indicate that nucleons are modified in such a way that the net charge response of the parent nucleus is much more complicated than a simple sum of nucleons. Recent, QCD inspired theoretical work predicts a dramatic quenching of the sum rule [15]. Furthermore, observations of short range correlated nucleon pairs in knockout reactions have challenged us to confront our ignorance of the short-range part of the N-N potential.

While a consensus has yet to be reached in explaining the origins of and the connections between the EMC effect, short range correlations, and quenching of the Coulomb sum rule, medium modifications of the nucleon is expected to play an important role in these phenomena.

[1] In hindsight, perhaps the "EMC effect" should have been called the "EMC Crisis", and the "spin crisis" called the "EMC spin effect".

[2] Perhaps the earliest known medium modification of the nucleon is the free neutron lifetime compared to the significantly longer lifetime when bound in a nucleus.

1.1.3 Why *Tagged* DVCS?

DVCS is poised to provide some much needed contact between the EMC effect and short-range correlations. The two phenomena are observed through notably different processes but the connection between the inelastic and elastic observables is due to the properties of GPDs (see B.1). In the forward limit the GPDs reduce to the longitudinal parton distributions whose modification may explain the EMC effect, and in the off-forward case they reduce to the form factors, thus, describing elastic scattering off of the nucleon. Therefore, measurements of nucleon GPDs in nuclei will bridge the gap between these two processes and will shed light on the connections between the EMC effect and short range correlations. The sensitivity of the GPDs to medium modifications is a significant motivation, however, *tagged* incoherent DVCS provides an unprecedented handle on quantifying and systematically controlling the various nuclear effects.

First, let us consider the inclusive DIS measurements where only the scattered electron is detected and the exchanged virtual photon interacts at the parton level. The nucleon containing the struck quark may potentially be in a short-range correlated N-N pair, therefore, tagging the spectator system in the PWIA provides the experimental handle needed to compare the contributions to the EMC effect from SRC nucleons versus the nucleons in the mean field. This measurement is part of the "Tagged EMC" proposal found in the current proposal's run group. Here, FSIs are the principle challenge for this method which become amplified at larger initial nucleon momentum. The re-interaction of the spectator system (A-1) with hadronizing fragments (X) can alter the detected momentum of the spectator system. Therefore model calculations have to be used to explore kinematics where FSIs can minimized [16].

Similarly, for inclusive quasi-elastic scattering we would like to measure the nucleon elastic form factor modifications associated with the SRC and the mean-field nucleons. Therefore, by detecting the knockout nucleon or a spectator recoil, the initial nucleon's momentum can be determined (within the PWIA). If both are detected, the over-determined kinematics allow for a second calculation of the momentum transfer. However, for large nuclei the possibility of detecting the full (A-1) recoil system becomes nearly impossible. Furthermore, FSIs in the form of meson exchange currents (MEC) can become rather troublesome even for measurements of induced polarization in quasi-elastic knock-out reactions. Therefore, again, we find an explicit model dependence spoiling the interpretation of medium modifications.

Finally, incoherent DVCS has a unique combination characteristics found in DIS and quasi-elastic scattering that make it the ideal process for exploring nuclear effects. Like both processes, tagging the recoil spectator system serves to identify and separate the mean field (low momentum) nucleons from the SRC (high momentum) nucleons. Similar to DIS, DVCS has a parton level interpretation, and like elastic scattering the process is exclusive. The latter

property allows for systematic control of the FSIs through the redundant measurement of the momentum transfer, t. Therefore, tagged incoherent DVCS provides a *model independent* method for studying and accounting for final state interactions while providing an observable that is uniquely sensitive to the medium modifications.

1.2 Generalized Parton Distributions

1.2.1 Spin Sum Rule

By studying the "off-forward parton distributions", Ji derived a sum rule [17] which is a gauge invariant decomposition of the nucleon spin. It relates integrals of the GPDs to the quark total angular momentum and is written as

$$J_q = \frac{1}{2}\int dx\, x \left[H_q(x,\xi,t=0;Q^2) + E_q(x,\xi,t=0;Q^2)\right] \tag{1.1}$$

where the H_q and E_q are the leading-twist chiral-even quark GPDs. An identical expression for the total gluon orbital angular momentum is obtained using the two gluon GPDs, H_g and E_g. The total nucleon spin is simply written as

$$\frac{1}{2} = \sum_q J_q + J_g, \tag{1.2}$$

where the sum is over light quarks and anti-quarks. A topic of heavy discussion over the past five years or so has been about the decomposition of the nucleon spin. Ji showed that the gluon angular momentum cannot be broken into spin and orbital in a gauge invariant way, however, the quark can. In fact, the polarized PDFs provide the quark spin contribution in the forward limit

$$\Delta\Sigma_q(Q^2) = \int dx\, x\, \tilde{H}_q(x,\xi=0,t=0;Q^2) \tag{1.3}$$

where $\Delta\Sigma_q$ is the integral of the polarized PDF Δq. Therefore, we arrive at an expression for the quark OAM

$$L_q = J_q - \frac{1}{2}\Delta\Sigma_q \tag{1.4}$$

which, through equations 1.1 and 1.3, is a function of the quark GPDs E, H, and $\tilde{H}$.

The GPDs of the up and down quarks can be extracted from measurements on the neutron

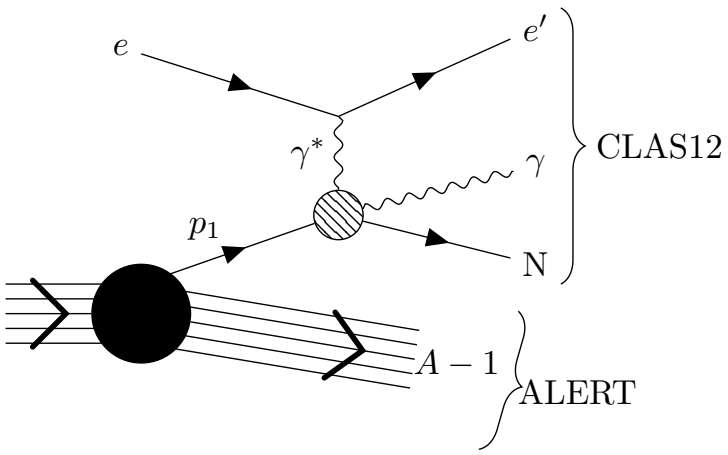

Figure 1.1: Tagged DVCS diagram showing the detection of the forward DVCS final state particles in CLAS12 and the detection of the recoiling spectator system (A-1) in ALERT. The hatched circle represents the hard DVCS process.

and proton using isospin symmetry

$$F_u = \frac{3}{5}\left(4F^p - F^n\right) \tag{1.5}$$

$$F_d = \frac{3}{5}\left(4F^n - F^p\right) \tag{1.6}$$

where $F \in [H, E, \tilde{H}, \tilde{E}]$. The flavor separation is straight forward if equal data on the proton and neutron GPDs are available. However, clean neutron data are not available due to a non-existent free-neutron target, and when neutron measurements are made using nuclear targets they suffer from a variety of nuclear effects previously discussed. Part of the proposed experiment would provide a precise neutron measurement from deuteron with a technique similar to the one used by the BoNuS experiment[3] to extract the neutron structure function at high x [18, 19].

1.2.2 Polarized EMC Effect

Using polarized nuclear targets, the polarized EMC effect can be measured and is predicted to be larger than the "unpolarized" EMC effect [20]. The polarized EMC effect is measured through the ratio of spin structure functions g_1 of a bound nucleon to that of a free nucleon. DIS measurements typically require both a longitudinally polarized target and longitudinally polarized beam to measure g_1. The $\sin\phi$ harmonic of the neutron DVCS beam

[3]BoNuS stands for "Barely off-shell Nucleon Structure".

spin asymmetry is

$$A_{LU,n}^{\sin\phi} \propto \mathrm{Im}(F_1^n \mathcal{H}^n - \frac{t}{4M^2} F_2^n \mathcal{E}^n + \frac{x_B}{2}(F_1 + F_2)^n \tilde{\mathcal{H}}^n) \ . \tag{1.7}$$

The first term is suppressed by F_1^n and if for the moment we neglect the $\mathcal{E}$ term, the ratio of this asymmetry for a bound neutron to a free neutron is

$$R_{AL,n}^{\sin\phi} = \frac{A_{LU,n^*}^{\sin\phi}}{A_{LU,n}^{\sin\phi}} \simeq \frac{G_M^{n^*}(t)}{G_M^n(t)} \frac{\mathrm{Im}(\tilde{\mathcal{H}}^{n^*}(\xi,\xi,t))}{\mathrm{Im}(\tilde{\mathcal{H}}^n(\xi,\xi,t))} \tag{1.8}$$

which in the forward limit becomes

$$R_{AL,n}^{\sin\phi} \longrightarrow \frac{\mu_{n^*}}{\mu_n} \frac{g_1^{n^*}(x)}{g_1^n(x)} \ , \tag{1.9}$$

where μ_{n^*}/μ_n is the ratio of the bound neutron magnetic moment to the free neutron magnetic moment, and $g_1^{n^*}/g_1^n$ is similarly the ratio of the bound to free neutron spin structure functions.

Equations 1.8 and 1.9 are rather interesting for a few reasons. First, they can be used to draw conclusions about the behavior of the *polarized* quark distributions in unpolarized nuclei without using a polarized target. But we must note the unjustified neglect of the $\mathcal{E}^n$ term which complicates subsequent analysis. We point out this term in the ratio of Equation 1.8 because it highlights the observable's sensitivity to medium modifications. Specifically noting that a modification to the nucleon's static properties, such as, anomalous magnetic moment or polarization-dependent transverse-charge distribution (see [21]), would also manifest themselves through the magnetic form factor whose ratio also appears in this observable.

Also, a measurement of the BSA in Equation 1.7 will provide important model constraints on the GPD E^n and measurements of the ratio with ^{4}He would further constrain nuclear GPD models. This is particularly motivating in the context of Equation 1.1, where E^n is clearly an important quantity for understanding the quark orbital angular momentum.

1.2.3 Models of Nuclear Effects

To understand the potential sources of observable nuclear effects, we take the ratio of beam spin asymmetries for a bound nucleon to that on the free nucleon target. Here we discuss just two models that make very different predictions for similar ratios based on the presumed sources of the nuclear effects.

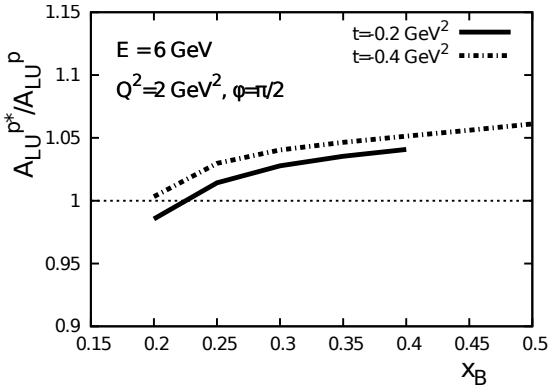

Figure 1.2: Beam spin asymmetry ratio of a bound proton to a free proton. Reproduced from [22].

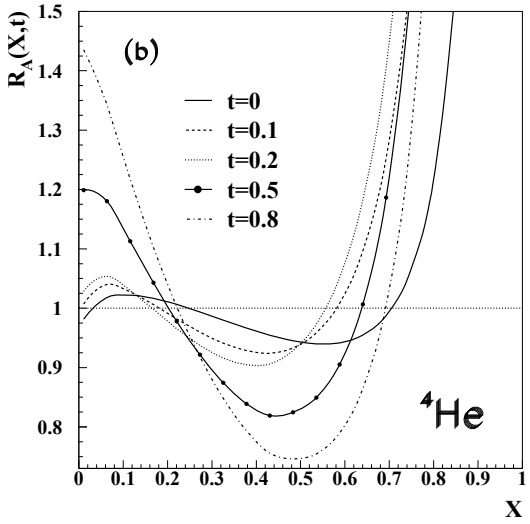

Figure 1.3: Predictions for the ratio given in equation 1.10. Reproduced from [23].

First, predictions for the ratio of beam spin asymmetry at 6 GeV are shown in Figure 1.2, which shows the bound proton beam spin asymmetry, $A_{LU}^{p^*}$, to the free proton A_{LU}^{p} [22]. These calculations use the medium modified GPDs as calculated from the quark-Meson coupling model. However, they do not include FSIs and predict their contribution is at most a few percent. In another calculation, Liuti et al. [23, 24] use a realistic spectral function and consider off-shell effects. This is a more traditional approach to explaining differences in a bound nucleon. They make predictions for the ratio

$$R_A(x, \xi = 0, t) = \frac{H_A(x, \xi = 0, t) F_N(t)}{H_N(x, \xi = 0, t) F_A(t)} \tag{1.10}$$

which is shown in Figure 1.3. For more discussions of modeling nuclear effects see [25, 26].

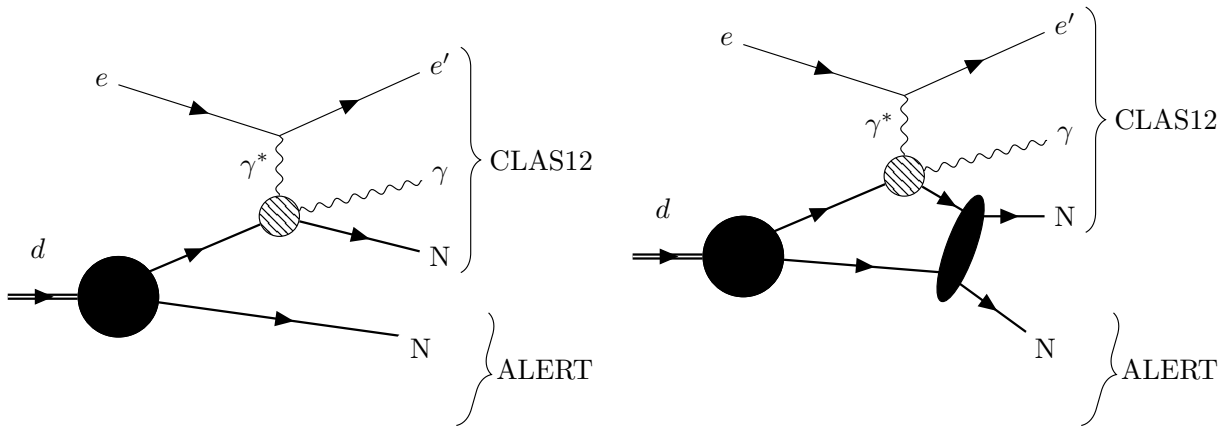

Figure 1.4: PWIA diagram for incoherent DVCS on the deuteron (left) and with the inclusion of final state interactions (right).

It is clear that the role of off-shellness, and final state interactions in nuclei needs to be better understood if we are to conclude that the nucleon structure is modified by the nuclear medium. With spectator tagging, we will be able to test these models over a broad range of spectator momentum and angles. This tagging technique can be used as a knob to tune the effect of final state interactions and either maximized or minimized it.

To understand the regions where FSIs are expected to be significant, we first look at the deuteron. Consider the quasi-elastic scattering on a quasi-free nucleon as shown in Figure 1.4. Measurements of the cross section as a function of missing momentum are shown in Figure 1.5 along with model calculations in PWIA with different final state interactions. From model calculations it was found that the PWIA was insufficient for describing the data at missing momenta above 300 MeV/c. Similarly, the size of the FSI strength as a function of spectator momentum (left) and angle relative to the momentum transfer, θ_s, (right) is shown in Figure 1.6 [28, 16]. At low recoil momentum and backwards spectator angle, the FSIs are negligible, where at high momenta perpendicular to the momentum transfer, the FSIs are maximized.

1.3 Motivation Summary

In summary, we propose to perform the following key measurements using CLAS12 and ALERT for the low energy spectator recoil tagging:

- *Bound proton DVCS* with a ^{4}He target where the final state is fully detected by tagging a spectator ^{3}H and the struck proton is detected in CLAS12. The PWIA will be tested

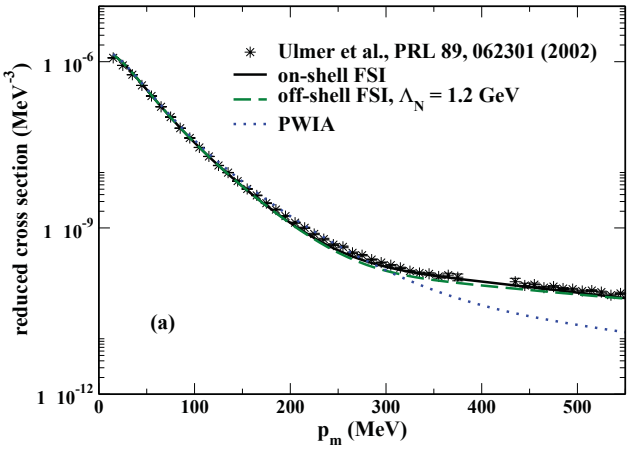

Figure 1.5: Reduced quasi-elastic scattering cross section on deuteron. Reproduced from [27]. The reduced cross section includes a term multiplying the cross section by $M_d f_{\rm rec}/(\sigma_{\rm Mott} m_p m_n p_p)$, where the $f_{\rm rec}$ is the recoil factor, and $\sigma_{\rm Mott}$ is the Mott cross section. See reference [27] for more details.

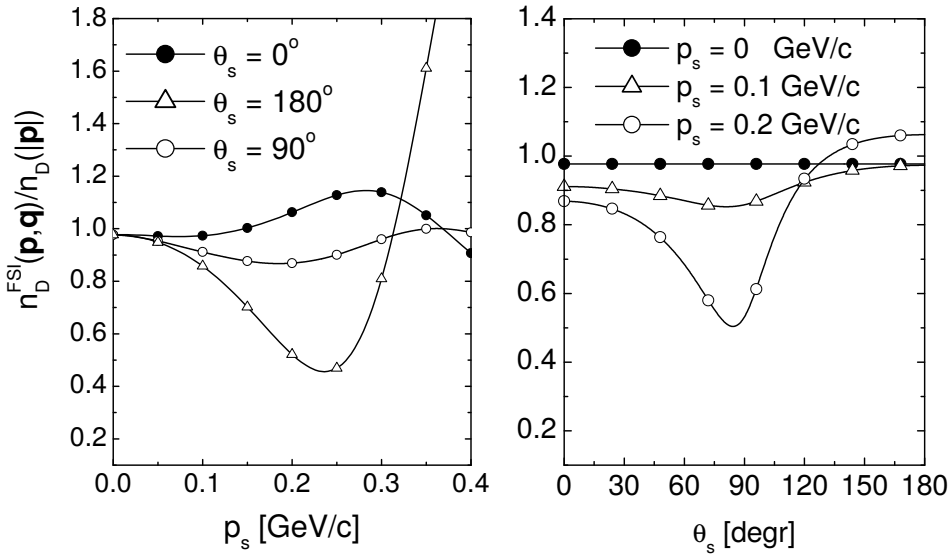

Figure 1.6: Ratio of cross sections for the FSI model from [28] to PWIA calculation as a function of the spectator momentum (left) and spectator angle (right).

by the redundant measurement of the momentum transfer as explained above and in great detail in appendix A. Thus, kinematics with significant FSIs are identified in a completely *model independent* way.

- *Bound neutron DVCS* with a ^{4}He target where the neutron goes undetected and the spectator ^{3}He is detected in ALERT. Using the same kinematics identified in the previous measurement, and using iso-spin (charge) symmetry, we can conclude that the struck neutron feels the same final state interactions as the struck proton.

- *Quasi-free neutron DVCS* with a ^{2}H target where the recoil proton is tagged and the struck neutron goes undetected.

Chapter 2

Formalism and Experimental Observables

2.1 Deeply Virtual Compton Scattering

The cross section for DVCS on a spin-1/2 target can be parameterized in terms of four helicity conserving GPDs: H^q, E^q, $\tilde{H}^q$, and $\tilde{E}^q$. For spin-0 targets, such as ^{4}He, the cross section is parameterized with just one helicity conserving GPD [29]. For spin-1 targets like the deuteron, the cross section is parameterized with nine GPDs [30, 31].

The DVCS cross section is written as

$$\frac{d\sigma}{dx_A\, dy\, dt\, d\phi\, d\varphi} = \frac{\alpha^3 x_A y}{16\pi^2 Q^2 \sqrt{1+\varepsilon^2}} \left|\frac{\mathcal{T}}{e^3}\right|^2 \tag{2.1}$$

where

$$\varepsilon \equiv 2x_A \frac{M_A}{Q}, \tag{2.2}$$

$x_A = Q^2/(2p_1 \cdot q_1)$ is the scaling variable, $y = (p_1 \cdot q_1)/(p_1 \cdot k_1)$ is the photon energy fraction, ϕ is the angle between the leptonic and hadronic planes, φ is the scattered electron's azimuthal angle, $Q^2 = -q_1^2$, and $q_1 = k_1 - k_2$. The particle momentum definitions are shown in Figure 2.1. We use the BMJ[1] convention [32, 33, 34, 35] for defining the momentum transfer where the target nucleus is initially at rest, $\Delta = p_1 - p_2$ and $t = \Delta^2$. The Bjorken variable

[1]The Belitsky, Müller, and Ji reference frame. See [32] for a nice discussion of the various reference frames.

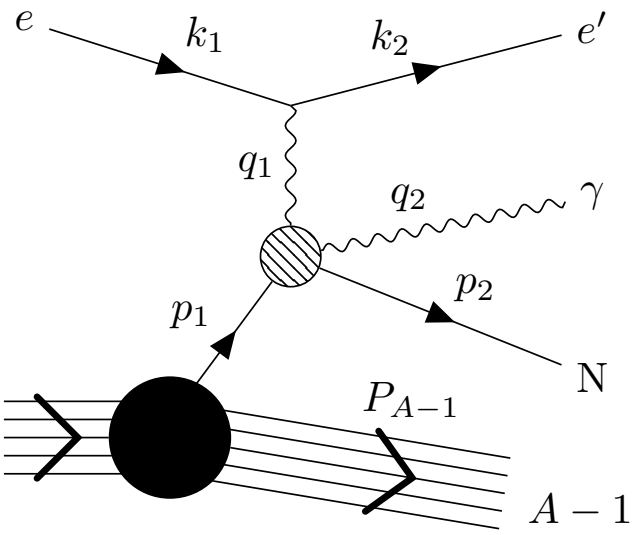

Figure 2.1: Incoherent DVCS process with the momentum definitions labeled.

is related to the scaling variable by

$$x_{\mathrm{B}} = \frac{Q^2}{2M_N E\, y} \simeq A x_A \tag{2.3}$$

where M_N is the nucleon mass and E is the beam energy. Another scaling variable called skewedness is

$$\xi = \frac{x_A}{2 - x_A} + \mathcal{O}(1/Q^2) \tag{2.4}$$

where the power suppressed contributions originate with the selection of the BMJ frame convention needed to unambiguously define the leading-twist approximation used in this proposal [32].

The amplitude is the sum of the DVCS and Bethe-Heitler (BH) amplitudes, and when squared has terms

$$\mathcal{T}^2 = |\mathcal{T}_{\mathrm{BH}}|^2 + |\mathcal{T}_{\mathrm{DVCS}}|^2 + \mathcal{I} \tag{2.5}$$

where the first is the BH contribution, the second is the DVCS part, and the last term is the interference part,

$$\mathcal{I} = \mathcal{T}_{\mathrm{DVCS}}\mathcal{T}^*_{\mathrm{BH}} + \mathcal{T}^*_{\mathrm{DVCS}}\mathcal{T}_{\mathrm{BH}}. \tag{2.6}$$

The corresponding amplitudes are calculated with the diagrams shown in Figure 2.2. The details of contracting the DVCS tensor with various currents and tensors can be found in [31]. The resulting expressions for the amplitudes are

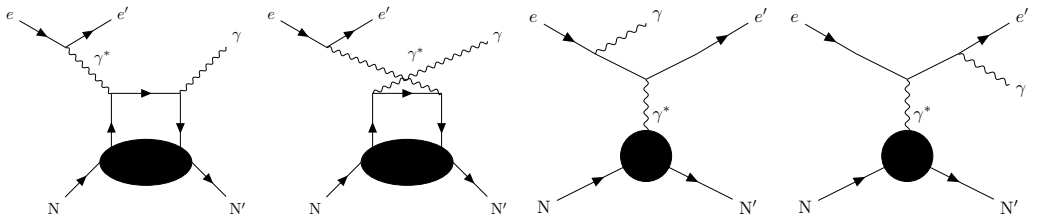

Figure 2.2: DVCS handbag diagram and BH contributions used for calculating DVCS amplitudes.

$$|\mathcal{T}_{\rm BH}|^2 = \frac{e^6(1+\varepsilon^2)^{-2}}{x_A^2\, y^2\, t\, \mathcal{P}_1(\phi)\mathcal{P}_2(\phi)} \left\{ c_0^{\rm BH} + \sum_{n=1}^{2} \left[c_n^{\rm BH} \cos(n\phi) + s_n^{\rm BH} \cos(n\phi) \right] \right\} \tag{2.7}$$

$$|\mathcal{T}_{\rm DVCS}|^2 = \frac{e^6}{y^2\, Q^2} \left\{ c_0^{\rm DVCS} + \sum_{n=1}^{2} \left[c_n^{\rm DVCS} \cos(n\phi) + s_n^{\rm DVCS} \cos(n\phi) \right] \right\} \tag{2.8}$$

$$\mathcal{I} = \frac{e^6(1+\varepsilon^2)^{-2}}{x_A\, y^3\, t\, \mathcal{P}_1(\phi)\mathcal{P}_2(\phi)} \left\{ c_0^{\mathcal{I}} + \sum_{n=1}^{3} \left[c_n^{\mathcal{I}} \cos(n\phi) + s_n^{\mathcal{I}} \cos(n\phi) \right] \right\} \tag{2.9}$$

The functions c_0, c_n, and s_n are called *Fourier coefficients* and they depend on the kinematic variables and the operator decomposition of the DVCS tensor for a target with a given spin. At leading twist there is a straightforward form factor decomposition which relates the vector and axial-vector operators with the so-called Compton form factors (CFFs) [36]. The Compton form factors appearing in the DVCS amplitudes are integrals of the type

$$\mathcal{F} = \int_{-1}^{1} dx F(\mp x, \xi, t) C^{\pm}(x, \xi) \tag{2.10}$$

where the coefficient functions at leading order take the form

$$C^{\pm}(x,\xi) = \frac{1}{x - \xi + i\varepsilon} \pm \frac{1}{x + \xi - i\varepsilon}. \tag{2.11}$$

We plan on measuring the beam spin asymmetry as a function of ϕ

$$A_{LU}(\phi) = \frac{d\sigma^{\uparrow}(\phi) - d\sigma^{\downarrow}(\phi)}{d\sigma^{\uparrow}(\phi) + d\sigma^{\downarrow}(\phi)} \tag{2.12}$$

where the arrows indicate the electron beam helicity.

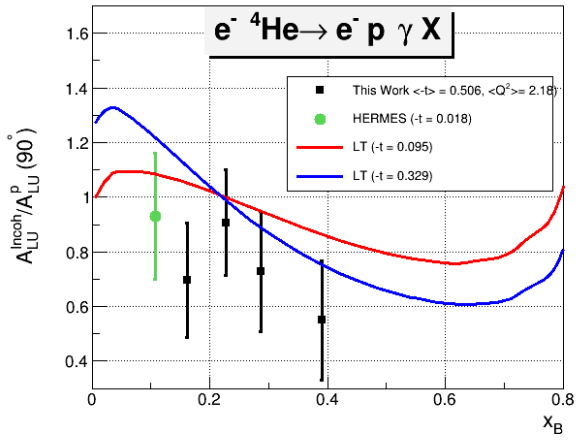

Figure 2.3: The beam spin asymmetry from eg6 [38] and HERMES along with models from Liuti and Taneja [39].

2.1.1 DVCS Beam Spin Asymmetry

Through the Bethe-Heitler dominance of the first sine harmonic of the beam spin asymmetry

$$A_{LU}^{\sin\phi} = \frac{1}{\pi}\int_{\pi}^{\pi} d\phi \sin\phi A_{LU}(\phi) \tag{2.13}$$

is proportional to the following combination of Compton form factors [37]

$$A_{LU}^{\sin\phi} \propto \mathrm{Im}(F_1\mathcal{H} - \frac{t}{4M^2}F_2\mathcal{E} + \frac{x_B}{2}(F_1+F_2)\tilde{\mathcal{H}}) \tag{2.14}$$

which is dominated by $\mathrm{Im}(\mathcal{H})$ for the proton, and dominantly sensitive to $\mathrm{Im}(\mathcal{E})$ and $\mathrm{Im}(\tilde{\mathcal{H}})$ for the neutron.

Recent measurement [38] of incoherent DVCS by the CLAS collaboration conducted during the 6 GeV era (E08-024) have indeed shown significant modification of the proton beam spin asymmetry in ^{4}He without the possibility to decipher between the nuclear effects presented above. These results are shown in Figure 2.3. In these measurements the SRC and mean field nucleons are not separated and the FSIs remain unchecked.

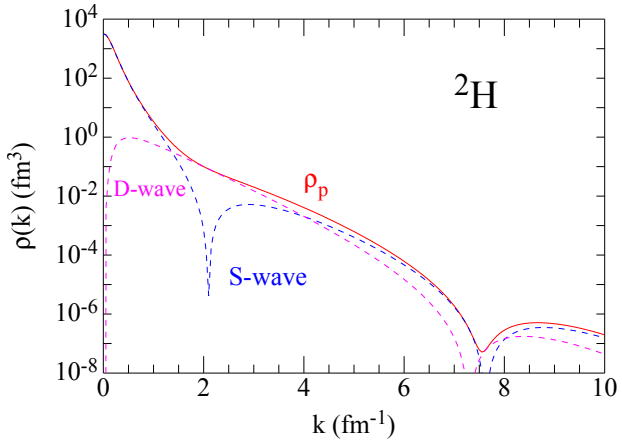

Figure 2.4: The total proton momentum distribution in the deuteron is shown by the red solid line; the contribution from S-wave and D-wave components are shown separately by blue and magenta dashed lines. [40]

2.2 Tagged DVCS Reactions

The ALERT detector combined with CLAS12 provides a unique opportunity to measure incoherent exclusive processes on light nuclei. As mentioned in the previous chapters, tagging low momentum spectator recoils in exclusive knockout reactions provides the experimental leverage needed to separate and cleanly study a variety of nuclear effects.

Neutron DVCS (n-DVCS) is of immediate interest as it is needed to do a flavor separation of the GPDs. We propose to measure tagged n-DVCS on ^{2}H and ^{4}He targets starting at $P_{A-1} \simeq 70$ MeV/c for tagged protons and $P_{A-1} \simeq 120$ MeV/c for ^{3}He ions. The momentum densities for these targets can be seen in Figure 2.4 and Figure 2.5.

2.2.1 n-DVCS with a ^{2}H Target

Previous measurements of n-DVCS using a deuteron target required subtracting a proton contribution from the total deuteron yields [5] and assumed the validity of the PWIA. The yield for the neutron and coherent deuteron can not be separated and the subtraction yields the resulting beam spin asymmetry of the combination

$$D(\vec{e}, e'\gamma)X - H(\vec{e}, e'\gamma)X = d(\vec{e}, e'\gamma)d + n(\vec{e}, e'\gamma)n + ... \tag{2.15}$$

which is fit with the CFFs of the neutron and deuteron as free parameters. This procedure has a few downsides: it requires a bin by bin equivalent proton measurement which is highly

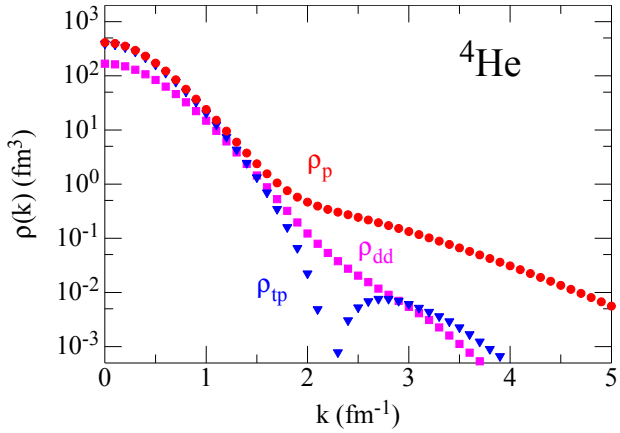

Figure 2.5: The proton momentum distribution in ^{4}He is shown by the red circles; the tp cluster distribution is shown by the blue triangles and the dd cluster distribution is shown by the magenta squares. [40]

prone to systematic effects, the undetected spectator system or struck nucleon leaves the center-of-momentum energy, $\sqrt{s}$, undetermined, and FSI remain unchecked.

We propose to measure the recoiling spectator proton, thus, measuring $\sqrt{s}$ for every event. Furthermore, the reconstructed missing momentum can be used to check for significant final state interactions (see appendix A). Comparing t calculated from the virtual and real photon momenta to t calculated using the reconstructed missing momentum of the neutron (after selection cuts),

$$t_q = (q_1 - q_2)^2 \tag{2.16}$$

can provide a measure of the presence of significant final state interactions.

2.2.2 n-DVCS and p-DVCS with a ^{4}He Target

A helium target provides the unique opportunity to again measure the neutron DVCS beam spin asymmetry, however, now on a bound nucleon with unprecedented control over final state interactions. Through the two reactions $^4\mathrm{He}(e, e'\gamma\, p\, ^3\mathrm{H})$ and $^4\mathrm{He}(e, e'\gamma\, ^3\mathrm{He})n$ the ratios

$$R_n = \frac{A_{LU}^{n^*}}{A_{LU}^{n}} \tag{2.17}$$

$$R_p = \frac{A_{LU}^{p^*}}{A_{LU}^{p}} \tag{2.18}$$

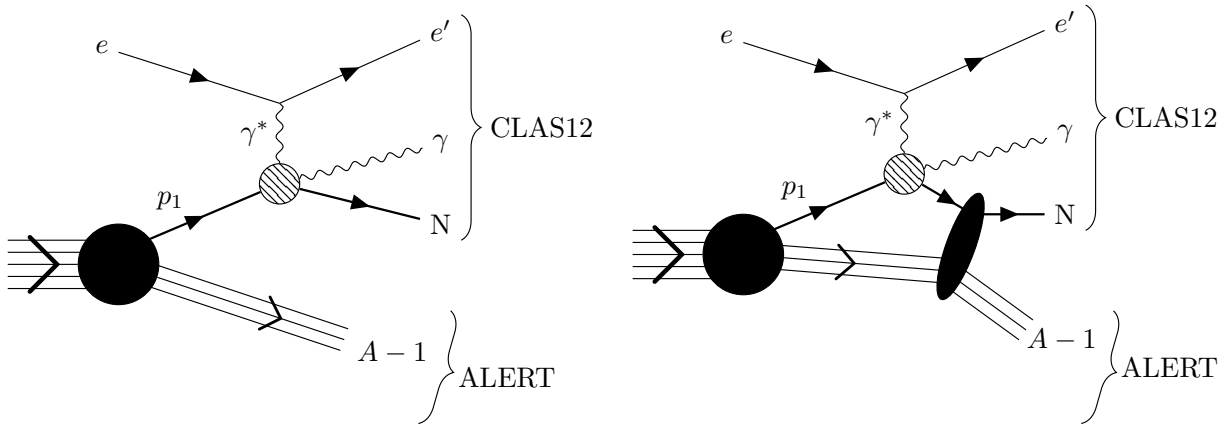

Figure 2.6: Incoherent DVCS on a nuclear target without (left) and with (right) final state interactions.

can provide the leverage needed to definitively make a statement on medium modifications.

The proton BSA will be measured by fully detecting the final state; the struck proton will be detected in CLAS12 and the recoiling spectator ^{3}H will be detected in ALERT. The neutron BSA will be measured by tagging a recoil ^{3}He and without detecting the struck neutron. Exclusivity cuts will ensure the n-DVCS event is cleanly selected. The free proton BSA measurement in Equation 2.17 will be taken from the already approved JLab measurements [9, 10], while the neutron BSA will come from the deuteron target measurement discussed above. The neutron measurement will have the extra advantage of experimental systematics canceling in the ratio because both asymmetries will be measured using the same apparatus.

Finally, we consider the fully exclusive proton DVCS reaction where a recoil triton is detected as $\boldsymbol{P}_{A-1} = -\boldsymbol{p}_1$. The fully detected final state kinematics present an opportunity to test the PWIA[2]. One way is to use the two momentum transfers, t_q (Equation 2.16) and

$$t_p = (p_1 - p_2)^2, \tag{2.19}$$

which must be the same, i.e., $\delta t = t_q - t_p = 0$. If a FSI occurs between the spectator and the struck nucleon (Figure 1.4), such as pion exchange, δt can be non-zero depending which over-determined kinematic variables we choose to use (or not use). The reader is referred to appendix A for a thorough discussion of this point. By selecting events where $\delta t \simeq 0$, within the detector resolutions, we can be sure that significant final state interactions have not occurred. These are events that may contain FSIs that are kinematically indistinguishable from the PWIA, but which have an amplitude level influence on the cross section. Alternatively, requiring the missing momentum to be back-to-back with the recoil spectator provides a cut

[2]Please see appendix A for a more detailed explanation.

which is expected to reduce final state interactions.

With the final state interactions well under control in the proton DVCS channel, charge symmetry suggests that, for the same kinematics, they will be similarly understood in the neutron channel. That is the FSIs are assumed to follow charge symmetry. Therefore, the proton DVCS BSA measurement on ^{4}He is crucial for measuring in a model independent way the validity of the PWIA and mapping the FSIs for the mirror neutron measurement.

Chapter 3

Experimental Setup

All the different measurements of the ALERT run group require, in addition to a good scattered electron measurement, the detection of low energy nuclear recoil fragments with a large kinematic coverage. Such measurements have been performed in CLAS (BONuS and eg6 runs), where the adequacy of a small additional detector placed in the center of CLAS right around the target has shown to be the best solution. We propose here a similar setup using the CLAS12 spectrometer augmented by a low energy recoil detector.

We summarize in Table 3.1 the requirements for the different experiments proposed in the run group. By comparison with previous similar experiments, the proposed tagged measurements necessitate a good particle identification. Also, CLAS12 will be able to handle higher luminosity than CLAS so it will be key to exploit this feature in the future setting in order to keep our beam time request reasonable.

Measurement	Particles detected	p range	θ range
Nuclear GPDs	^{4}He	$230 < p < 400 MeV/c$	$\pi/4 < \theta < \pi/2$ rad
Tagged EMC	p, ^{3}H, ^{3}He	As low as possible	As close to π as possible
Tagged DVCS	p, ^{3}H, ^{3}He	As low as possible	As close to π as possible

Table 3.1: Requirements for the detection of low momentum spectator fragments of the proposed measurements.

This chapter will begin with a brief description of CLAS12. After presenting the existing options for recoil detection and recognize that they will not fulfill the needs laid out above, we will describe the design of the proposed new recoil detector ALERT. We will then present the reconstruction scheme of ALERT and show the first prototypes built by our technical

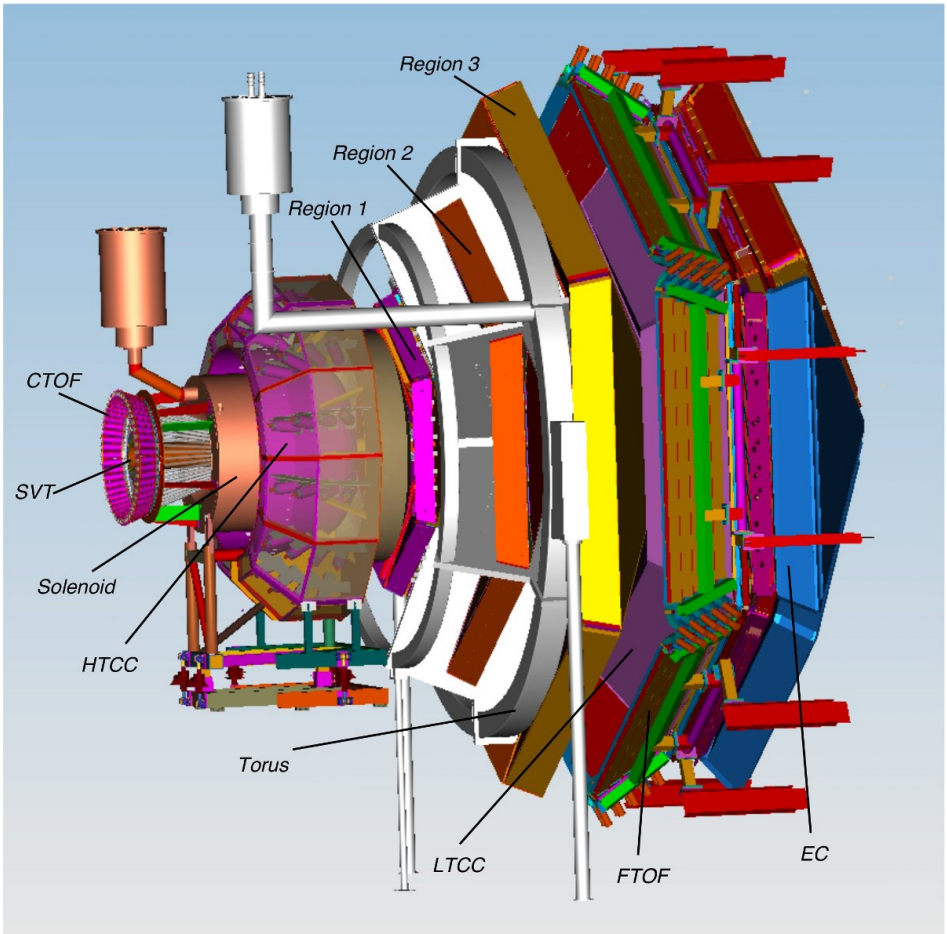

Figure 3.1: The schematic layout of the CLAS12 baseline design.

teams. Finally, we specify the technical contributions of the different partners.

3.1 The CLAS12 Spectrometer

The CLAS12 detector is designed to operate with 11 GeV beam at an electron-nucleon luminosity of $\mathcal{L} = 1 \times 10^{35}$ cm^{-2}s^{-1}. The baseline configuration of the CLAS12 detector consists of the forward detector and the central detector packages [41] (see Figure 3.1). We use the forward detector for electron detection in all ALERT run group proposals, while DVCS centered proposals also use it for photon detection. The central detector's silicon tracker and micromegas will be removed to leave room for the recoil detector.

The scattered electrons and photons will be detected in the forward detector which consists of the High Threshold Cherenkov Counters (HTCC), Drift Chambers (DC), the Low Threshold Cherenkov Counters (LTCC), the Time-of-Flight scintillators (TOF), the Forward Calorimeter and the Preshower Calorimeter. The charged particle identification in the forward detector is achieved by utilizing the combination of the HTCC, LTCC and TOF arrays with the tracking information from the Drift Chambers. The HTCC together with the Forward Calorimeter and the Preshower Calorimeter will provide a pion rejection factor of more than 2000 up to a momentum of 4.9 GeV/c, and a rejection factor of 100 above 4.9 GeV/c. The photons are detected using the calorimeters.

3.2 Available options for a Low Energy Recoil Detector

We explored available solutions for the low-energy recoil tracker with adequate momentum and spatial resolution, and good particle identification for recoiling light nuclei (p, ^{3}H and ^{3}He). After investigating the feasibility of the proposed measurements using the CLAS12 Central Detector and the BONuS Detector [18, 19], we concluded that we needed to build a dedicated detector. We summarize in the following the facts that led us to this conclusion.

3.2.1 CLAS12 Central Detector

The CLAS12 Central Detector [41] is designed to detect various charged particles over a wide momentum and angular range. The main detector package includes:

- Solenoid Magnet: provides a central longitudinal magnetic field up to 5 Tesla, which serves to curl emitted low energy Møller electrons and determine particle momenta through tracking in the central detector.
- Central Tracker: consists of 3 double layers of silicon strips and 6 layers of Micromegas. The thickness of a single silicon layer is 320 µm.
- Central Time-of-Flight: an array of scintillator paddles with a cylindrical geometry of radius 26 cm and length 50 cm; the thickness of the detector is 2 cm with designed timing resolution of $\sigma_t = 50$ ps, used to separate pions and protons up to 1.2 GeV/c.

The current design, however, is not optimal for low energy particles ($p < 300$ MeV/c) due to the energy loss in the first 2 silicon strip layers. The momentum detection threshold is ~ 200 MeV/c for protons, ~ 350 MeV/c for deuterons and even higher for ^{3}H and ^{3}He. These values are significantly too large for any of the ALERT run group proposals.

Detector Property	RTPC	ALERT
Detection region radius	4 cm	5 cm
Longitudinal length	$\sim$ 40 cm	$\sim$ 30 cm
Gas mixture	80% helium/20% DME	90% helium/10% isobutane
Azimuthal coverage	360°	340°
Momentum range	70-250 MeV/c protons	70-250 MeV/c protons
Transverse mom. resolution	10% for 100 MeV/c protons	10% for 100 MeV/c protons
z resolution	3 mm	3 mm
Solenoidal field	$\sim$ 5 T	$\sim$ 5 T
ID of all light nuclei	No	Yes
Luminosity	3×10^{33} nucleon/cm^2/s	6×10^{34} nucleon/cm^2/s
Trigger	can not be included	can be included

Table 3.2: Comparison between the RTPC (left column) and the new tracker (right column).

3.2.2 BONuS12 Radial Time Projection Chamber

The original BONuS detector was built for Hall B experiment E03-012 to study neutron structure at high x_B by scattering electrons off an almost on-shell neutron inside deuteron. The purpose of the detector was to tag the low energy recoil protons ($p > 60$ MeV/c). The key component for detecting the slow protons was the Radial Time Projection Chamber (RTPC) based on Gas Electron Multipliers (GEM). A later run period (eg6) used a newly built RTPC with a new design to detect recoiling α particles in coherent DVCS scattering. The major improvements of the eg6 RTPC were full cylindrical coverage and a higher data taking rate.

The approved 12 GeV BONuS (BONuS12) experiment is planning to use a similar device with some upgrades. The target gas cell length will be doubled, and the new RTPC will be longer as well, therefore doubling the luminosity and increasing the acceptance. Taking advantage of the larger bore ($\sim$ 700 mm) of the 5 Tesla solenoid magnet, the maximum radial drift length will be increased from the present 3 cm to 4 cm, improving the momentum resolution by 50% [19] and extending the momentum coverage. The main features of the proposed BONuS12 detector are summarized in Table 3.2.

In principle, particle identification can be obtained from the RTPC through the energy loss dE/dx in the detector as a function of the particle momentum (see Figure 3.2). However, with such a small difference between ^{3}H and ^{3}He, it is nearly impossible to discriminate between them on an event by event basis because of the intrinsic width of the dE/dx distributions.

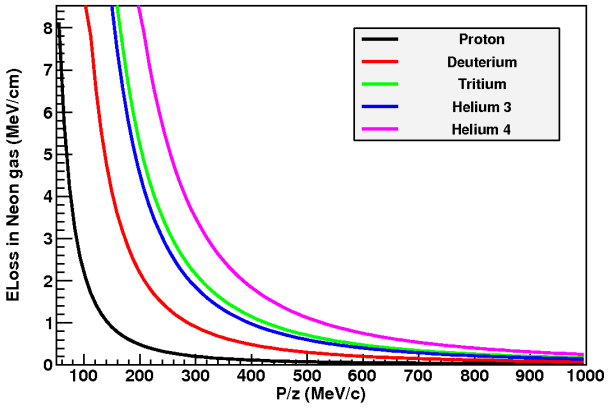

Figure 3.2: Calculation of energy loss in Neon gas as a function of the particle momentum divided by its charge for different nuclei.

This feature is not problematic when using deuterium target, but makes the RTPC no longer a viable option for our tagged EMC and tagged DVCS measurements which require a ^{4}He target and the differentiation of ^{4}He, ^{3}He, ^{3}H, deuterons and protons.

Another issue with the RTPC is its slow response time due to a long drift time (~ 5 μs). If a fast recoil detector could be included in the trigger it would have a significant impact on the background rejection. Indeed, in about 90% of DIS events on deuteron or helium, the spectator fragments have too low energy or too small angle to get out of the target and be detected. By including the recoil detector in the trigger, we would not be recording these events anymore. Since the data acquisition speed was the main limiting factor for both BONuS and eg6 runs in CLAS, this would be a much needed reduction of the pressure on the DAQ.

3.2.3 Summary

In summary, we found that the threshold of the CLAS12 inner tracker is significantly too high to be used for our measurements. On the other hand, the recoil detector planned for BONuS12, a RTPC, is not suitable due to its inability to distinguish all kind of particles we need to measure. Moreover, as the RTPC cannot be efficiently included in the trigger, a lot of background events are sent to the readout electronics, which will cause its saturation and limit the maximum luminosity the detector can handle. Therefore, we propose a new detector design.

3.3 Design of the ALERT Detector

We propose to build a low energy recoil detector consisting of two sub-systems: a drift chamber and a scintillator hodoscope. The drift chamber will be composed of 8 layers of sense wires to provide tracking information while the scintillators will provide particle identification through time-of-flight and energy measurements. To reduce the material budget, thus reducing the threshold to detect recoil particles at as low energy as possible, the scintillator hodoscope will be placed inside the gas chamber, just outside of the last layer of drift wires.

The drift chamber volume will be filled with a light gas mixture (90% He and 10% C_4H_{10}) at atmospheric pressure. The amplification potential will be kept low enough in order to not be sensitive to relativistic particles such as electrons and pions. Furthermore, a light gas mixture will increase the drift speed of the electrons from ionization. This will allow the chamber to withstand higher rates and experience lower hit occupancy. The fast signals from the chamber and the scintillators will be used in coincidence with electron trigger from CLAS12 to reduce the overall DAQ trigger rate and allow for operation at high luminosity.

The detector is designed to fit inside the central TOF of CLAS12; the silicon vertex tracker and the micromegas vertex tracker (MVT) will be removed. The available space has thus an outer radius of slightly more than 20 cm. A schematic layout of the preliminary design is shown in Figure 3.3 and its characteristics compared to the RTPC design in Table 3.2. The different detection elements are covering about 340° of the polar angle to leave room for mechanics, and are 30 cm long with an effort made to reduce the particle energy loss through the materials. From the inside out, it is composed of:

- a 30 cm long cylindrical target with an outer radius of 6 mm and target walls 25 µm Kapton filled with 3 atm of helium;
- a clear space filled with helium to reduce secondary scattering from the high rate Møller electrons with an outer radius of 30 mm;
- the drift chamber, its inner radius is 32 mm and its outer radius is 85 mm;
- two rings of plastic scintillators placed inside the gaseous chamber, with total thickness of roughly 20 mm.

3.3.1 The Drift Chamber

While drift chambers are very useful to cover large areas at a moderate price, huge progress has been made in terms of their ability to withstand higher rates using better electronics,

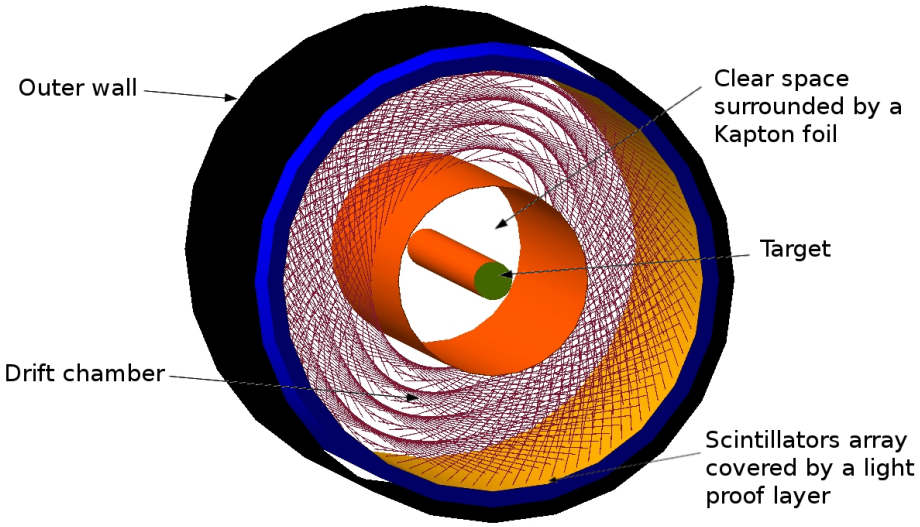

Figure 3.3: The schematic layout of the ALERT detector design, viewed from the beam direction.

shorter distance between wires and optimization of the electric field over pressure ratio. Our design is based on other chambers developed recently. For example for the dimuon arm of ALICE at CERN, drift chambers with cathode planes were built in Orsay [42]. The gap between sense wires is 2.1 mm and the distance between two cathode planes is also 2.1 mm, the wires are stretched over about 1 m. Belle II is building a cylindrical drift chamber very similar to what is needed for this experiment and for which the space between wires is around 2.5 mm [43]. Finally, a drift chamber with wire gaps of 1 mm is being built for the small wheel of ATLAS at CERN [44]. The cylindrical drift chamber proposed for our experiment is 300 mm long, and we therefore considered that a 2 mm gap between wires is technically a rather conservative goal. Optimization is envisioned based on experience with prototypes.

The radial form of the detector does not allow for 90 degrees x-y wires in the chamber. Thus, the wires of each layer are at alternating angle of $\pm$ 10°, called the stereo-angle, from the axis of the drift chamber. We use stereo-angles between wires to determine the coordinate along the beam axis (z). This setting makes it possible to use a thin forward end-plate to reduce multiple scattering of the outgoing high-energy electrons. A rough estimate of the tension due to the $\sim$2600 wires is under 600 kg, which appears to be reasonable for a composite end-plate.

The drift chamber cells are composed of one sense wire made of gold plated tungsten surrounded by field wires, however the presence of the 5 T magnetic field complicates the field lines. Several cell configurations have been studied with MAGBOLTZ [45], we decided

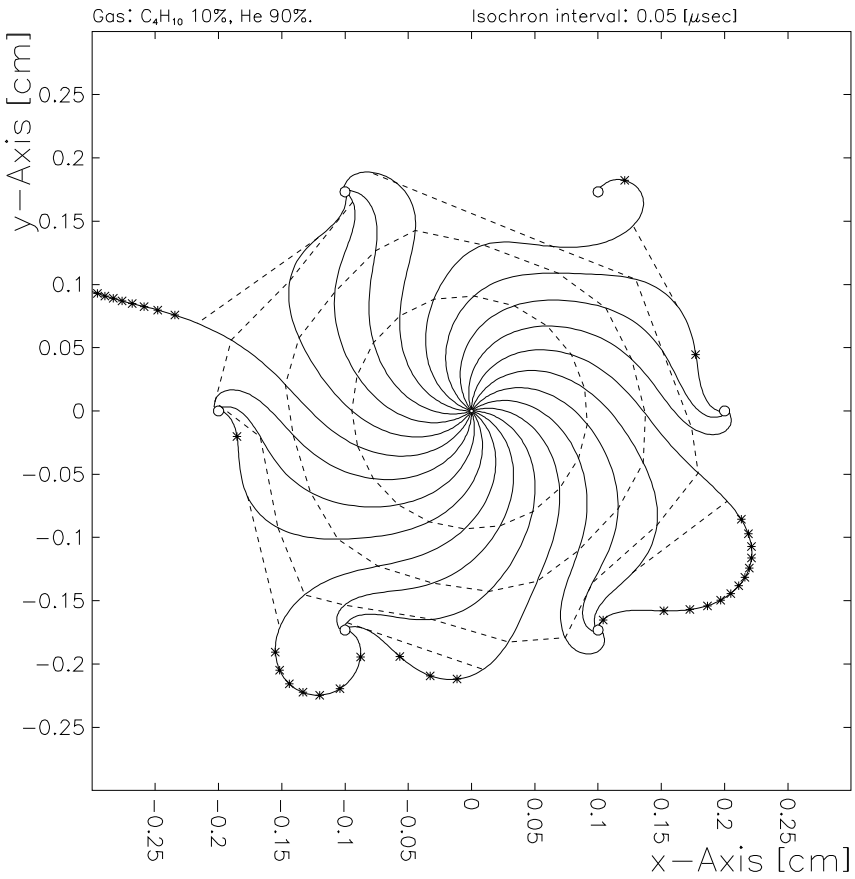

Figure 3.4: Drift lines simulated using MAGBOLTZ [45] for one sense wire (at the center) surrounded by 6 field wires. The two electric field lines leaving the cell disappear when adjusting the voltages on the wires. Dashed lines are isochrones spaced by 50 ns. This shows that the maximum drift time is about 250 ns.

to choose a conservative configuration as shown in Figure 3.4. The sense wire is surrounded by 6 field wires placed equidistantly from it in a hexagonal pattern. The distance between the sense and field wires is constant and equal to 2 mm. Two adjacent cells share the field wires placed between them. The current design will have 8 layers of cells of similar radius. The simulation code MAGBOLTZ is calculating the drift speed and drift paths of the electrons (Figure 3.4). With a moderate electric field, the drift speed is around 10 microns/ns, the average drift time expected is thus 250 ns (over 2 mm). Assuming a conservative 10 ns time resolution, the spatial resolution is expected to be around 200 microns due to field distortions and spread of the signal.

The maximum occupancy, shown in Figure 3.5, is expected to be around 5% for the inner most wires at 10^{35} $cm^{-2}s^{-1}$ (including the target windows). This is the maximum

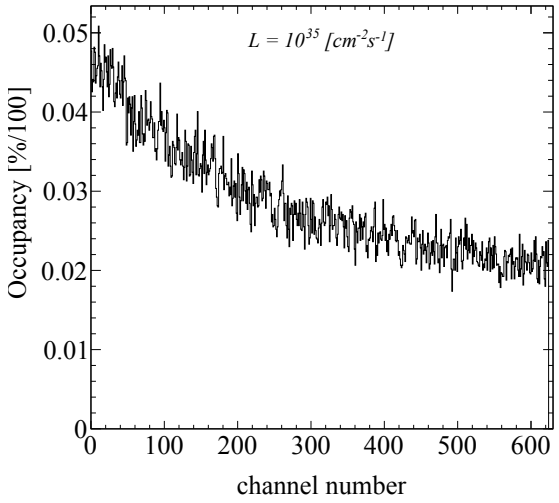

Figure 3.5: A full Geant4 simulation of the ALERT drift chamber hit occupancy at a luminosity of 10^{35} cm^{-2}s^{-1}. The channel numbering starts with the inner most wires and works outwards.

available luminosity for the baseline CLAS12 and is obtained based on the physics channels depicted in Figure 3.6, assuming an integration time of 200 ns and considering a readout wire separation of 4 mm. This amount of accidental hits does not appear to be reasonable for a good tracking quality, we therefore decided to run only at half this luminosity for our main production runs. This will keep occupancy below 3%, which is a reasonable amount for a drift chamber to maintain high tracking efficiency. When running the coherent processes with the ^{4}He target, it is not necessary to detect the protons[1], so the rate of accidental hits can then be highly reduced by increasing the detection threshold, thus making the chamber blind to the protons[2]. In this configuration, considering that our main contribution to occupancy are quasi-elastic protons, we are confident that the ALERT can work properly at 10^{35} cm^{-2}s^{-1}.

We are currently planning to use the electronics used by the MVT of CLAS12, known as the DREAM chip [46]. Its dynamic range and time resolution correspond to the needs of our drift chamber. To ensure that it is the case, tests with a prototype will be performed at the IPN Orsay (see section 3.5).

[1] This running condition is specific to the proposal "Partonic Structure of Light Nuclei" in the ALERT run group.

[2] The CLAS *eg6* run period was using the RTPC in the same fashion.

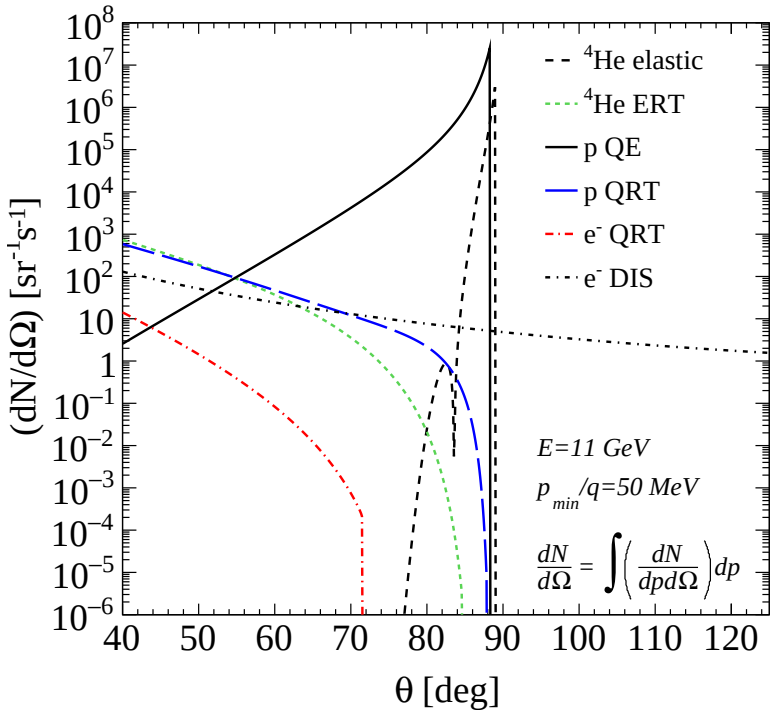

Figure 3.6: The rates for different processes as function of angle. The quasi-elastic radiative tails (QRT), ^{4}He elastic radiative tail (ERT), and DIS contributions have been integrated over momenta starting at $p/q = 50$ MeV/c, where q is the electric charge of the particle detected.

3.3.2 The Scintillator Array

The scintillator array will serve two main purposes. First, it will provide a useful complementary trigger signal because of its very fast response time, which will reduce the random background triggers. Second, it will provide particle identification, primarily through a time-of-flight measurement, but also by a measurement of the particle total energy deposited and path length in the scintillator which is important for doubly charged ions.

The length of the scintillators cannot exceed roughly 40 cm to keep the time resolution below 150 ps. It must also be segmented to match with tracks reconstructed in the drift chamber. Since ^{3}He and ^{4}He will travel at most a few mm in the scintillator for the highest anticipated momenta ($\sim$ 400 MeV/c), a multi-layer scintillator design provides an extra handle on particle identification by checking if the range exceeded the thickness of the first scintillator layer.

The initial scintillator design consists of a thin (2 mm) inner layer of 60 bars, 30 cm in length, and 600 segmented outer scintillators (10 segments 3 cm long for each inner bar) wrapped around the drift chamber. Each of these thin inner bars has SiPM[3] detectors attached to both ends. A thicker outer layer (18 mm) will be further segmented along the beam axis to provide position information and maintain good time resolution.

For the outer layer, a dual ended bar design and a tile design with embedded wavelength shifting fiber readouts similar to the forward tagger's hodoscope for CLAS12 [47] were considered. After simulating these designs, it was found that the time resolution was insufficient except only for the smallest of tile designs ($15\times15\times7$ mm^3). Instead of using fibers, a SiPM will be mounted directly on the outer layer of a keystone shaped scintillator that is 30 mm in length and 18 mm thick. This design can be seen in Figure 3.7 which shows a full Geant4 simulation of the drift chamber and scintillators. By directly mounting the SiPMs to the scintillator we collect the maximum signal in the shortest amount of time. With the large number of photons we expect, the time resolution of SiPMs will be a few tens of ps, which is well within our target.

The advantage of a dual ended readout is that the time sum is proportional to the TOF plus a constant. The improved separation of different particles can be seen in Figure 3.8. Reconstructing the position of a hit along the length of a bar in the first layer is important for the doubly charged ions because they will not penetrate deep enough to reach the second layer of segmented scintillator.

[3]SiPM: silicon photomultiplier.

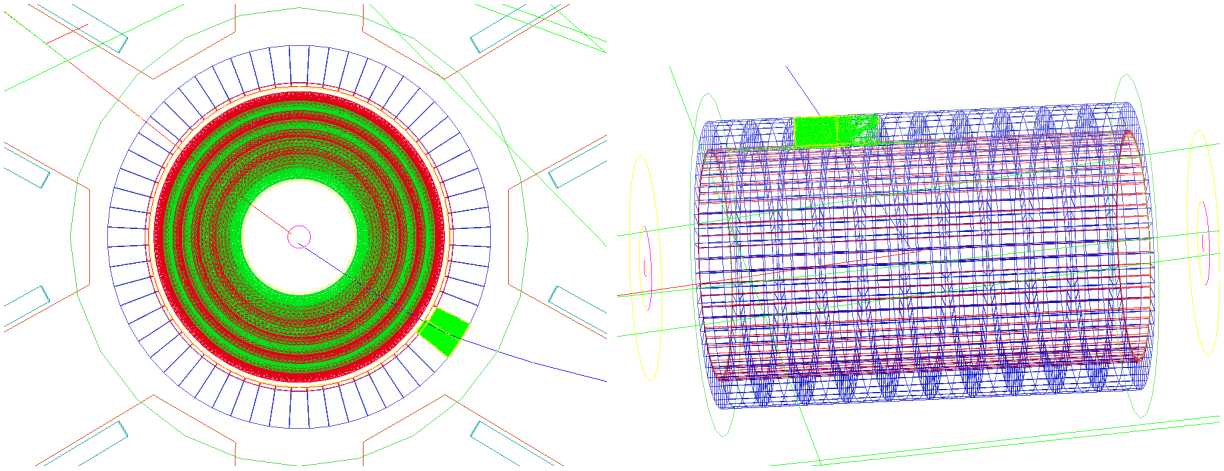

Figure 3.7: Geant4 simulation of a proton passing through the recoil drift chamber and scintillator hodoscope. The view looking downstream (left) shows the drift chamber's eight alternating layers of wires (green and red) surrounded by the two layers of scintillator (red and blue). Simulating a proton through the detector, photons (green) are produced in a few scintillators. On the right figure, the dark blue rings are graphical feature showing the contact between the adjacent outer scintillators.

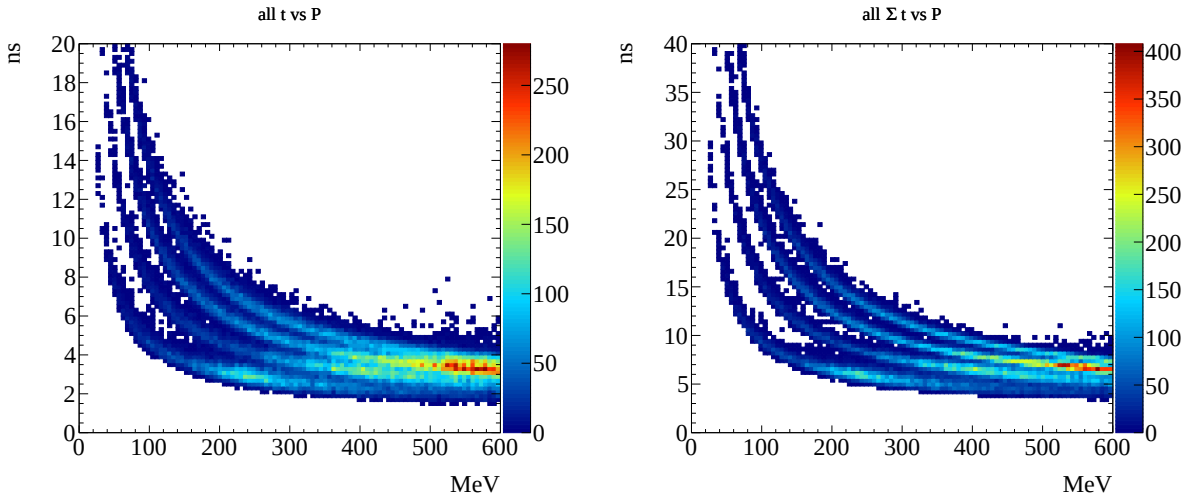

Figure 3.8: Simulated TOF for the various recoil particles vs Momentum. The TOF from just a single readout is shown on the left and the sum of the dual ended readout is shown on the right.

The front-end electrons for the SiPMs will include preamplifiers and ASICs[4] which provide both TDC and ADC readouts. The PETIROC-2A[48] ASIC provides excellent time resolution (18 ps on trigger output with 4 photoelectrons detected) and a maximum readout rate at about 40k events/s. Higher readout rates can be handled by using external digitizers by using the analog mode of operation and increase this rate by an order of magnitude. The ASIC also has the advantage of being able to tune the individual over-bias voltages with an 8-bit DAC.

The expected radiation damage to the SiPMs and scintillator material is found to be minimal over the length of the proposed experiment. We used the CLAS12 forward tagger hodoscope technical design report [47] as a very conservative baseline for this comparison. We arrived at an estimated dose of 1 krad after about 4.5 months of running. The damage to the scintillator at 100 times these radiation levels would not be problematic, even for the longest lengths of scintillator used [49]. Accumulated dose on the SiPMs leads to an increased dark current. Similarly than for scintillators, we do not expect it to be significant over the length of the experiment. The interested reader is referred to the work on SiPMs for the Hall-D detectors [50, 51]. A front-end electronics prototype will be tested for radiation hardness but we expect any damage to negligible [52].

3.3.3 Target Cell

The design of the proposed ALERT target will be very similar to the eg6 target shown in Figure 3.9. The target parameters are shown in Table 3.3 with the parameters of other existing and PAC approved targets. Note that, the proposed target has an increased radius of 6 mm compared to all the others which have 3 mm radius. This increase compared to the previous CLAS targets has been made in order to compensate for the expected increase of beam size at 11 GeV. The BONuS12 target is still presently proposed to be 3 mm in radius, if such a target is operated successfully in JLab, we will definitely consider using a smaller radius as well, but we prefer to propose here a safer option that we know will work fine.

3.4 Simulation of ALERT and reconstruction

The general detection and reconstruction scheme for ALERT is as follows. We fit the track with the drift chamber and scintillator position information to obtain the momentum over the charge. Next, using the scintillator time-of-flight, the particles are separated and identified by their mass-to-charge ratio, therefore leaving a degeneracy for the deuteron and

[4] ASIC: application-specific integrated circuit.

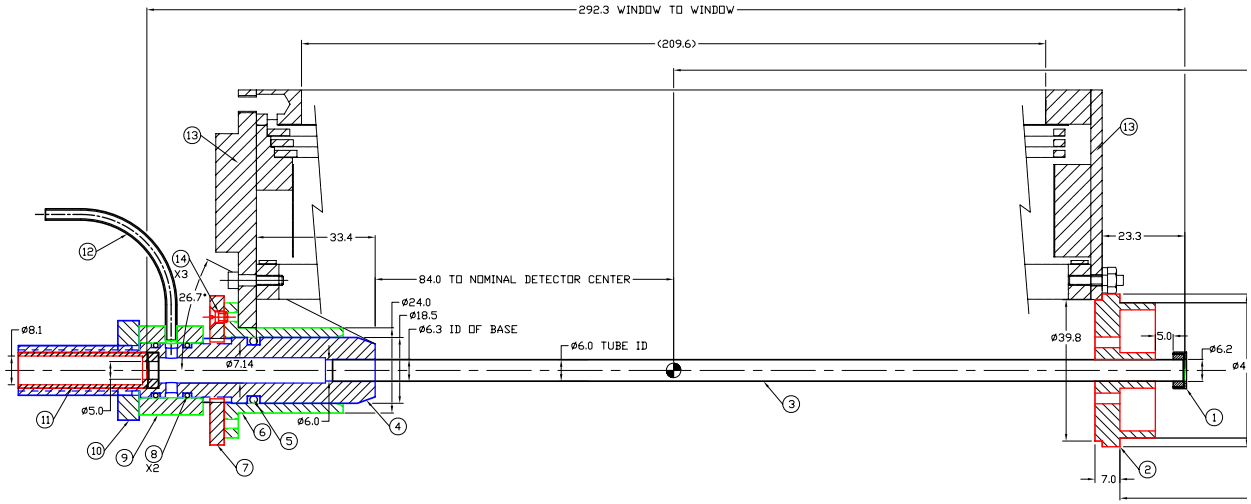

Figure 3.9: The eg6 target design drawing.

Table 3.3: Comparison of various straw targets used at JLab.The "JLab test targets" correspond to recent tests performed in JLab for the BONuS12 target, they have been tested for pressure but have never been tested with beam.

Experiment	**Length**	**Kapton wall thickness**	**Pressure**
CLAS target (eg6)	30 cm	27 µm	6.0 atm
BONuS12 (E12-06-113) target	42 cm	30 µm	7.5 atm
JLab test target 1	42 cm	30 µm	3.0 atm
JLab test target 2	42 cm	50 µm	4.5 atm
JLab test target 3	42 cm	60 µm	6.0 atm
ALERT proposed target	35 cm	25 µm	3.0 atm

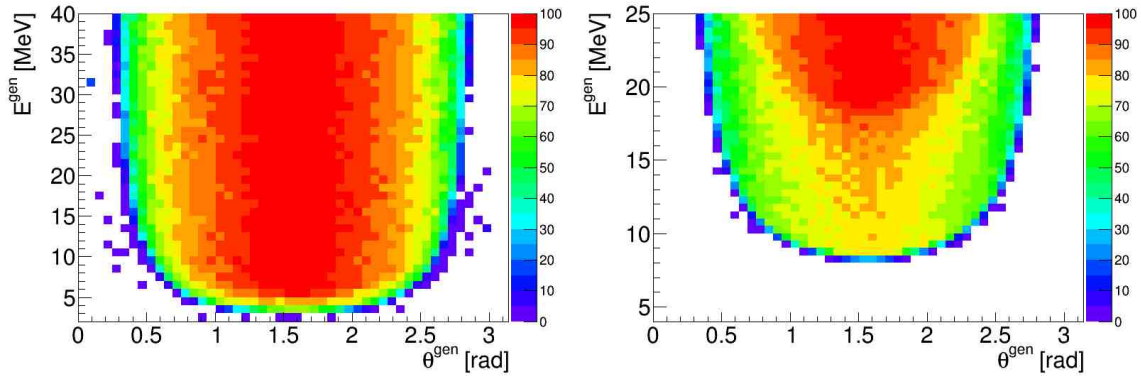

Figure 3.10: Simulated recoil detector acceptance percentage, for protons (left) and ^{4}He (right), when requiring energy deposition in the scintillators arrays.

α particles. The degeneracy between deuteron and α particles can be resolved in a few ways. The first and most simple way is to observe that an α will almost never make it to the second layer of scintillators and therefore the absence (presence) of a signal would indicate the particle is an α (deuteron). Furthermore, as will be discussed below, the measured dE/dx will differ for ^{4}He and ^{2}H, therefore, taking into account energy loss in track fitting alone can provide separation. Additionally taking further advantage of the measured total energy deposited in the scintillators can help separate the αs and deuterons.

3.4.1 Simulation of ALERT

The simulation of the recoil detector has been implemented with the full geometry and material specifications in GEANT4. It includes a 5 Tesla homogeneous solenoid field and the entire detector filled with materials as described in the previous section. In this study all recoil species are generated with the same distributions: flat in momentum from threshold up to 40 MeV ($\sim$ 250 MeV/c) for protons and about 25 MeV for other particles; isotropic angular coverage; flat distribution in z-vertex; and a radial vertex coordinate smeared around the beam line center by a Gaussian distribution of sigma equal to the expected beam radius (0.2 mm). For reconstruction, we require that the particle reaches the scintillator and obtain the acceptance averaged over the z-vertex position shown in Figure 3.10.

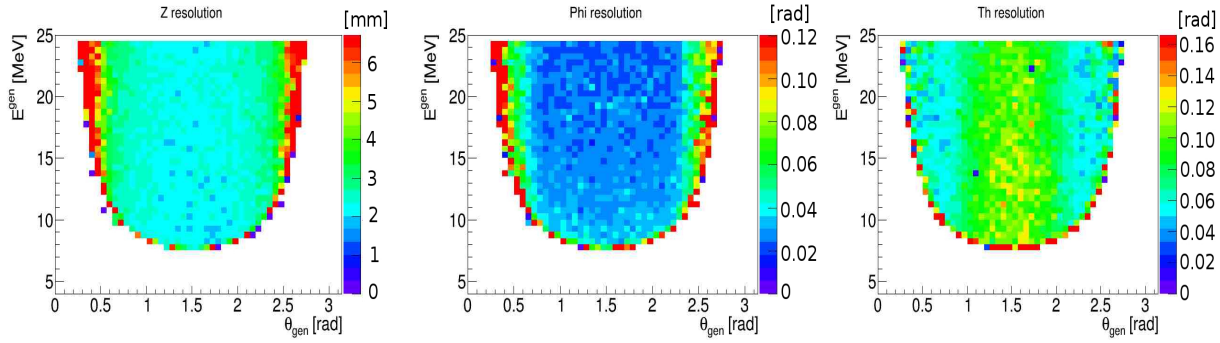

Figure 3.11: Resolutions for simulated ^{4}He: z-vertex resolution in mm (left), azimuthal (center) and polar (right) angle resolutions in radians for the lowest energy regime when the recoil track reaches the scintillator.

3.4.2 Track Fitting

The tracks are obtained using a helix fitter giving the coordinates of the vertex and the momentum of the particle. The energy deposited in the scintillators could also be used to help determine the kinetic energy of the nucleus, but is not implemented in the studies we performed here. The tracking capabilities of the recoil detector are investigated assuming a spatial resolutions of 200 µm for the drift chamber. The wires are strung in the z-direction with a stereo angle of 10°. The resulting difference between generated and reconstructed variables from simulation is shown in Figure 3.11 for ^{4}He particles. The momentum resolution for both protons and ^{4}He is presented in Figure 3.12.

3.4.3 Particle identification in ALERT

The particle identification scheme is investigated using the GEANT4 simulation as well. The scintillators have been designed to ensure a 150 ps time resolution. To determine the dE/dx resolution, measurements will be necessary for the scintillators and for the drift chamber as this depends on the detector layout, gas mixture, electronics, voltages... Nevertheless, from [53], one can assume that with 8 hits in the drift chamber and the measurements in the scintillators, the energy resolution should be at least 10%. Under these conditions, a clean separation of three of the five nuclei is shown in Figure 3.13 solely based on the time of flight measured by the scintillator compared to the reconstructed momentum from the drift chamber. We then separate ^{2}H and α using dE/dx in the drift chamber and in the scintillators.

To quantify the separation power of our device, we simulated an equal quantity of each

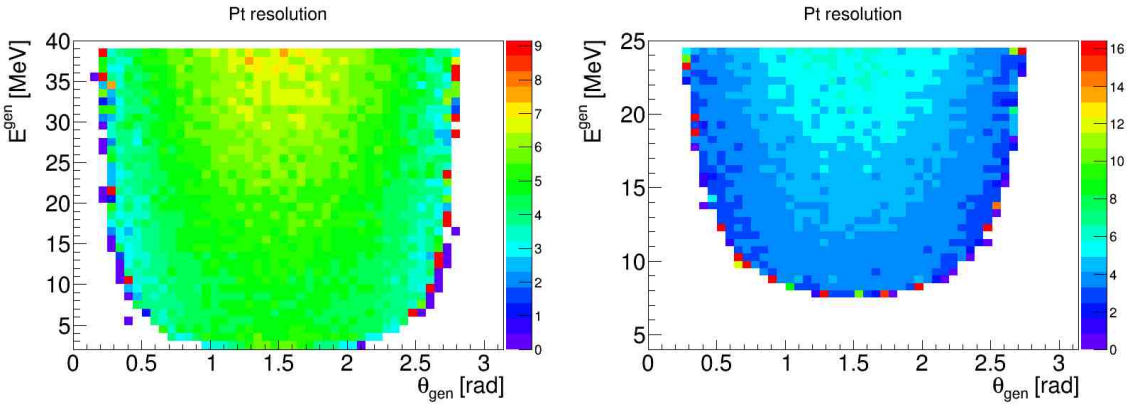

Figure 3.12: Simulated momentum resolutions (in %) as a function of energy and polar angle for protons (left) and ^{4}He (right) integrated over all z, when the recoil track reaches the scintillators array.

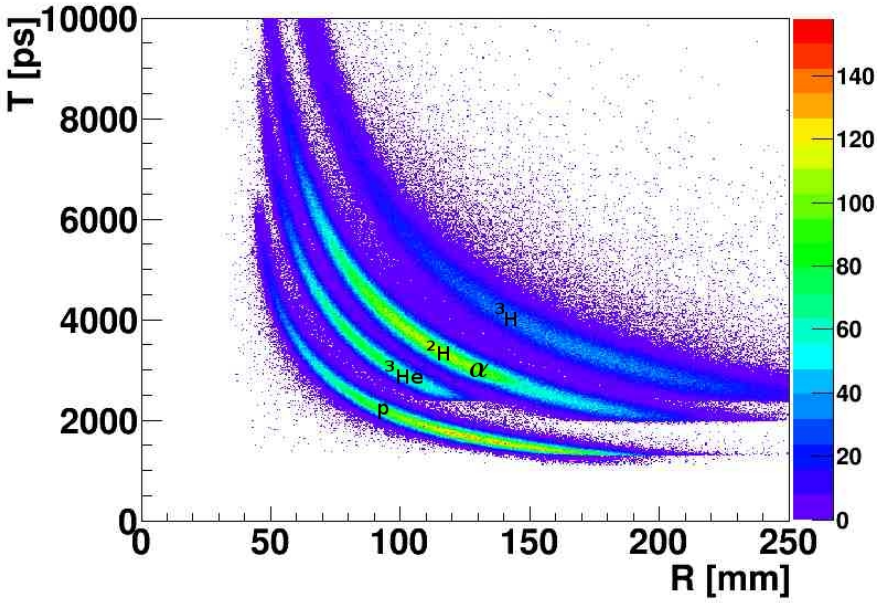

Figure 3.13: Simulated time of flight at the scintillator versus the reconstructed radius in the drift chamber. The bottom band corresponds to the proton, next band is the ^{3}He nuclei, ^{2}H and α are overlapping in the third band, the uppermost band is ^{3}H. ^{2}H and α are separated using dE/dx.

species. We obtained a particle identification efficiency of 99% for protons, 95% for ^{3}He and 98% for ^{3}H and around 90% for ^{2}H and α with equally excellent rejection factors. It is important to note that for this analysis, only the energy deposited in the scintillators was used, not the energy deposited in the drift chamber nor the path length in the scintillators, thus these numbers are very likely to be improved when using the full information[5]. This analysis indicates that the proposed reconstruction and particle identification schemes for this design are quite promising. Studies, using both simulation software and prototyping, are ongoing to determine the optimal detector parameters to minimize the detection threshold while maximizing particle identification efficiency. The resolutions presented above have been implemented in a fast Monte-Carlo used to evaluate their impact on our measurements.

3.5 Drift chamber prototype

Since the design of the drift chamber presents several challenges in term of mechanical assembly, we decided to start prototyping early. The goal is to find a design that will be easy to install and to maintain if need be, while keeping the amount of material at a minimum. This section presents the work done in Orsay to address the main questions concerning the mechanics that needed to be answered:

- How to build a stereo drift chamber with a 2 mm gap between wires?
- Can we have frames that can be quickly changed in case of a broken wire?
- How to minimize the forward structure to reduce the multiple scattering, while keeping it rigid enough to support the tension due to the wires?

For the first question, small plastic structures realized with a 3D printer were tested and wires welded on it, as shown in Figure 3.14. This demonstrated our ability to weld wires with a 2 mm gap on a curved structure.

To limit issues related to broken wires, we opted for a modular detector made of identical sectors. Each sector covers 20° of the azimuthal angle (Figure 3.15) and can be rotated around the beam axis to be separated from the other sectors. This rotation is possible due to the absence of one sector, leaving a 20° dead angle. Then, if a wire breaks, its sector can be removed independently and replaced by a spare. Plastic and metallic prototype sectors were made with 3D printers to test the assembling procedure and we have started the construction

[5]The uncertainty remains important about the resolutions that will be achieved for these extra information. So we deemed more reasonable to ignore them for now.

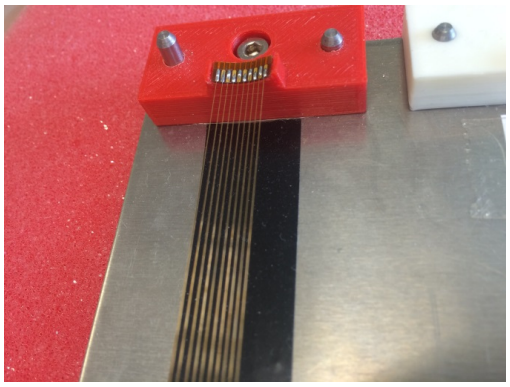

Figure 3.14: Welded wires on a curved structure with a 2 mm gap between each wire.

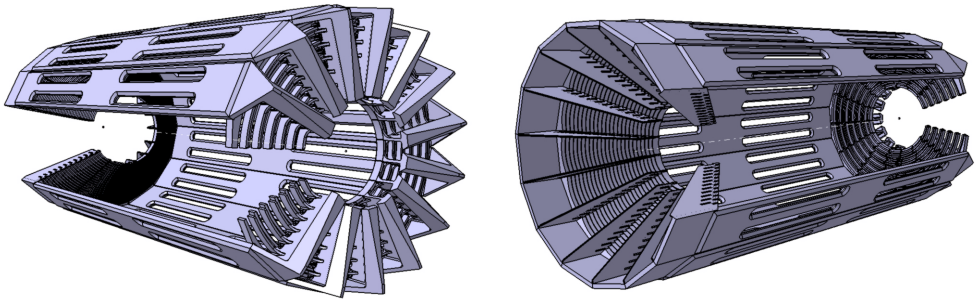

Figure 3.15: Upstream (left) and downstream (right) ends of the prototype detector in computer assisted design (CAD) with all the sectors included.

of a full size prototype of one sector. The shape of each sector is constrained by the position of the wires. It has a triangular shape on one side and due to the stereo angle, the other side looks like a pine tree with branches alternatively going left and right from a central trunk (Figure 3.16).

Finally, the material used to build the structure will be studied in details with future prototypes. Nevertheless, most recent plans are to use high rigidity plastic in the forward region and metal for the backward structure (as in Figure 3.17). The prototypes are not only designed to check the mechanical requirements summarized above but also to verify the different cell configurations, and to test the DREAM electronics (time resolution, active range, noise).

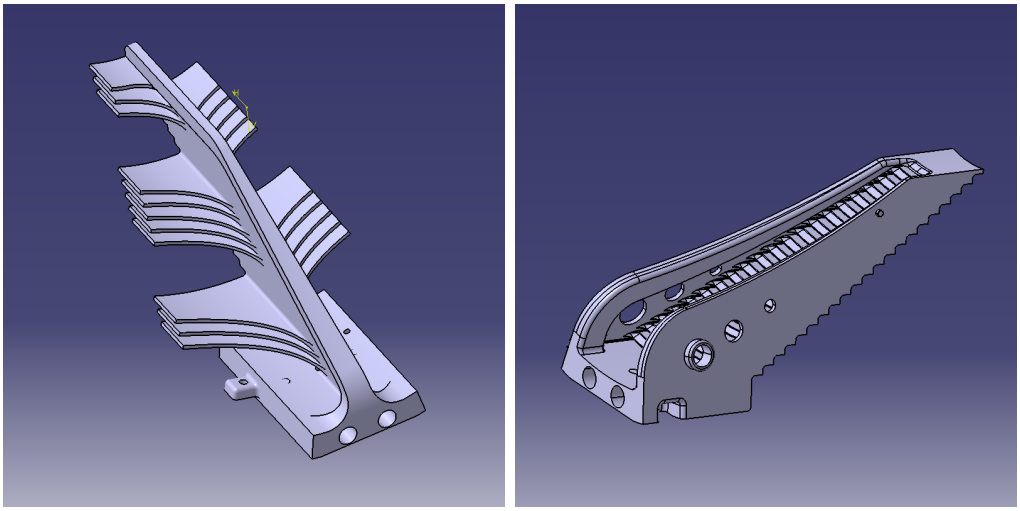

Figure 3.16: Close up on the CAD of the upstream piece (left) and downstream piece(right) of the drift chamber. Note that the design of the pieces has been optimized in comparison of what is shown in Figure 3.15.

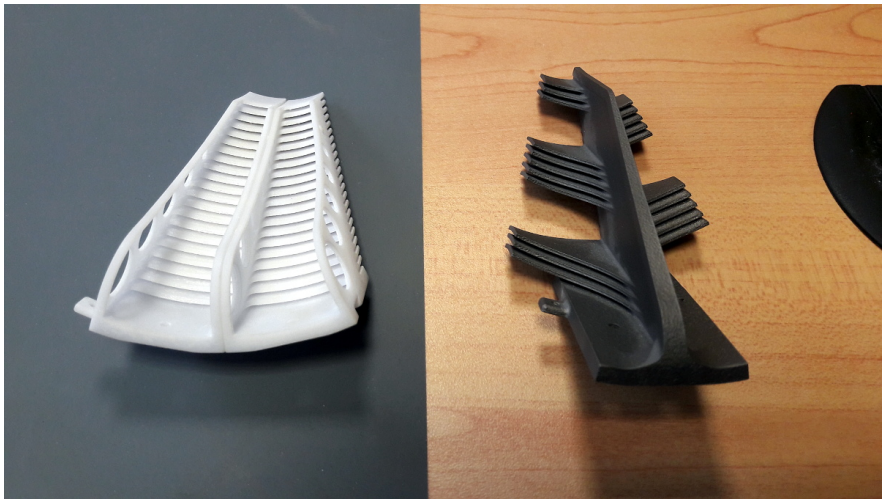

Figure 3.17: Prototypes for the mechanical parts of the drift chamber made out of plastic for the forward part and titanium for the backward.

3.6 Technical contributions from the research groups

The effort to design, build and integrate the ALERT detector is led by four research groups, Argonne National Lab (ANL), Institut de Physique Nucléaire d'Orsay (IPNO), Jefferson Lab and Temple University (TU).

Jefferson Lab is the host institution. ANL, IPNO and TU have all contributed technically to CLAS12. ANL was involved in the construction of the high-threshold Cherenkov counters (HTCC) for CLAS12. ANL has a memorandum of understanding (MOU) with JLab on taking responsibility for the HTCC light collection system including testing the photomultipliers and the magnetic shielding. For the RICH detector for CLAS12, ANL developed full GEANT-4 simulations in addition to the tracking software. ANL also developed the mechanical design of the detector support elements and entrance and exit windows in addition to the front-end electronics cooling system. IPNO took full responsibility for the design and construction of CLAS12 neutron detector (CND). The CND was successfully delivered to Jefferson Lab. TU played an important role in the refurbishment of the low threshold Cherenkov counters (LTCC), which was completed recently. All 216 photomultipliers have been coated with wavelength shifting material (p-Terphenyl) at Temple University, which resulted in a significant increase in the number of photoelectrons response.

The three institutions have already shown strong technical commitment to JLab 12 GeV upgrade, with a focus on CLAS12 and this proposal is a continuation of this commitment.

3.6.1 Argonne National Laboratory and Temple University

The ANL medium energy group is responsible for the ALERT scintillator system, including scintillation material, light collection device and electronics. First results of simulations have led to the design proposed here. This work will continue to integrate the scintillator system with the wire chamber. ANL will collaborate closely with Temple University to test the light detection system. Both institutions will be responsible to assemble and test the detector.

Argonne will provide the electronics and technical support required to integrate the scintillator detector system into the CLAS12 DAQ. The effort will minimize the effort required on the part of the Hall B staff.

3.6.2 Institut de Physique Nucléaire d'Orsay

The Institut de Physique Nucléaire d'Orsay is responsible for the wire chamber and the mechanical structure of the detector design and construction. As shown in the proposal, this work has already started, a first prototype is being built to test different cell forms, wire material, wire thickness, pressure, etc. This experience will lead to a complete design of the ALERT detector integrating the scintillator built at ANL, the gas distribution system and the electronic connections.

In partnership with *CEA Saclay*, IPN Orsay will also test the use of the DREAM front-end chip for the wire chamber. Preliminary tests were successful and will continue. The integration of the chip with CLAS12 is expected to be done by the *CEA Saclay*, since they use the same chip to readout the CLAS12 MVT. Adaptations to the DAQ necessary when the MVT will be replaced by ALERT will be performed by the staff of IPN Orsay.

3.6.3 Jefferson Laboratory

We expect Jefferson Lab to help with the configuration of the beam line. This will include the following items.

Beam Dump Upgrade The maximum beam current will be around 1000 nA for the production runs at 10^{35} $cm^{-2}s^{-1}$, which is not common for Hall-B. To run above 500 nA the "beam blocker" will need to be upgraded to handle higher power. The beam blocker attenuates the beam seen by the Faraday cup. This blocker is constructed of copper and is water cooled. Hall B staff have indicated that this is a rather straightforward engineering task and has no significant associated costs [54].

Straw Target We also expect JLab to design and build the target for the experiment as it will be a very similar target as the ones build for CLAS BONuS and eg6 runs. See section 3.3.3 for more details.

Mechanical Integration We also expect Jefferson Laboratory to provide assistance in the detector installation in the Hall. This will include providing designers at ANL and IPNO with the technical drawings required to integrate ALERT with CLAS12. We will also need some coordination between designers to validate the mechanical integration.

CLAS12 DAQ Integration We also will need assistance in connecting the electronics of ALERT to the CLAS12 data acquisition and trigger systems. This will also include help integrating the slow controls into the EPICs system.

Chapter 4

Proposed Measurements

We propose to measure the beam spin asymmetry for three DVCS channels using two different targets and with tagged spectator systems. The three principal reactions are:

- $^4\mathrm{He}(\vec{e}, e'\,\gamma\,{}^3\mathrm{H}p)$ – bound p-DVCS
- $^4\mathrm{H}(\vec{e}, e'\,\gamma\,{}^3\mathrm{He})n$ – bound n-DVCS
- $^2\mathrm{H}(\vec{e}, e'\,\gamma\,p)n$ – quasi-free n-DVCS

where in the first process the final state is fully detected. Before discussing the details of the measurements, we present an overview of the procedure for extracting the $\sin\phi$ harmonic of the BSAs and identify the primary deliverables of the experiment.

4.1 Asymmetry Extraction Procedure

Figure 4.1 shows how, starting with just one kinematic bin in t, Q^2, and x (which is not explicitly shown), the BSA is extracted for three regions of spectator recoil angles relative to the virtual photon direction and three ranges of spectator momenta. As indicated, the spectator angles correspond to a forward tagged system, a system with perpendicular momenta, and a backward tagged spectator. In the latter angular region FSIs are expected to minimal. Furthermore, three ranges of momenta are identified, the lowest corresponding to nucleons moving in the mean field and the highest belonging to nucleons in short range correlated

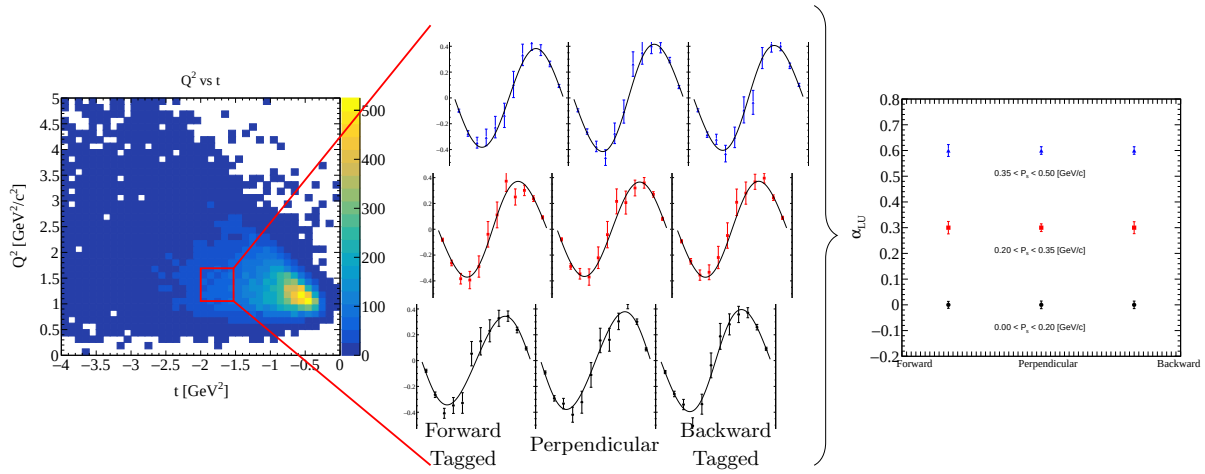

Figure 4.1: A general overview of the BSA extraction procedure for a kinematic bin. For each (x, Q^2, t) bin the BSA is extracted through fitting the asymmetry as function of ϕ (see Equation 4.1) for the various spectator momentum configurations and the $\sin\phi$ harmonic, α is extracted. Note these plots are only showing statistical uncertainties and the values are offset for clarity.

pairs. Fitting the BSA asymmetries yields the $\sin\phi$ harmonic which is shown on the right of Figure 4.1 for the different spectator kinematic regions.

The first process above, p-DVCS on ^{4}He, provides a model independent way of identifying kinematics where final state interactions are minimized (see Introduction and Chapter 1). Armed with this information we will then measure the n-DVCS beam spin asymmetries on ^{4}He and ^{2}H knowing which kinematics are, or are not, influenced by FSIs. We will then proceed as shown in Figure 4.2 where the two n-DVCS measurements are combined into a ratio of bound neutron to quasi-free neutron. These BSA measurements and ratios are the primary deliverables of this proposal. They will be measured over a broad range of DVCS kinematics accessible to CLAS12 and for the spectator momenta regions noted above using the ALERT detector.

4.2 Kinematic Coverage

The kinematic coverage was studied using a newly developed CLAS12 fast Monte-Carlo, `c12sim`, where the CLAS12 detector resolutions were replicated based on the Fortran CLAS12 Fast-MC code. Because `c12sim` is a Geant4 based simulation, the particle transport through the magnetic fields was handled by the Geant4 geometry navigation where all other processes were turned off. The resolutions for ALERT were obtained through full Geant4 simulations

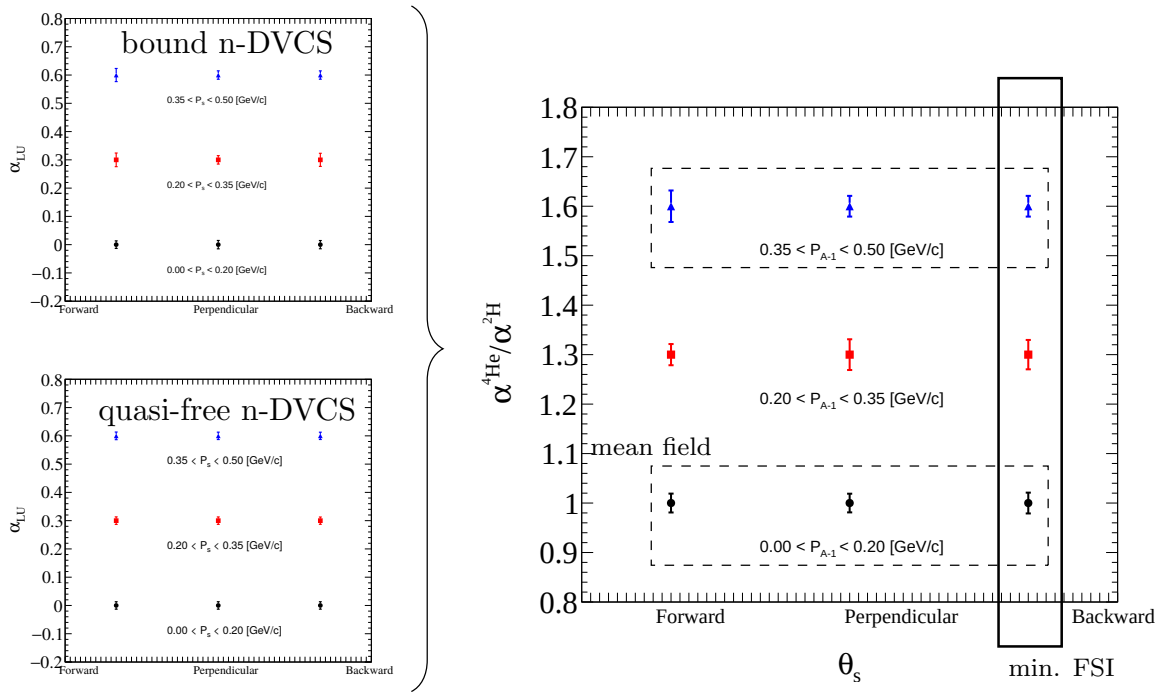

Figure 4.2: The BSA ratios targeting different nuclear effects with specific spectator kinematics. Note only statistical uncertainties are shown and the BSA harmonics/ratios are (arbitrarily) offset for clarity.

with all physics processes turned on.

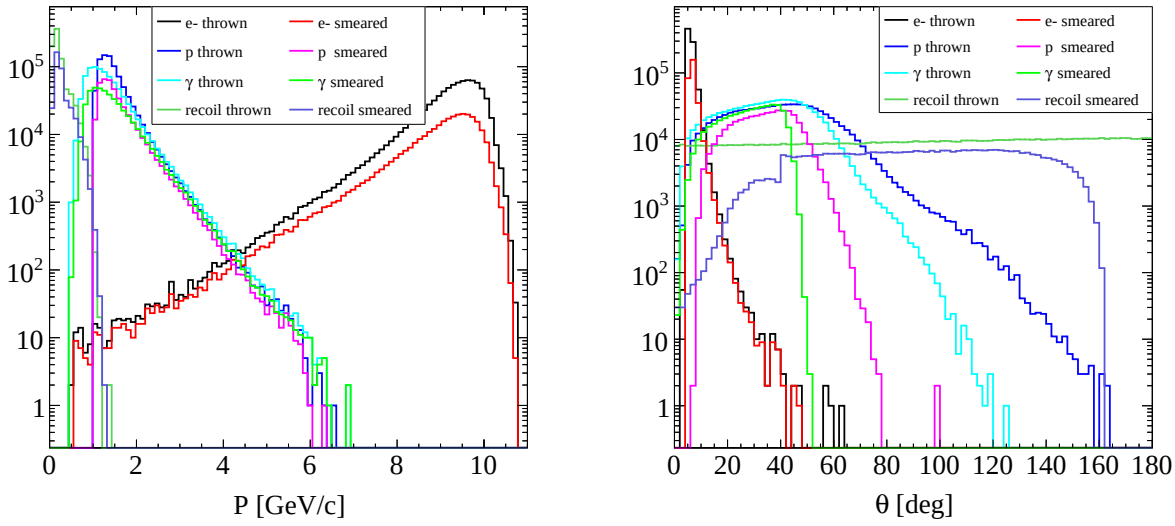

Figure 4.3: The simulated and detected momentum (left) and angular (right) distributions showing overall detector coverage for the experiment.

First, we consider the p-DVCS reaction on ^{4}He because of its special ability to determine the presence of final state interactions through a fully detected final state. The spectator system, a recoiling ^{3}H in the present case, is detected in ALERT while the forward electron, photon, and proton are detected in CLAS12. The resulting kinematics for the n-DVCS on ^{2}H and ^{4}He reactions will be quite similar, where the key difference is the struck neutron goes undetected. These events are then selected via the neutron missing mass cuts.

The overall coverage in momentum and scattering angle can be seen in Figure 4.3 and angular detector coverage of all the particles can be seen in Figure 4.5. The bin variables x, Q^2, and t are shown in Figure 4.6. See C.1 for more details on the kinematic coverage.

As mentioned throughout this proposal and with detail in appendix A, the momentum transfer can be reconstructed via using the photons, or using the nucleon side of the diagram where we make use use of the detected spectator system and the PWIA. Figure 4.4 shows that the resolutions are comparable, thus, allowing for the systematic check of FSIs which were not included in the generated events. The spectator angle and momentum can be seen in Figure 4.7, where these results can be used along with calculations such as those shown in Figure 1.6 to isolate kinematic regions with significant FSIs.

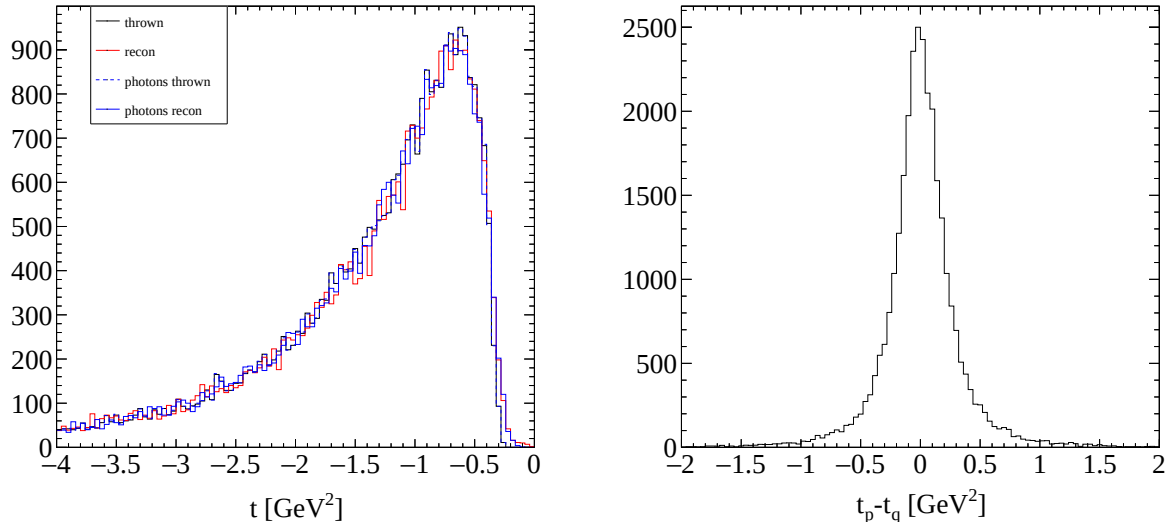

Figure 4.4: Left: simulated and reconstructed t calculated from the photons (t_q) and hadrons (t_p). Right: The difference between the two momentum transfers, $\delta t = t_p - t_q$.

4.3 Projections

4.3.1 Beam Spin Asymmetry Extraction

The measured beam spin asymmetries are binned in 6 variables: x_B, Q^2, t, ϕ, P_s, and θ_s. The 6 dimensional data will be reduced to 5 dimensions by fitting the BSA as a function of ϕ to extract harmonic content. Projections for the statistical uncertainties of these asymmetries and their fits are shown for a few bins in Figure 4.8 and Figure 4.9 for p-DVCS on ^{4}He. A few of the ϕ binned asymmetries for n-DVCS on ^{4}He are shown in Figure 4.10 and similarly in Figure 4.11 for n-DVCS on ^{2}H. Note that we are using a simple binning scheme shown in Table 4.1. These bins are likely to change as the cross sections are not well known, especially when isolating high momentum spectators.

The beam spin asymmetries are the primary observables for this experiment and will be fit with the following simplified parameterization

$$A_{LU}(\phi) = \frac{\alpha \sin\phi}{1 + \beta \cos\phi} \tag{4.1}$$

where the free parameters α and β are related to CFFs and Fourier harmonics. As emphasized in section 1.2.2, the $\sin\phi$ harmonic, α, is quite sensitive to nuclear effects. Therefore, we will extract α for every bin by fitting the asymmetry binned in ϕ for each kinematic setting. Out

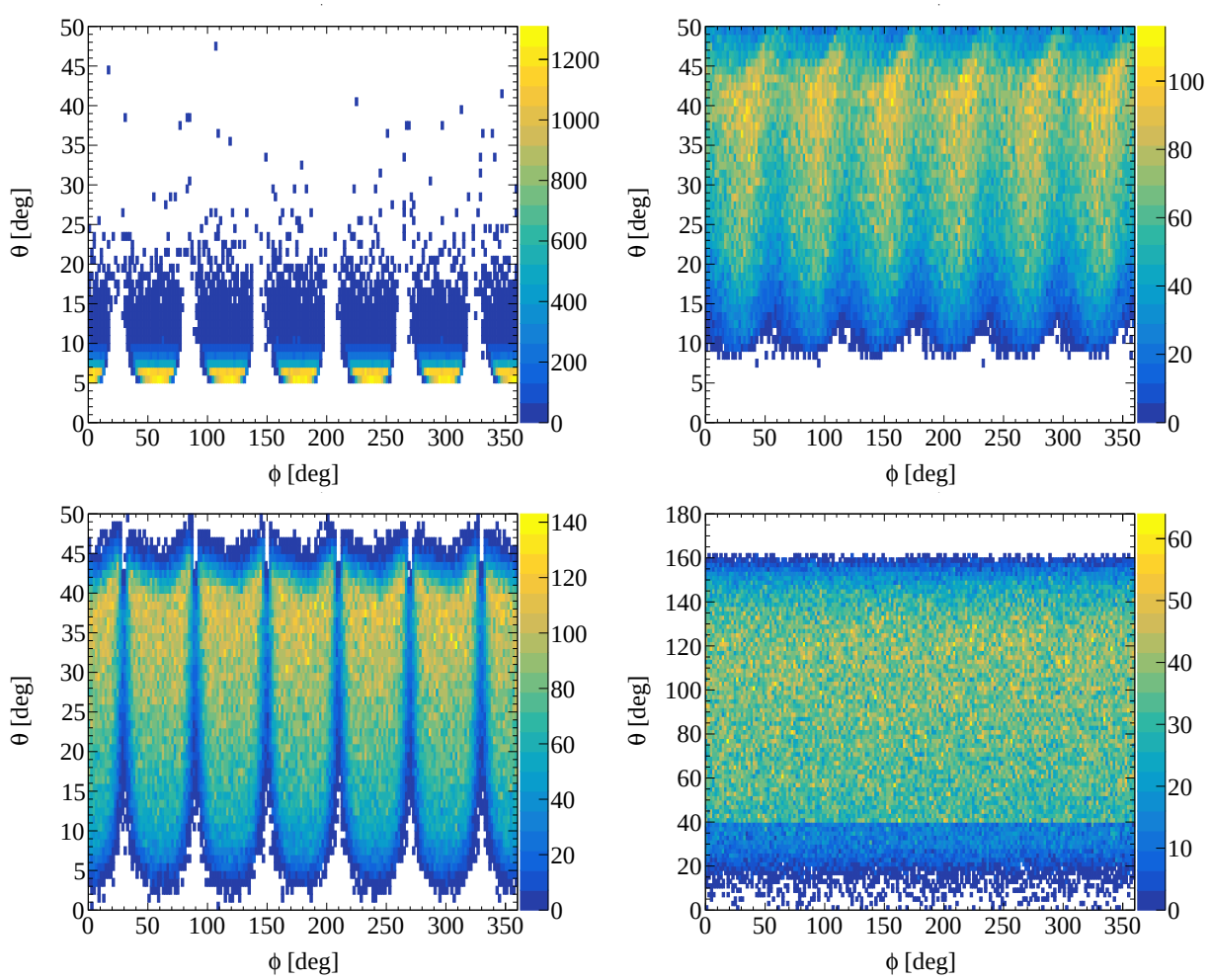

Figure 4.5: The angular coverage shown as θ Vs. ϕ for the electron (upper left), proton (upper right), photon (lower left), and recoil spectator (lower right).

Bin	x	Q^2	t	θ_s	P_s
units		GeV^2	GeV^2	$^\circ$	GeV/c
	0.05	1	0	0.0	0.0
	0.25	1.5	0.75	50	0.2
	0.35	2.0	1.5	100	0.35
	0.5	3.0	2.5	180	0.5
	0.8	10	6.0		

Table 4.1: The simple binning scheme used for the proposal. Listed here are the bin edges forming each bin.

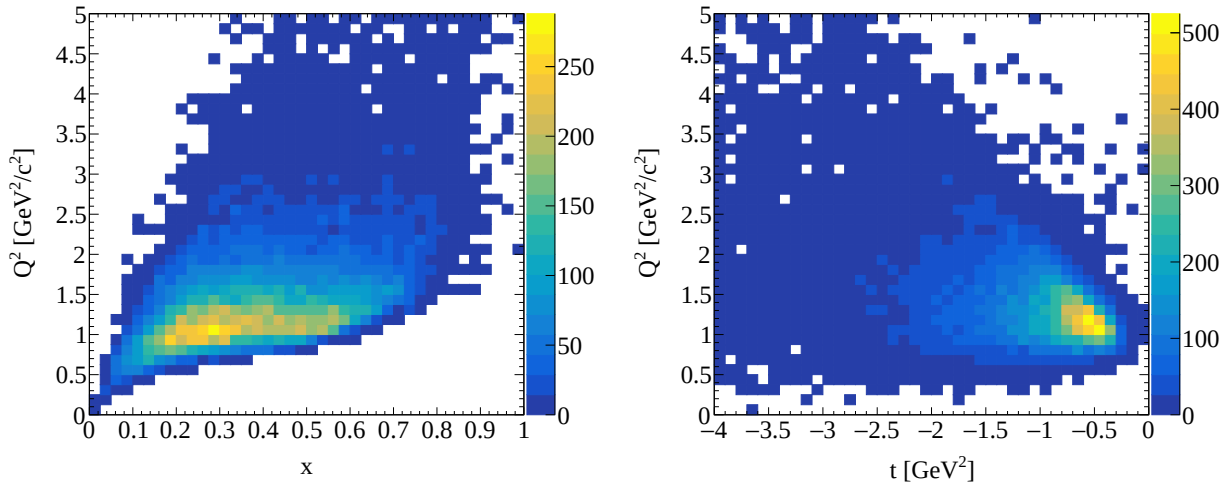

Figure 4.6: Q^2 plotted against x (left) and t (right).

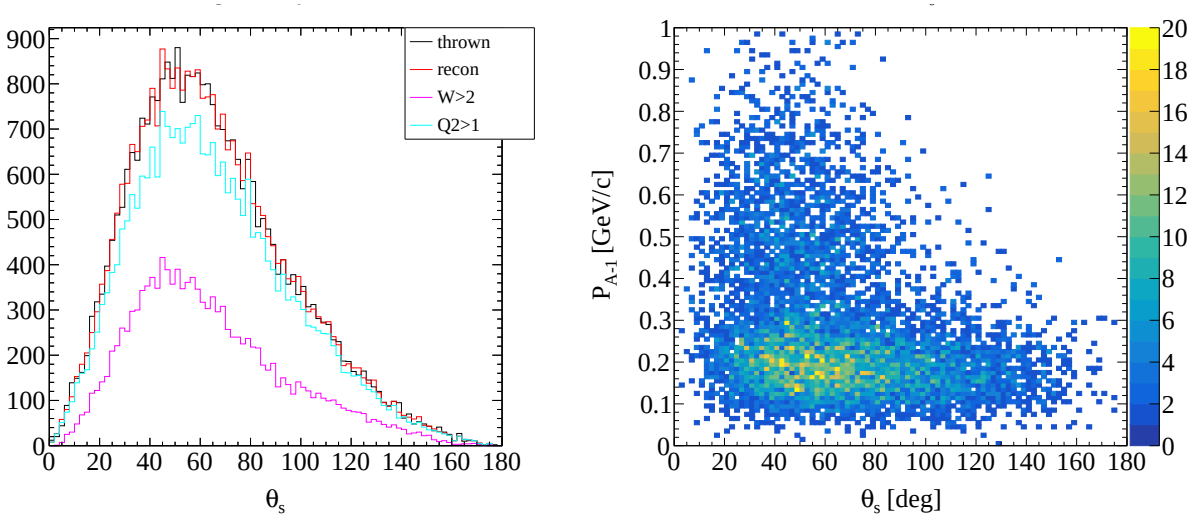

Figure 4.7: Left: Spectator recoil angle, θ_s, showing the generated and reconstructed values, also shown is the reconstructed with $Q^2 > 1$ GeV^2 and $W > 2$ GeV. Right: Spectator angle vs reconstructed spectator momentum.

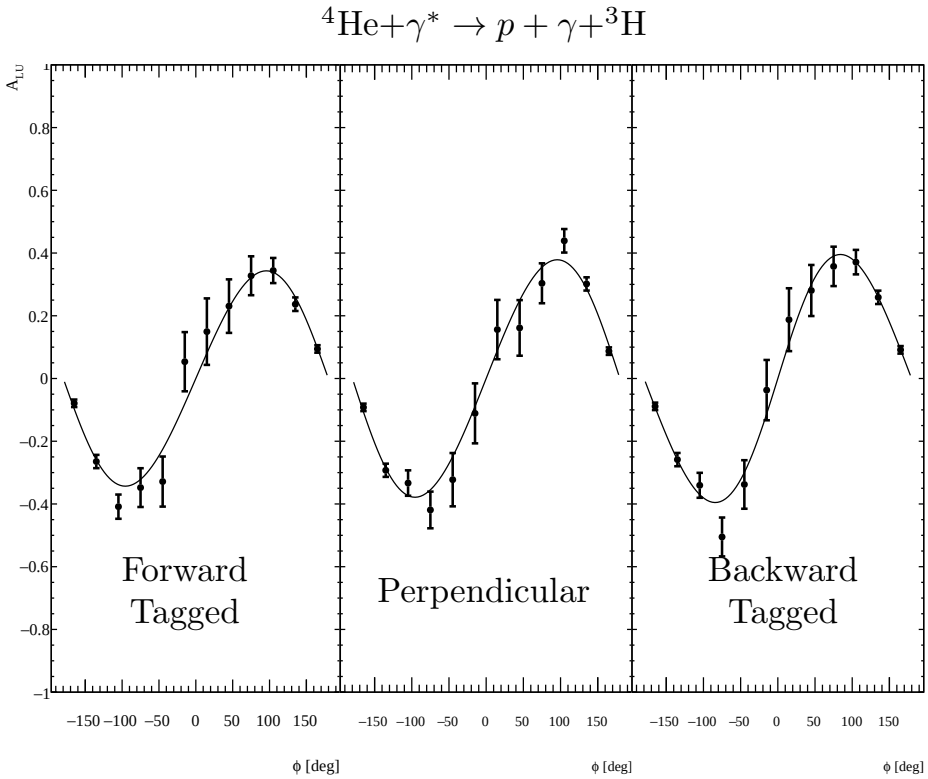

Figure 4.8: Projections for the statistical uncertainties on A_{LU} for three different bins in spectator angle, all corresponding to the lowest spectator momentum bin. The spectator angles are forward (left), perpendicular (center), and backward (right). Note the low momentum bin corresponds to the mean field nucleons.

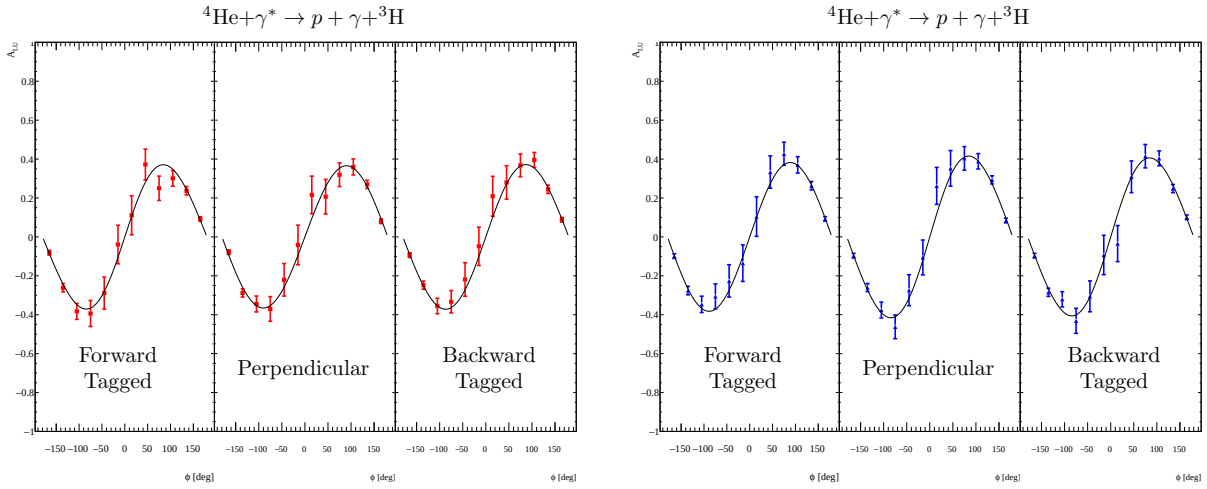

Figure 4.9: Expected statistical uncertainties of A_{LU} for θ_s bins identical to those in Figure 4.8, but these results show the two higher spectator momentum bins. Note the highest momenta (blue) correspond to SRC nucleons.

of the many kinematic settings, Figure 4.12 (left) shows the result of fitting the ϕ asymmetry for one bin in x, Q^2, and t.

For the n-DVCS measurements, the missing mass cut will select DVCS events. The primary assumption is what we will have already observed through the p-DVCS channel and isolated kinematics where FSIs are minimized. Typically, this corresponds to backward low momentum spectators. We will match the kinematics where the FSI are observed to be negligible for the proton and look for nuclear effects in neutron. We define the following ratio for the extracted α values from DVCS on a quasi-free neutron in ^{2}H and from DVCS on a bound neutron in ^{4}He:

$$R_\alpha^N = \frac{\alpha_{N^*}^{(^4\mathrm{He})}}{\alpha_N^{(^2\mathrm{H})}} \tag{4.2}$$

where the N^* indicates the bound nucleon. We will identify nuclear effects by observing deviations from unity in this ratio and extracting its trend as a function of x, and for various spectator kinematics limits where we expect mean field nucleons or SRC nucleons to dominate. The projected statistical uncertainty is shown in Figure 4.12 (right) and in Fig 4.13. See appendix C.2 for more BSA ratio projections.

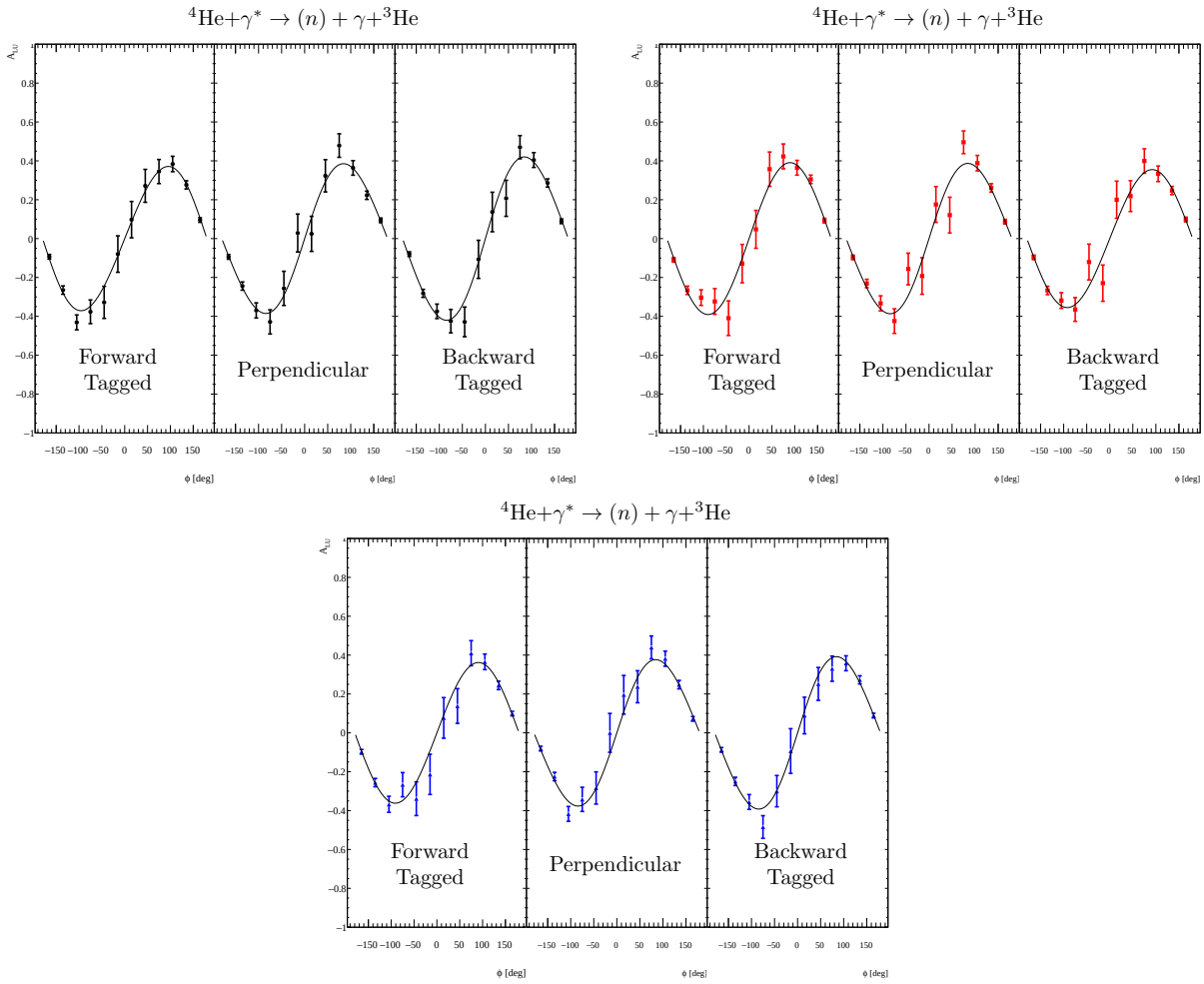

Figure 4.10: Projected statistical uncertainties A_{LU} for θ_s bins identical to those in Figure 4.8, for n-DVCS on ^{4}He measurement, in 9 different bins of spectator momentum and angle.

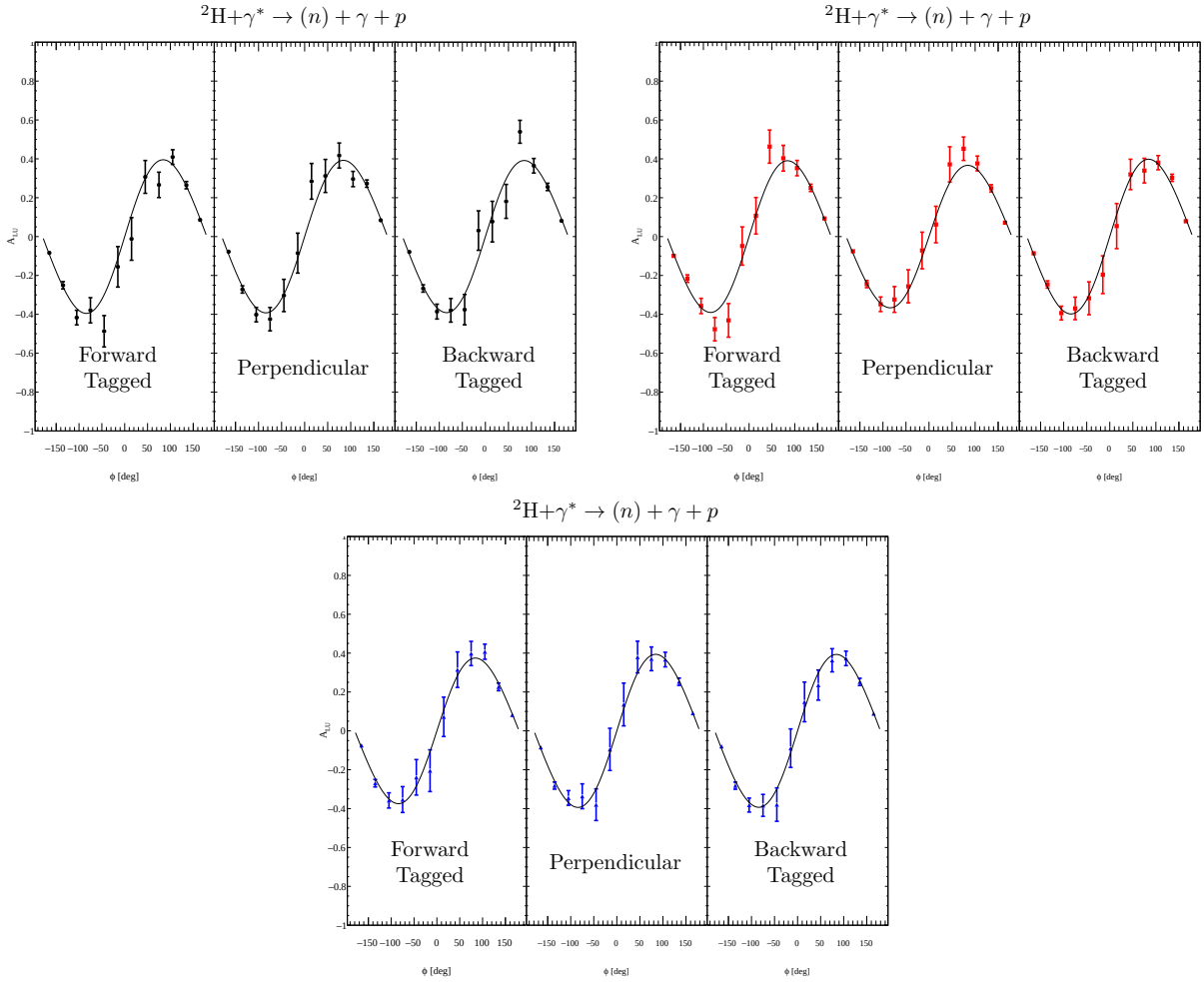

Figure 4.11: Projected statistical uncertainties A_{LU} for θ_s bins identical to those in Figure 4.8, for n-DVCS on ^{2}H measurement, in 9 different bins of spectator momentum and angle.

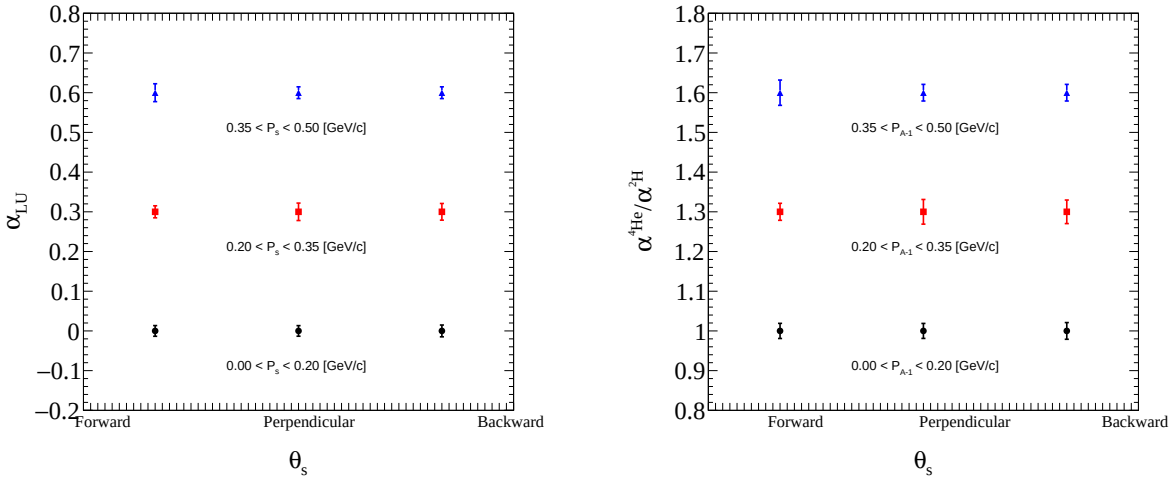

Figure 4.12: Left: Projected uncertainties after fitting the beam spin asymmetry with equation (4.1) to extract a value of α. Each bin in x, Q^2, and t has 3 bins in P_{A-1} and θ_s, which are offset vertically for clarity. Right: The ratio of αs for a bound neutron and a quasi-free nucleon.

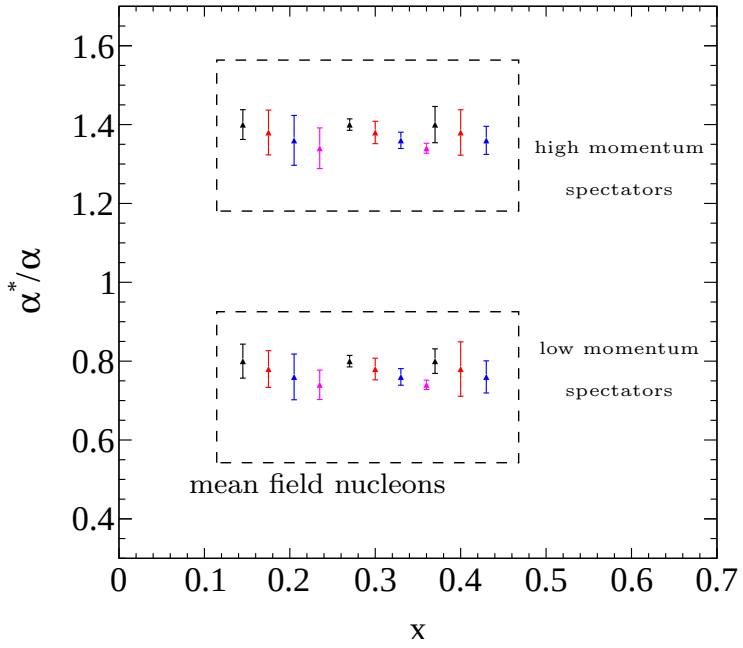

Figure 4.13: A subset of the R_α ratios for all Q^2 with backward tagged spectators. The highest spectator momenta bins are offset vertically above the lowest spectator momenta and the colors indicate the different t bins which are shifted horizontally for clarity.

Source	CLAS-eg6	CLAS12-ALERT	Systematic Type
Beam polarization	3.5%	3.5%	normalization
DVCS event selection	3.7%	1.0%	bin-to-bin
Acceptance ratio	2.0%	<1.0%	bin-to-bin
Radiative Corrections	2.0%	<1.0%	bin-to-bin
Others	0.1%	0.1%	
Total	5.5%	4.0%	

Table 4.2: Estimates of the expected systematic uncertainties compared to CLAS-eg6.

4.3.2 Systematic Uncertainties

We estimate the main sources of systematic uncertainties from those ultimately obtained for the CLAS-eg6 experiment's incoherent DVCS measurement [38]. They are listed in Table 4.2 along with our estimates for the beam spin asymmetry systematics. For the BSA the beam polarization will dominate our systematic uncertainties followed by the DVCS event selection cuts. With the significant improvement of ALERT for detecting the spectator recoils this uncertainty is expected to improve by more than a factor of two.

The so-called "acceptance ratio" corrects for the π^0 background and is defined for each bin as

$$R_{\pi^0} = \frac{N_{\pi(\gamma)}}{N_{\pi(\gamma\gamma)}} \tag{4.3}$$

where $N_{\pi(\gamma)}$ and $N_{\pi(\gamma\gamma)}$ are the rates for exclusive electro-production of π^0s where one decay photon is detected and where both decay photons are detected, respectively. The ratio calculated in Equation. 4.2 has the benefit that the acceptance cancels in the ratio under the approximation $R_{\pi^0}(^4\mathrm{He}) \simeq R_{\pi^0}(^2\mathrm{H})$.

External radiative effects on the electron side can be easily understood and studied using the over-determined kinematics. The exclusivity of the process allows tight cuts that remove any initial state radiation. Furthermore, much of the radiative effects will cancel in the ratio.

Chapter 5

Summary and Answers to PAC44

In this final chapter we first address issues and concern raised in the PAC44 report about the ALERT run group. Then, following a brief summary of the proposed experiment, we state the beam time request. Then we conclude by addressing this proposal's relation to other approved experiments.

5.1 Answers to PAC44 issues

Issues:

The Drift Chamber/scintillator technology needs to be demonstrated. We observe that a strong program of prototype studies is already underway.

Answer: We feel the technology has no major unknowns, wire chambers and scintillators have been used for decades as detectors of low energy nuclei and their properties have been well established. We present in the proposal a conceptual design demonstrating the feasibility of the detector, it is common practice to work on the optimization of a certain number of parameters after the proposal is approved. In particular, because it is easier to fund and man a project that has an approved status than a future proposal. Nevertheless, we remain open to discuss the topic in more depth if the committee has any concerns.

The TAC report voiced concerns about the length of the straw cell target and the substantial effort needed to integrate the DAQ for this detector into the CLAS12 DAQ.

Answer: The TAC and PAC44 raised concerns about the target cell. We have added extra discussion in section 3.3.3, which includes a table of existing or planned targets that are similar to the one we proposed. In summary, our proposed target is twice as wide as the ones used in the 6 GeV era for the BONuS and eg6 run and should therefore cause no issues. Note that the experiment 12-06-113 (BONuS12) is approved with a longer and thinner target. Their design will be reviewed by JLab for their experiment readiness review (ERR) before the PAC45 meeting. The result of this review should settle the question, but in any case, we propose a safer solution based on the successful experiments of the 6 GeV era.

The TAC and PAC44 raised issues regarding integration of ALERT into the CLAS12 DAQ. First, they raised a concern that the resources necessary for this integration are not clearly identified. We have added text in section 3.6.3 outlining the resources provided by each group and the technical support they are expected to provide. Secondly, they mentioned a concern about the "substantial effort needed to integrate the DAQ for this detector into the CLAS12 DAQ". We want to emphasize that the read-out systems for ALERT are already being used in the CLAS12 DAQ to readout Micromegas detectors. Therefore, we will use and build on the experience gained from these systems.

The proposal does not clearly identify the resources (beyond generic JLAB/CLAS12 effort) necessary for DAQ integration which may be a substantial project.

Answer: As mentioned above, we do not feel this contribution is major, nevertheless we made this part clearer in the proposal.

During review the collaboration discovered an error in converting the luminosity to beam current. This resulted in a revision that will either require doubling the current or the target density. The beam current change would require changes to the Hall B beam dump, while raising the target density could impact the physics reach of the experiment by raising the minimum momentum threshold.

Answer: During the PAC44 proposal submission process the wrong beam current was requested. It was a factor of 2 too low. This increased beam current brought into contention the issue of possible Hall B beam current limits. We chose to use the higher beam current in this new version. Based on discussions with the Hall-B and accelerator staff, the only necessary upgrade necessary to run at 1 µA is with the Hall-B beam blocker.

The precise interplay between final state interactions (FSI) and the tails of the initial state momentum distribution in DVCS on 4He was a topic of some debate. The collaboration makes an argument that the excellent acceptance of the apparatus allows novel constraints that allow selection of kinematic ranges where FSI is suppressed. While the originally suggested method to unambiguously identify areas of FSI was revised during the review, the committee remains unconvinced that the new kinematic selections suggested do not also cut

into interesting regimes for the initial state kinematics. The committee believes that this is model dependent and would like to see more quantitative arguments than were provided in this version of the proposal.

Answer: We acknowledge there was an overstatement of the possibilities of the Tagged-DVCS proposal on this topic, this has been corrected. We now show a reduction, in opposition to the complete suppression previously claimed, in events that differ from the PWIA result. This finding is based on a simulation using a simple model of FSIs together with a Monte-Carlo event generator.

Summary:

The committee was generally enthusiastic about the diverse science program presented in this proposal; in particular the tagged EMC studies and the unique study of coherent GPD's on the 4He nucleus. However, the substantial modifications made in the proposal during review indicate that it could be substantially improved on a reasonably short time scale. We would welcome a new proposal that addresses the issues identified by the committee and by the collaboration.

Answer: We hope that the new proposals will answer all the questions raised by the PAC44 and will make the physics case even more compelling.

We also note that there are multiple experiments, proposed and approved, to study the EMC effect, including several with novel methods of studying the recoil system. We appreciate the comparisons of recoil technologies in this proposal and would welcome a broader physics discussion of how the proposed measurements contribute to a lab-wide strategy for exploring the EMC effect.

Answer: While no strategy document has been drafted after them, we want to point out to the PAC that the community of physicist interested by the partonic structure of nuclei meets regularly, with often a large focus on what can be done at JLab (see workshops at Trento[1], Miami[2], MIT[3], and Orsay[4] for example). Nonetheless, we added in the tagged EMC proposal summary an extension about the 12 GeV approved experiments related to the EMC effect. This short annex will hopefully clarify the context and the uniqueness of the present experiments.

[1]New Directions in Nuclear Deep Inelastic Scattering http://www.ectstar.eu/node/1221

[2]Next generation nuclear physics with JLab12 and EIC https://www.jlab.org/indico/event/121/

[3]Quantitative challenges in EMC and SRC Research and Data-Mining http://web.mit.edu/schmidta/www/src_workshop/

[4]Partons and Nuclei https://indico.in2p3.fr/event/14438/

5.2 Summary and Beam Time Request

Spectator tagged DVCS on ^{2}H and ^{4}He is of critical importance for two reasons. First and foremost, it identifies the active nucleon in the DVCS process. Secondly, spectator tagging provides a handle on the initial nucleon momenta, *i.e.*, it allows us to separate the mean field nucleons from the short range correlated nucleons. Tagged incoherent DVCS uniquely provides important leverage for identifying and isolating final state interactions while simultaneously probing the struck nucleon at the parton level. Furthermore, the neutron beam spin asymmetry is very sensitive to nuclear effects (see section 1.2.2). Therefore cleanly extracting the neutron DVCS beam spin asymmetry, as we propose to do, in both bound and quasi-free configurations, will produce a *high impact result* from which we are able to *unambiguously* conclude that nucleons are modified in medium at the parton level. It also allows for the systematic control over FSIs needed to definitively observe modified nucleons.

In order to achieve the uncertainties presented in this proposal, we need 20 days of running at 11 GeV with helium target, 20 days at 11 GeV with deuterium, both with 80% longitudinally polarized beam, and 5 days of commissioning of the ALERT detector at 2.2 GeV with helium and hydrogen targets.

5.3 Relation to other experiments

This experiment will greatly complement many already approved experiments and previously conducted experiments.

First, the approved E12-11-003 experiment [55], "Deeply Virtual Compton Scattering on the Neutron with CLAS12 at 11 GeV" is set to measure the n-DVCS beam spin asymmetry by directly detecting the struck neutron in the reaction $\gamma^* + d \rightarrow n + \gamma + (p)$. While we intend to also measure the BSA through detection of the spectator proton instead, this is not the main thrust of this proposal. We aim to observe a medium modified neutron by also looking at a similar reaction on the neutron with a helium target where a spectator ^{3}He is detected.

The approved E12-06-113 experiment [19], "The Structure of the Free Neutron at Large x-Bjorken" will measure the neutron structure function in DIS through a spectator tagging of a recoil proton using the BONuS12 detector. The reaction $e + d \rightarrow e + p_s + (X)$ is aimed at the deuteron's quasi-free neutron, as is our DVCS BSA with a deuteron target. However, we will also investigate the bound neutron. Our main result will be the ratio of the BSA $\sin\phi$ harmonics from bound and quasi-free neutrons, which is a *model independent observable*.

Because we will study the FSIs through the fully detected final state, as highlighted throughout this proposal, we will be able to directly test the validity of the PWIA over a wide range of spectator kinematics. This information will directly benefit both experiments mentioned (and many more). The knowledge of the FSIs can be used to tune the models needed to extract the on-shell neutron structure function. Furthermore, the neutron DVCS observable will also be sensitive to FSIs which can be further understood with the results of this experiment.

Appendix A

The Kinematics of Spectator-Tagged DVCS

This appendix defines and discuses the kinematics of spectator-tagged DVCS. We will begin by defining the basic kinematic variables and the plane-wave impulse approximation (PWIA). This is followed by an analysis of the fully exclusive kinematics where all final-state particles are detected and a discussion of how to leverage this extra information for studying FSIs.

A.1 Incoherent DVCS Kinematic Variables

A.1.1 Experimentally Measured Variables

The four-momenta in the tagged incoherent DVCS reaction are defined in Figure A.1. The momenta are explicitly

$$k_1 = (k_1, \boldsymbol{k}_1 \simeq k_1^0) \qquad k_2 = (k_2, \boldsymbol{k}_2 \simeq k_2^0) \qquad \text{for } e \text{ and } e', \tag{A.1}$$

$$q_1 = (\nu_1, \boldsymbol{q}_1) \qquad q_2 = (\nu_2, \boldsymbol{q}_2) \qquad \text{for } \gamma^* \text{ and } \gamma, \tag{A.2}$$

$$p_1 = (E_1, \boldsymbol{p}_1) \qquad p_2 = (E_2, \boldsymbol{p}_2) \qquad \text{for initial and struck nucleon,} \tag{A.3}$$

$$p_A = (M_A, \boldsymbol{0}) \qquad p_{A-1} = (E_{A-1}, \boldsymbol{p}_{A-1}) \qquad \text{for target and spectator nucleus,} \tag{A.4}$$

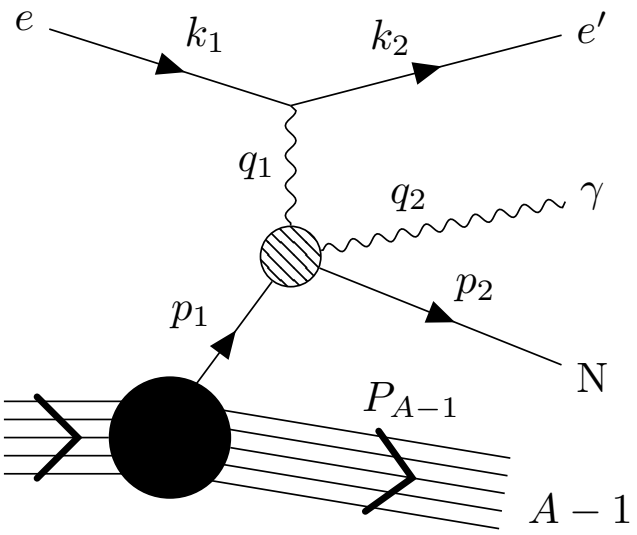

Figure A.1: Tagged incoherent DVCS with labeled momenta.

and the virtual and real photon momenta are

$$|\boldsymbol{q}_1| = \sqrt{Q^2 + \nu_1^2} \qquad \text{and} \qquad |\boldsymbol{q}_2| = \nu_2\,. \tag{A.5}$$

The virtual photon energy and four-momentum squared are

$$\nu_1 = k_1^0 - k_2^0 \qquad \text{and} \qquad Q^2 = -q_1^2 = -(k_1 - k_2)^2 \simeq 4k_1^0 k_2^0 \sin^2(\theta_{k_1 k_2}). \tag{A.6}$$

For the remainder of this chapter we will be considering the process where all particles are detected, i.e., ^{4}He$(e, e'\,\gamma\, p\,+^3$H). The incident and scattered electron momenta are experimentally well-determined, thus, the virtual photon four-momentum is well defined. The real photon energy and direction is measured in the electromagnetic calorimeter and the struck nucleon is also detected in the forward CLAS12 detector. The spectator system is identified in ALERT, which also measures its momentum. And finally the initial nucleus is at rest with mass M_A. Therefore all the momenta in equations A.1–A.4 (and Figure A.1) are determined with the exception of the initial struck nucleon, p_1. We will return to determining this in section A.2.

A.1.2 Momentum Transfer

The Mandelstam variable t is the square of the momentum transfer and can be calculated on the photon side of the diagram or the hadron side of the diagram as illustrated in Figure A.2. We define the former as

$$t_q = (q_1 - q_2)^2 \tag{A.7}$$
$$= -Q^2 - 2\nu_2(\nu_1 - q_1 \cos\theta_{q_1 q_2}) \tag{A.8}$$

and the latter as

$$t_p = (p_1 - p_2)^2 \tag{A.9}$$
$$= 2M^2 - 2(E_1 E_2 - \boldsymbol{p}_1 \cdot \boldsymbol{p}_2). \tag{A.10}$$

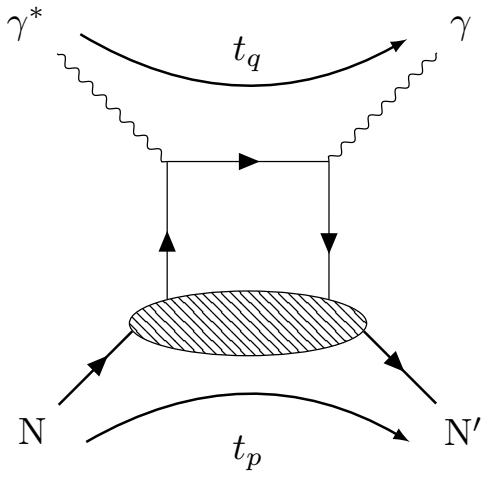

Figure A.2: The DVCS handbag diagram showing the two ways the momentum transfer can be calculated.

A.1.2.1 Nucleon at Rest

For DVCS on a fixed proton target, the momentum transfer can be calculated from the virtual photon momentum, q_2, and the *direction* of the real photon, $\hat{\boldsymbol{q}}_2$ =

$(\cos\phi_{q_2}\sin\theta_{q_2}, \sin\phi_{q_2}\sin\theta_{q_2}, \cos\theta_{q_2})$. The momentum transfer squared in this case is calculated as

$$\boxed{t_{\gamma\gamma} = \frac{-Q^2 - 2\nu_1(\nu_1 - q_1\cos\theta_{q_1q_2})}{1 + (\nu_1 - q_1\cos\theta_{q_1q_2})/M}} \tag{A.11}$$

where the angle between the virtual and real photons is $\theta_{q_1q_2}$.

Derivation 1: $t_{\gamma\gamma}$ for nucleon at rest.
Equation (A.11) is obtained from equation (2.16) and the real photon's energy determined using the initial nucleon at rest. Using the struck nucleon's invariant mass we get

$$\begin{aligned} p_2^2 &= M^2 \\ &= M^2 - Q^2 + 2\left(M_1(\nu_1 - \nu_2) - \nu_1\nu_2 + \boldsymbol{q}_1\cdot\boldsymbol{q}_2\right). \end{aligned}$$

This equation becomes

$$\frac{Q^2}{2} = \nu_1 M_1 - \nu_2 M_1 - \nu_1\nu_2 + \boldsymbol{q}_1\cdot\boldsymbol{q}_2 \tag{A.12}$$

which can be solved for ν_2 to yield

$$\boxed{\nu_2 = \frac{Q^2/2 - \nu_1 M}{|\boldsymbol{q}_1|\cos\theta_{q_1q_2} - M - \nu_1}\,.} \tag{A.13}$$

Putting (A.13) into (A.8) yields the result of (A.11).

A.1.2.2 Bound Nucleon with Fermi Motion

Equation (A.11) is a special case of the more general situation where the initial nucleon is not at rest in the lab frame. This is the case for a nucleon with non-zero Fermi motion or an electron-proton collider lab frame. Unlike the nucleon at rest case we cannot eliminate *both* p_1 and p_2, instead, we have only the option of eliminating one. This is not a problem for an electron-proton collider, where p_1 is constant, since we can just boost to the frame with $p_1 = (M, \mathbf{0})$ and the analysis can be carried out consistently. However, a bound nucleon in a nucleus makes for a lousy collider because every scattering event would require a unique analysis frame.

It should be emphasized that the two possible choices above lead to a unique opportunity for studying tagged DVCS where the final state is fully detected. We will return to this in

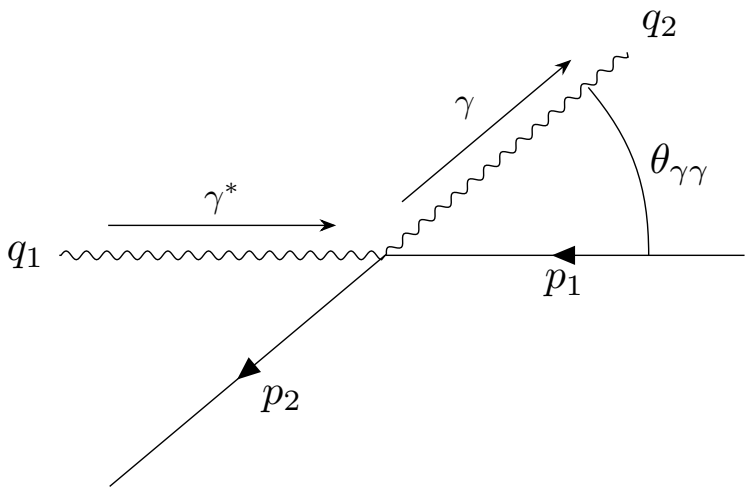

Figure A.3: Nucleon-photon center-of-momentum system.

section A.2.2 only after defining the PWIA in section A.2.

A.1.3 $t_{\mathbf{min}}$ and $t_{\mathbf{max}}$

The minimum and maximum momentum transfer are easily understood in the virtual photon-nucleon center-of-momentum (CM) frame which is shown in Figure A.3. We begin by deriving the real photon's energy in this frame which will be useful for deriving further relations between frames.

Derivation 2: Real photon energy in the CM frame.
The center-of-mass energy squared calculated from the final state momenta is

$$s = M^2 + 2(E_2\nu_2 + |\boldsymbol{p}_2||\boldsymbol{q}_2|) \tag{A.14}$$

$$= M^2 + 2\nu_2(\sqrt{\nu_2^2 + M^2} + \nu_2) \tag{A.15}$$

where we have used the CM relation $\boldsymbol{p}_2 = -\boldsymbol{q}_2$ and the fact that the final state nucleon and photon are both on-shell. Solving (A.15) for ν_2 yields

$$\boxed{\nu_2^{CM} = \frac{s - M^2}{2\sqrt{s}}} \tag{A.16}$$

where we label the result explicitly as a CM value.

The minimum momentum transfer corresponds to the scenario in the CM system where the virtual photon loses just enough momentum as to become on-shell. That is, it transfers only enough momentum to become a real photon and continues to propagate in the same direction. This corresponds to the case where $\theta_{\gamma\gamma} = 0$. Using this value in (A.8) gives

$$\boxed{t_{\min} = -Q^2 - \left(\frac{s - M^2}{\sqrt{s}}\right)(\nu_1^{CM} - q_1^{CM})} \tag{A.17}$$

where we have explicitly labeled the frame dependent quantities. Quite similarly, the maximum momentum transfer corresponds to the case where the particles scatter in the opposite direction of their initial momentum. This corresponds to $\theta_{\gamma\gamma} = \pi$, yielding the maximum momentum transfer

$$\boxed{t_{\max} = -Q^2 - \left(\frac{s - M^2}{\sqrt{s}}\right)(\nu_1^{CM} + q_1^{CM})}. \tag{A.18}$$

As a check, in the case of a real initial photon ($Q^2 = 0$),

$$t_{\min} \to 0 \qquad \text{and} t_{\max} \to \left(\frac{M^2 - s}{\sqrt{s}}\right) 2\nu_1^{CM}. \tag{A.19}$$

In the high energy limit were $M^2 \ll s$ or in the massless case where M terms are neglected we find

$$s \to (2\nu_1^{CM})^2 \qquad \text{and} \qquad t_{\max} \to -s \tag{A.20}$$

where we find the maximum momentum transfer is simply all the available momentum.

We now need relations for the CM energies between the photon-nucleon CM frame, lab frame, and the frame where the initial nucleon is at rest. The CM energy squared in each of these frames is

$$s = -Q^2 + M^2 + 2\left(\nu_1 E_1 - |\boldsymbol{q}_1||\boldsymbol{p}_1|\cos\theta_{p_1 q_1}\right) \qquad \text{any frame} \tag{A.21}$$

$$s = -Q^2 + M^2 + 2\left(\nu_1^R M\right) \qquad p_1 \text{ rest frame} \tag{A.22}$$

$$s = -Q^2 + M^2 + 2\left(\nu_1^{CM}\sqrt{|\boldsymbol{q}_1^{CM}|^2 + M^2} - |\boldsymbol{q}_1^{CM}|^2\right) \qquad \text{CM frame} \tag{A.23}$$

where the rest frame and CM frame variables are labeled with R and CM, respectively, while the lab frame variables are not labeled.

Using (A.21) and (A.22) we find the relation between the nucleon rest frame and the lab

$$\nu_1^R = \frac{1}{M}\left(\nu_1 E_1 - |\boldsymbol{p}_1||\boldsymbol{q}_1|\cos\theta_{p_1 q_1}\right) \qquad \text{Lab to nucleon rest frame} \tag{A.24}$$

and similarly for (A.23) and (A.22)

$$\nu_1^R = \frac{1}{M}\left(\nu_1^{CM}\sqrt{|\boldsymbol{q}_1^{CM}|^2 + M^2} + |\boldsymbol{q}_1^{CM}|^2\right) \qquad \text{CM to nucleon rest frame.} \tag{A.25}$$

Equation A.25 can be turned around and solved for ν_1^{CM} since we need it to calculate the kinematic limits above. This gives

$$\boxed{\nu_1^{CM} = \sqrt{\frac{\left(M\nu_1^R - Q^2\right)^2}{M^2 + 2M\nu_1^R - Q^2}}} \tag{A.26}$$

which, along with (A.24), can be quite useful for evaluating t_{min} and t_{max}.

A.2 Plane Wave Impulse Approximation

In the following sections we discuss the plane-wave impulse approximation and how it *provides a framework for comparison*, even for kinematics where it is not expected to apply. We conclude with a detailed discussion of the kinematic issues raised around about Fermi motion in section A.1.2.2.

A.2.1 PWIA Definition

The plane-wave impulse approximation is a simple model for calculating an incoherent scattering from a bound nucleon. The PWIA assumes [56] i) the virtual photon is absorbed by a single nucleon, and ii) this nucleon is also the nucleon detected, and iii) this nucleon leaves the nucleus without interacting with the A-1 spectator system. This implies the recoiling spectator system has a momentum opposite that of the initial struck nucleon,

$$\boldsymbol{p}_1 = -\boldsymbol{p}_{A-1}. \tag{A.27}$$

Furthermore, this approximation also implies that the spectator system is on-shell, *i.e.*,

$$E_{A-1} = \sqrt{|\boldsymbol{p}_{A-1}|^2 - M_{A-1}^2}. \tag{A.28}$$

Noting the initial nucleon can be off-shell, we introduce the following definition of the initial nucleon's invariant mass

$$p_1^2 = \bar{M}^2 \neq M_N^2. \tag{A.29}$$

The "off-shellness" of the struck nucleon is typically characterized by $0.7 \lesssim \bar{M}/M_N < 1$.

A.2.2 FSI and Off-shellness

From its definition, the PWIA implies all the "off-shellness" goes with initial nucleon. Where this not the case, the spectator system would be left off-shell, and thus, necessitate some final state interaction to put it on-shell prior to detection. So here we should emphasize that the PWIA is not used throughout this proposal because the authors think it is a correct or even a good approximation, but rather, *because it provides a basis for comparison.*

A.2.3 Measuring Off-shellness in the PWIA

The off-shell mass of the nucleon can be determined two different ways with the PWIA and a fully detected final state. Starting first with the direct approach using the spectator

$$\begin{aligned} \bar{M}_{(0)}^2 &= (p_A - p_{A-1})^2 \\ &= M_A^2 + M_{A-1}^2 - 2M_A E_{A-1}. \end{aligned} \tag{A.30}$$

The momenta used in this calculation are highlighted in Figure A.4's left diagram. The second way to calculate the off-shell mass is to use the invariant p_1^2 with all the other momenta not used in the previous calculation. This yields

$$\begin{aligned} \bar{M}_{(1)}^2(q_1, q_2, p_2) = M^2 - Q^2 + 2E_2(\nu_1 + \nu_2) \\ - 2\left(\nu_1\nu_2 + \nu_2|\boldsymbol{p}_2|\cos\theta_{p_2q_2} - \nu_2|\boldsymbol{q}_1|\cos\theta_{q_1q_2} + |\boldsymbol{p}_2||\boldsymbol{q}_1|\cos\theta_{p_2q_1}\right). \end{aligned} \tag{A.31}$$

The last way we calculate $\bar{M}$ is to start with the struck nucleon invariant mass to eliminate p_2 from the expression. This results in a slight more complicated expression:

$$\bar{M}_{(2)}^2(q_1, q_2, p_1) = \frac{1}{2(\nu_1 - \nu_2)}\sqrt{(a_{\bar{M}} + Q^2 + 2\boldsymbol{q}_1\cdot\boldsymbol{p}_1)(b_{\bar{M}} + Q^2 + 2\boldsymbol{q}_1\cdot\boldsymbol{p}_1)} \tag{A.32}$$

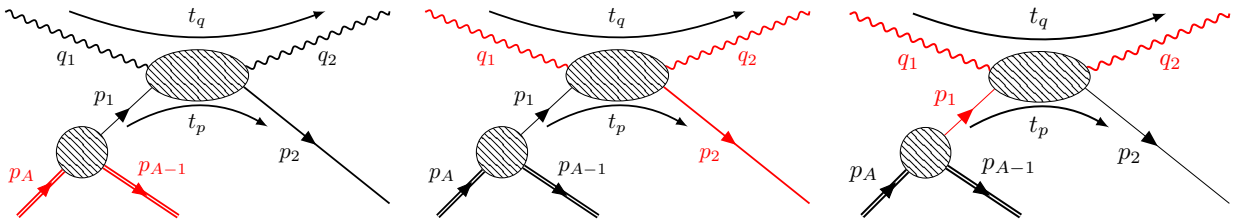

Figure A.4: Highlighted in red are the momenta used to calculate the off-shell mass. The diagrams from left to right correspond to $\bar{M}_{(0)}$ (A.30), $\bar{M}_{(1)}$ (A.31), and $\bar{M}_{(2)}$ (A.32).

where

$$a_{\bar{M}} = 2\nu_1(\nu_2 + |\boldsymbol{p}_1|) - 2\nu_2|\boldsymbol{p}_1|(\cos\theta_{p_1q_2} + 1 + \frac{|\boldsymbol{q}_1|}{|\boldsymbol{p}_1|}\cos\theta_{q_1q_2}) \tag{A.33}$$

$$b_{\bar{M}} = 2\nu_1(\nu_2 - |\boldsymbol{p}_1|) - 2\nu_2|\boldsymbol{p}_1|(\cos\theta_{p_1q_2} - 1 + \frac{|\boldsymbol{q}_1|}{|\boldsymbol{p}_1|}\cos\theta_{q_1q_2}). \tag{A.34}$$

The initial nucleon momentum, $\boldsymbol{p}_1$, is calculated from the target and spectator nuclei using the PWIA. It is worth noting that $\bar{M}_{(1)}$ does not depend on p_1 and $\bar{M}_{(2)}$ does not depend on p_2. The dependent momenta for each calculation are shown in Figure A.4.

A.2.4 Photon Energy as FSI Indicator

Calculating ν_2. Using the over-determined kinematics we can calculate the real photon energy two different ways.

Derivation 3: $\nu_2(p_2, \hat{\boldsymbol{q}}_2, \bar{M}, q_1)$

$$\begin{aligned} p_2^2 &= M^2 \\ &= -Q^2 + \bar{M}^2 + 2\left(E_1(\nu_1 - \nu_2) - \nu_1\nu_2 - (\boldsymbol{q}_1 - \boldsymbol{q}_2)\cdot\boldsymbol{p}_1 + \boldsymbol{q}_1\cdot\boldsymbol{q}_2\right). \end{aligned} \tag{A.35}$$

The last equation becomes

$$\frac{M^2 - \bar{M}^2 + Q^2}{2} = \nu_1 E_1 - \nu_2 E_1 - \nu_1\nu_2 - \boldsymbol{q}_1\cdot\boldsymbol{p}_1 + \boldsymbol{q}_2\cdot\boldsymbol{p}_1 + \boldsymbol{q}_1\cdot\boldsymbol{q}_2 \tag{A.36}$$

which can be solved for ν_2 to yield

$$\boxed{\nu_2^{(1)} = \frac{(M^2 - \bar{M}^2 + Q^2)/2 - \nu_1 E_1 + |\boldsymbol{q}_1|\,|\boldsymbol{p}_1| \cos\theta_{p_1 q_1}}{|\boldsymbol{q}_1| \cos\theta_{q_1 q_2} + |\boldsymbol{p}_1| \cos\theta_{p_1 q_2} - E_1 - \nu_1}}. \tag{A.37}$$

In the case of an on-shell nucleon at rest in the lab ($|\boldsymbol{p}_1| \to 0$), (A.37) reduces to (A.13).

Derivation 4: $\nu_2(p_2, \hat{\boldsymbol{q}}_2, \bar{M}, q_1)$
Solving for the invariant mass of p_1

$$\begin{aligned} p_1^2 &= \bar{M}^2 \\ &= -Q^2 + M^2 + 2\Big(\nu_2(q_1 \cos\theta_{q_1 q_2} - \nu_1 + E_2 - |\boldsymbol{p}_2| \cos\theta_{p_2 q_2}) \\ &\quad - \nu_1 E_2 + |\boldsymbol{q}_1||\boldsymbol{p}_2| \cos\theta_{q_1 p_2}\Big) \end{aligned} \tag{A.38}$$

This becomes

$$\boxed{\nu_2^{(2)} = \frac{(\bar{M}^2 - M^2 + Q^2)/2 + \nu_1 E_2 - |\boldsymbol{q}_1||\boldsymbol{p}_2| \cos\theta_{q_1 p_2}}{|\boldsymbol{q}_1| \cos\theta_{q_1 q_2} - |\boldsymbol{p}_2| \cos\theta_{p_2 q_2} - \nu_1 + E_2}}. \tag{A.39}$$

Calculating t. We can now put solutions (A.37) and (A.39) into (A.8) to obtain the analogues of $t_{\gamma\gamma}$ in (A.11) for the case of a bound nucleon with Fermi motion as discussed in section A.1.2.2. The results are

$$\boxed{t_q^{(1)} = -Q^2 - 2(\nu_1 - |\boldsymbol{q}_1| \cos\theta_{q_1 q_2}) \frac{(M^2 - \bar{M}^2 + Q^2)/2 - \nu_1 E_1 + |\boldsymbol{q}_1|\,|\boldsymbol{p}_1| \cos\theta_{p_1 q_1}}{|\boldsymbol{q}_1| \cos\theta_{q_1 q_2} + |\boldsymbol{p}_1| \cos\theta_{p_1 q_2} - E_1 - \nu_1}} \tag{A.40}$$

and

$$\boxed{t_q^{(2)} = -Q^2 - 2(\nu_1 - |\boldsymbol{q}_1| \cos\theta_{q_1 q_2}) \left[\frac{(\bar{M}^2 - M^2 + Q^2)/2 + \nu_1 E_2 - |\boldsymbol{q}_1||\boldsymbol{p}_2| \cos\theta_{q_1 p_2}}{|\boldsymbol{q}_1| \cos\theta_{q_1 q_2} - |\boldsymbol{p}_2| \cos\theta_{p_2 q_2} - \nu_1 + E_2}\right]}. \tag{A.41}$$

Identifying significant FSIs. The equations above for ν_2 and t require the off-shell mass, so we use the first PWIA result $\bar{M}_{(0)}$ in (A.30). To quickly summarize the procedure:

$$\Big[\text{Eq. (A.31)}\Big] \longrightarrow \quad \bar{M}^{\text{calc}} = \bar{M}_{(1)}(p_2, \hat{\boldsymbol{q}}_2, \nu_2^{\text{exp}}) \tag{A.42}$$

$$\Big[\text{Eq. (A.39)}\Big] \longrightarrow \quad \nu_2^{\text{calc}} = \nu_2^{(1)}(p_1, \hat{\boldsymbol{q}}_2, \bar{M}_{(0)}) \tag{A.43}$$

$$\Big[\nu_2^{\text{calc}} \neq \nu_2^{\text{exp}}, \bar{M}^{\text{calc}} \neq \bar{M}_{(0)}\Big] \longrightarrow \quad \text{PWIA modified by FSI.} \tag{A.44}$$

In the case where the initial nucleon is on-shell, this reduces to checking ν_2^{exp} against (A.39). Furthermore, the momentum transfer can be calculated from equation (A.40) and compared against t_q to verify that we are indeed identifying those events where they differ significantly due to FSIs. This analysis can be turned around, *i.e.*, p_1 and p_2 can be swapped in the procedure above:

$$\Big[\text{Eq. (A.32)}\Big] \longrightarrow \quad \bar{M}^{\text{calc}} = \bar{M}_{(2)}(p_1, \hat{\boldsymbol{q}}_2, \nu_2^{\text{exp}}) \tag{A.45}$$

$$\Big[\text{Eq. (A.37)}\Big] \longrightarrow \quad \nu_2^{\text{calc}} = \nu_2^{(2)}(p_2, \hat{\boldsymbol{q}}_2, \bar{M}_{(0)}) \tag{A.46}$$

$$\Big[\nu_2^{\text{calc}} \neq \nu_2^{\text{exp}}, \bar{M}^{\text{calc}} \neq \bar{M}_{(0)}\Big] \longrightarrow \quad \text{PWIA modified by FSI.} \tag{A.47}$$

Similarly, comparisons of (A.41) to t_q can be used to to determine the effectiveness of selection cuts. We now will turn our attention to this point and try to understand things with a toy model of FSIs.

A.3 Toy Model of FSIs

In this section we discuss a simple toy model of FSIs which was developed in order to understand the usefulness of the fully measured final state. First, we will discuss the toy model and emphasize that more theoretical work *or experimental data* is needed before the models can be taken seriously. Then we will use the model to test how well the analysis outlined above isolates the events with kinematics that are inconsistent with the PWIA due to significant FSIs.

A.3.1 Modeling the FSI

The FSIs were modeled as a single momentum exchange as illustrated in Figure A.5. This is obviously far from realistic since any rigorous treatment will require amplitude-level

calculations. However, as was already emphasized, we aim to separate those events which are no longer consistent with the PWIA using the momentum measured in the final state. This leaves those events where the FSI exchange produces little kinematic difference from the PWIA but may affect the cross section at the amplitude level. With these things in mind, we can proceed with the details of the toy model.

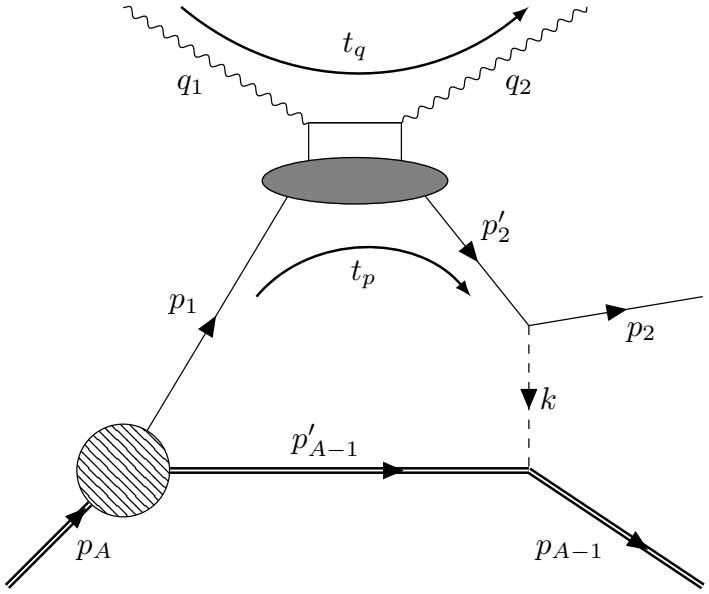

Figure A.5: A toy model of FSIs.

To get a feel for the size of the off-shell nucleon in the PWIA, it is worth pointing out that the mass difference between ^{4}He and ^{3}H is

$$M_{^4\mathrm{He}} - M_{^3\mathrm{H}} = (3.7284 - 2.80943)\ \mathrm{GeV/c^2} \tag{A.48}$$
$$= 0.91897\ \mathrm{GeV/c^2} \tag{A.49}$$
$$= 0.97945 M_p \tag{A.50}$$

and the mass difference between ^{4}He and ^{3}He is

$$M_{^4\mathrm{He}} - M_{^3\mathrm{He}} = (3.7284 - 2.80941)\ \mathrm{GeV/c^2} \tag{A.51}$$
$$= 0.91899\ \mathrm{GeV/c^2} \tag{A.52}$$
$$= 0.97943 M_p\ . \tag{A.53}$$

These differences give a rough estimate of the expected off-shellness in the case there are no FSIs present.

A straightforward Monte Carlo was generated, and in order simplify the present analysis,

the virtual photon kinematics were held fixed at

$$\nu_1 = 9 \text{ GeV}, \qquad Q^2 = 2.65 \text{ GeV}^2,$$

where for a nucleon at rest this would correspond to $x = 0.157$. The final state was uniformly sampled from the Lorentz invariant phase space, that is, there is no physics in the generated events and therefore all the results shown are purely a result of kinematics. However, The initial nucleon momentum was sampled from an empirical fit to the nucleon momentum distributions and the direction isotropic. The FSI momentum exchanged was also isotropic with a value uniformly sampled in the range of $0 < k < 0.2$ GeV/c.

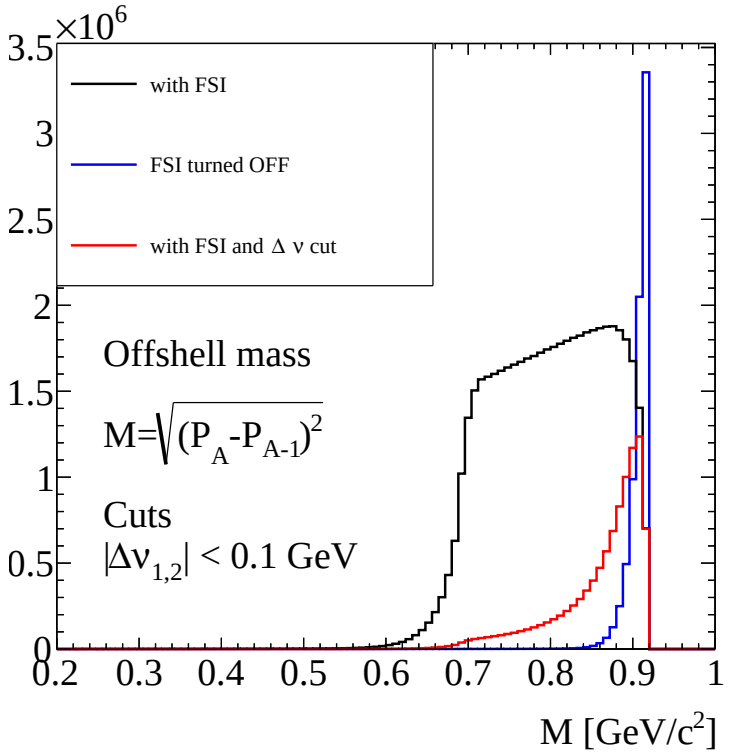

Figure A.6: The initial nucleon invariant mass without FSI (blue and reduced by a factor of 5), with FSI turned on (black), and with the selection cut (red). See text for more details.

A.3.2 Toy MC Results

We now follow the analysis outlined section A.2.4. The results for the invariant mass of the initial nucleon calculated with and without FSIs are shown in Figure A.6. Also shown in

red are the events that pass a selection cuts:

$$\Delta\nu_1^{(1)} > 0.1 \text{ GeV}, \qquad \text{and} \qquad \Delta\nu_1^{(2)} > 0.1 \text{ GeV}. \tag{A.54}$$

Furthermore, the results for $\Delta\nu_{(1,2)} = \nu_2^{exp} - \nu_2^{(1,2)}$ are shown in Figure A.8.. The dashed histograms have a cut on the invariant mass $M_0 > 0.8$ GeV/c^2.

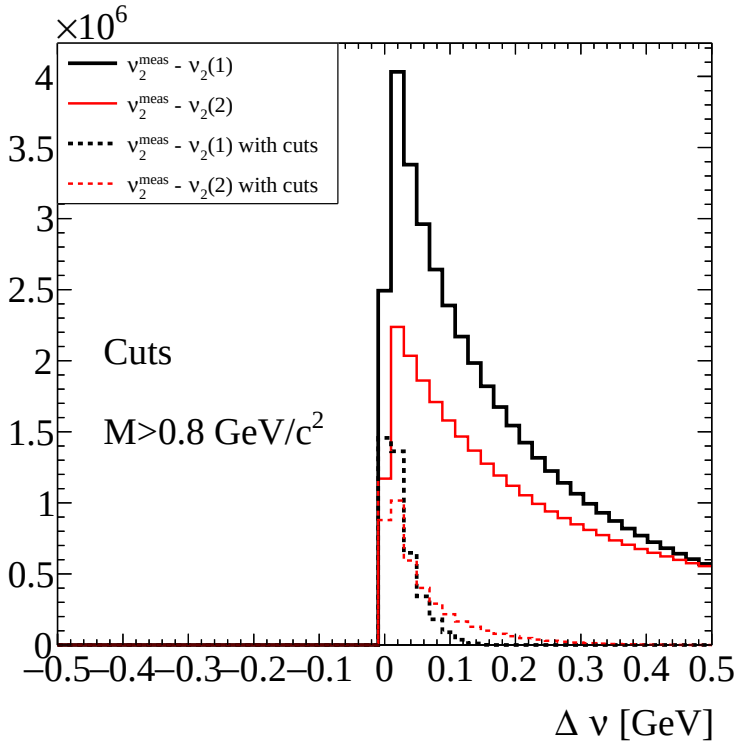

Figure A.7: The real photon momentum difference as calculated in equation (A.54).

The differences between the experimental momentum transfers are shown in Figure A.8. They are defined as

$$\Delta t_{(1,2)} = t_q - t_q^{(1,2)} \tag{A.55}$$

where $t_q^{(1,2)}$ are calculated from (A.40) and (A.41) respectively, and t_q is computed using the directly measured virtual and real photons.

Figures A.6, A.7, and A.8 clearly show that events with significant FSIs which result in kinematic differences from the PWIA can be isolated. The fully exclusive measurement will allow for a unique opportunity to study FSIs in this manner.

In order to see the impact of these cuts we take a look at the distribution of events versus spectator angle in a fixed bin of (x, Q^2, t, P_s). We form the ratio of distributions where the

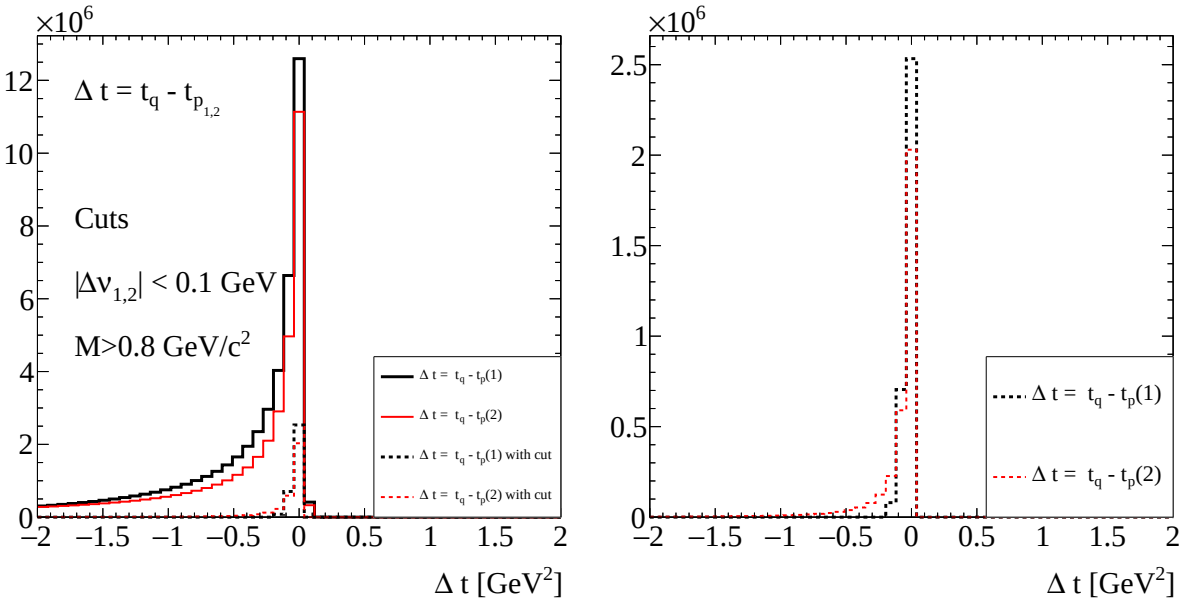

Figure A.8: The results of equation (A.55) without selection cuts (solid) and with selection cuts (dashed). The right plot shows only the results after selection cuts.

denominator is the distribution of all events in that bin and numerator includes the specific cuts to select a certain type of FSI (small or large momentum exchange). This ratio is defined as

$$R = A\frac{N(x, Q^2, t, P_s|\text{FSI cut})}{N(x, Q^2, t, P_s)}, \tag{A.56}$$

where A is an arbitrary normalization chosen so that the ratio of backward, low-P_s, and small k_0^{FSI} is about 1. The efficacy of such a cut, as outlined above, at removing events with significant FSIs can be seen in Figure A.9. For simplicity we limit ourselves to two bins in P_s (high and low). We can compare the result against its (unrealistic) counterpart by cutting on the FSI momentum exchange as well, i.e., $k_0^{\text{FSI}} < 15$ MeV or $k_0^{\text{FSI}} > 15$ MeV which correspond to the solid and dashed histograms in Figure A.10.

A.3.2.1 Noteworthy Features

Here we note some observations which are not integral to this proposal but are rather interesting. As Figure A.10 shows, the experimental cuts quite effectively act like a cut on the FSI momentum exchanged. Using this to our advantage we could take this one step further and isolate the effects for a given momentum exchange by systematically varying the effective

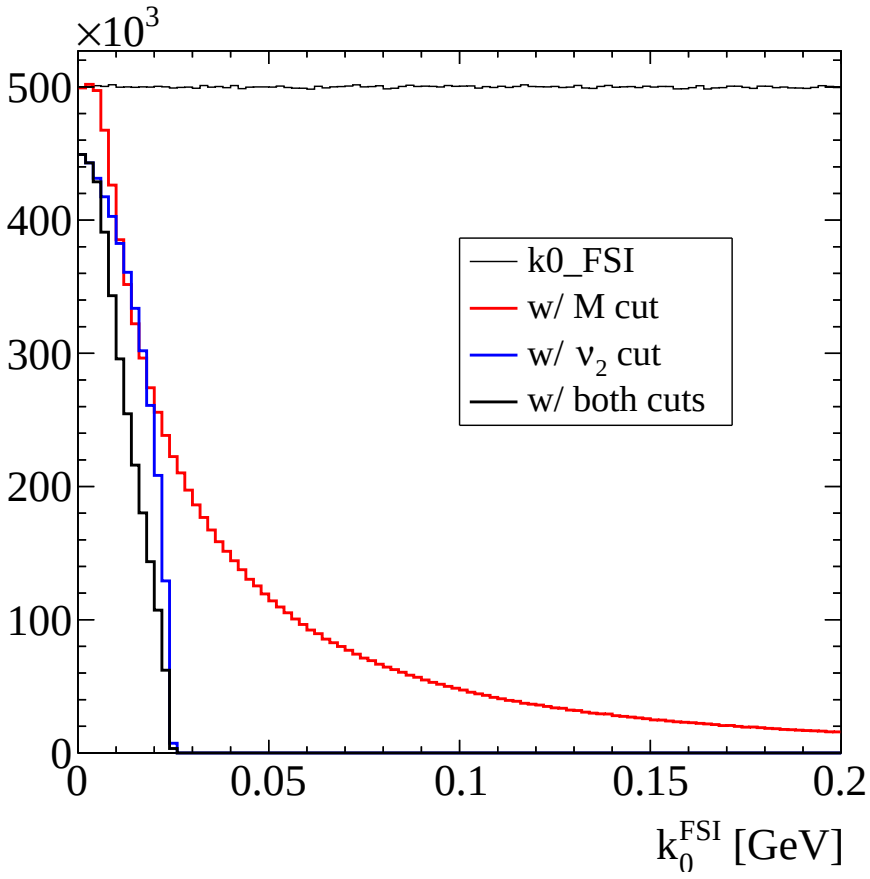

Figure A.9: The generated FSI momentum exchange with different cuts applied to select events with small k_0^{FSI}.

k_0^{FSI} cut (e.g. by loosening the values) and subtracting the difference[1]. However, we must remember that this is just a crude model and reality may be quite different. Furthermore, even in this simple example we do not know how to measure the value of k_0^{FSI}. We only have cuts which are roughly proportional to a range of FSI momentum exchange with an unknown proportionality constant.

A.3.3 Concluding Remarks

The FSI problem cannot escape model dependence. The strategy outlined above uses the over-determined kinematics to get a handle on FSIs. A PWIA analysis permits a kinematic

[1]This is somewhat analogous to using a bremsstrahlung photon beam at different energies in photo-production experiments. Taking the cross-section difference at slightly different beam energies allows the contribution from the high-energy tip of the bremsstrahlung spectrum to be isolated.

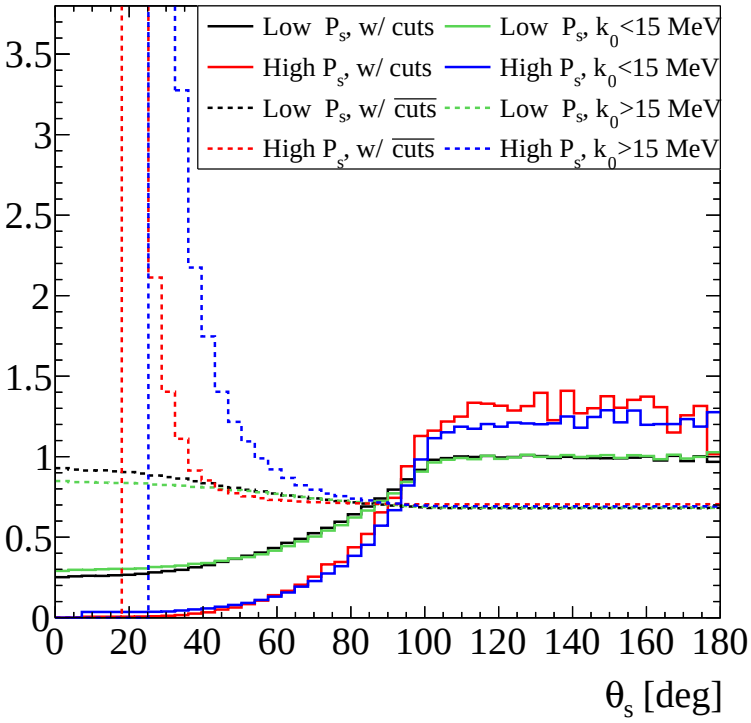

Figure A.10: Ratios (A.56) for the small (solid) and large (dashed) FSI momentum exchange. The plots labeled with $\overline{\text{cuts}}$ indicate the events are selected with the inverse of the cut discussed above, which in this case will select events with significant FSIs.

separation *at the event level* yielding roughly two event types: i) events with FSI causing significant deviation from PWIA kinematics, and ii) events with FSI that produce no discernible difference when compared to the PWIA result.

The first type of event can be removed if the goal is finding maximally FSI-free events, however, these events are invaluable for studying various models of FSIs. The over-determined kinematics will give an extra handle to test various models. Using models in agreement with type (i) events, the events of type (ii) can be systematically corrected (or even justified to be negligible). More theoretical input is needed for accurately modeling but this does not affect the impact of this proposals' result.

Perhaps the ultimate extension of the experimental setup would be to measure the induced polarization of the struck nucleon. This would be a DVCS version of the quasi-elastic scattering experiments where P_y gives a measure of FSIs. This too would have a model dependence but the combination would be quite powerful in understanding the FSIs[2].

[2]However, this method would require a new large recoil polarimeter which does not seem feasible at the moment.

Appendix B

DVCS Formalism

B.1 Theory bound nucleon DVCS

In the infinite-momentum frame, where the initial and the final nucleons go at the speed of light along the positive z-axis, the partons have relatively small transverse momenta compared to their longitudinal momenta. Referring to figure B.1, the struck parton carries a longitudinal momentum fraction $x+\xi$ and it goes back into the nucleon with a momentum fraction $x-\xi$. The GPDs are defined in the interval where x and $\xi \in$ [-1,1], which can be separated into three regions as can be seen in figure B.1. The regions are:

- $x \in [\xi,1]$: both momentum fractions $x+\xi$ and $x-\xi$ are positive and the process describes the emission and reabsorption of a quark.
- $x \in [-\xi,\xi]$: $x+\xi$ is positive reflecting the emission of a quark, while $x-\xi$ is negative and is interpreted as an antiquark being emitted from the initial proton.
- $x \in [-1,-\xi]$: both fractions are negative, and $x+\xi$ and $x-\xi$ represent the emission and reabsorption of antiquarks.

The GPDs in the first and in the third regions represent the probability amplitude of finding a quark or an antiquark in the nucleon, while in the second region they represent the probability amplitude of finding a quark-antiquark pair in the nucleon [57].

Following the definition of reference [58], the differential DVCS cross section is obtained

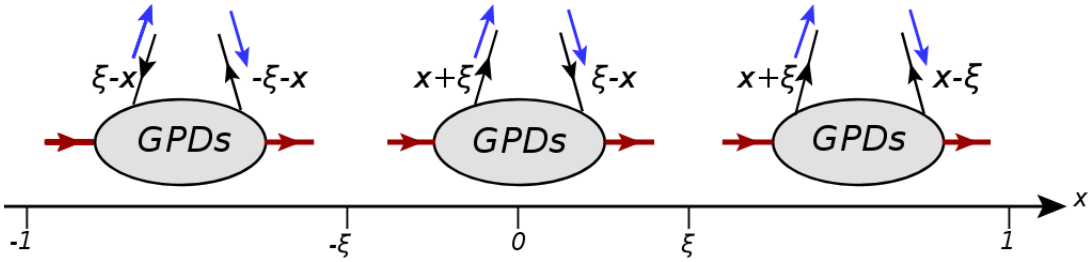

Figure B.1: The parton interpretations of the GPDs in three x-intervals [-1,-ξ], [-ξ,ξ] and [ξ,1]. The red arrows indicate the initial and the final-state of the proton, while the blue (black) arrows represent helicity (momentum) of the struck quark.

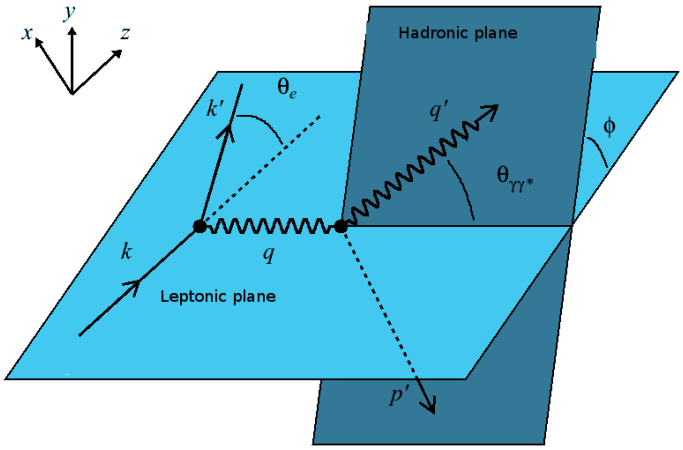

Figure B.2: The definition of the azimuthal angle ϕ between the leptonic and the hadronic planes.

from the DVCS scattering amplitude ($\mathcal{T}_{DVCS}$) as:

$$\frac{d^5\sigma}{dQ^2\,dx_B\,dt\,d\phi\,d\phi_e} = \frac{1}{(2\pi^4)32}\frac{x_B\,y^2}{Q^4}\left(1+\frac{4M^2x_B^2}{Q^2}\right)^{-1/2}|\mathcal{T}_{DVCS}|^2, \tag{B.1}$$

where ϕ_e is the azimuthal angle of the scattered lepton, $y = \frac{E-E'}{E}$ and Q^2, x_B, t, ϕ are the four kinematic variables that describe the process. The variable ϕ is the angle between the leptonic and the hadronic planes, as can be seen in figure B.2.

By neglecting the mass of the quark with respect to the energies of γ^* and γ, the DVCS scattering amplitude can be parametrized by four quark helicity conserving (chiral-even)

GPDs: H, E, $\widetilde{H}$ and $\widetilde{E}$ as:

$$\mathcal{T}_{DVCS} = \sum_q (|e|Q_q)^2 \varepsilon_\mu^* \varepsilon_\nu \Bigg\{ g_\perp^{\mu\nu} \int_{-1}^{1} dx \left[\frac{1}{x-\xi+i\varepsilon} + \frac{1}{x+\xi-i\varepsilon} \right] \times \frac{1}{2} \bar{u}(p') \left[H^q \gamma^+ + E^q i\sigma^{+\alpha} \frac{\Delta_\alpha}{2m_N} \right] u(p) + i\varepsilon^{\mu\nu+-} \int_{-1}^{1} dx \left[\frac{1}{x+\xi-i\varepsilon} - \frac{1}{x-\xi+i\varepsilon} \right] \times \frac{1}{2} \bar{u}(p') \left[\tilde{H}^q \gamma^+ \gamma_5 + \tilde{E}^q \gamma_5 \frac{\Delta^+}{2m_N} \right] u(p) \Bigg\}, \tag{B.2}$$

where $\bar{u}(p')$ and $u(p)$ are the spinors of the nucleon.

The GPDs H, E, $\widetilde{H}$ and $\widetilde{E}$ are defined for each quark flavor (q = u, d, s, ...). Analogous GPDs exist for the gluons, see references [58, 59, 60] for details. In this work, we are mostly concerned by the valence quark region, in which the sea quarks and the gluons contributions do not dominate the DVCS scattering amplitude.

The GPDs H, E, $\widetilde{H}$ and $\widetilde{E}$ are called chiral-even GPDs because they conserve the helicity of the struck quark. The GPDs H and $\widetilde{H}$ conserve the spin of the nucleon, while E and $\widetilde{E}$ flip it. The H and E GPDs are called the unpolarized GPDs as they represent the sum over the different configurations of the quarks' helicities, whereas $\widetilde{H}$ and $\widetilde{E}$ are called the polarized GPDs because they are made up of the difference between the orientations of the quarks' helicities.

If one keeps the quark mass, another set of GPDs gives contribution to the DVCS amplitude. They are called chiral-odd GPDs. They give information about the quarks helicity-flip transitions. At leading twist, there are four chiral-odd GPDs that parametrize the helicity-flip structure of the partons in a nucleon: H_T, E_T, $\widetilde{H}_T$ and $\widetilde{E}_T$ [61]. Analogous set of chiral-odd GPDs exist for the gluon sector (see [61, 62]). The chiral-even GPDs contribute mostly in the regions where $\xi < x$ and $x < -\xi$, while the chiral-odd GPDs have larger contribution in the $x < |\xi|$ region [58].

B.1.0.1 Basic properties of GPDs

Links to the ordinary FFs and PDFs Links between GPDs and the FFs are constructed by integrating the GPDs over the momentum fraction x at given momentum transfer (t). Because of Lorentz invariance, integrating over x removes all the references to the particular light-cone frame, in which ξ is defined. Therefore, the result must be ξ-independent as can

be see in equation B.3:

$$\begin{aligned} \int_{-1}^{1} dx\, H^q(x,\xi,t) &= F_1^q(t), \qquad \int_{-1}^{1} dx\, E^q(x,\xi,t) = F_2^q(t), \\ \int_{-1}^{1} dx\, \widetilde{H}^q(x,\xi,t) &= G_A^q(t), \qquad \int_{-1}^{1} dx\, \widetilde{E}^q(x,\xi,t) = G_P^q(t), \end{aligned} \tag{B.3}$$

where $F_1^q(t)$ and $F_2^q(t)$ are the previously introduced Dirac and Pauli FFs, $G_A^q(t)$ and $G_P^q(t)$ are the axial and pseudoscalar electroweak FFs. The latter two can be measured in electroweak interactions; see reference [63] for more details about the electroweak FFs.

From the optical theorem, the DIS cross section is proportional to the imaginary part of the forward amplitude of the doubly virtual Compton scattering (production of a spacelike ($Q^2 < 0$) virtual photon in the final state instead of a real photon) [37]. In the limit $\xi \to 0$ and t $\to 0$, the GPDs are reduced to the ordinary PDFs, such that for the quark sector:

$$H^q(x,0,0) = q(x), \qquad \widetilde{H}^q(x,0,0) = \Delta q(x), \tag{B.4}$$

where $q(x)$ is the unpolarized PDF, defined for each quark flavor. The polarized PDFs $\Delta q(x)$ are accessible from polarized-beam and polarized-target DIS experiments. There are no similar relations for the GPDs E and $\widetilde{E}$, as in the scattering amplitude, equation B.2, they are multiplied by factors proportional to t ($= \Delta^2$), which vanish in the forward limit. Figure B.3 summarizes the physics interpretations of the GPDs, the FFs, the PDFs, and the links between them.

Polynomiality of GPDs The GPDs have a key property which is the polynomiality. This property comes from the Lorentz invariance of the nucleon matrix elements. It states that the x^n moment of the GPDs must be a polynomial in ξ with a maximum order of n+1 [58].

$$\int_{-1}^{1} dx\, x^n H^q(x,\xi,t) = \sum_{(even)i=0}^{n} (2\xi)^i A_{n+1,i}^q(t) + mod(n,2)(2\xi)^{n+1} C_{n+1}^q(t), \tag{B.5}$$

$$\int_{-1}^{1} dx\, x^n E^q(x,\xi,t) = \sum_{(even)i=0}^{n} (2\xi)^i B_{n+1,i}^q(t) - mod(n,2)(2\xi)^{n+1} C_{n+1}^q(t), \tag{B.6}$$

$$\int_{-1}^{1} dx\, x^n \widetilde{H}^q(x,\xi,t) = \sum_{(even)i=0}^{n} (2\xi)^i \widetilde{A}_{n+1,i}^q(t), \tag{B.7}$$

$$\int_{-1}^{1} dx\, x^n \widetilde{E}^q(x,\xi,t) = \sum_{(even)i=0}^{n} (2\xi)^i \widetilde{B}_{n+1,i}^q(t). \tag{B.8}$$

where $mod(n,2)$ is 1 for odd n and 0 for even n. Thus, the corresponding polynomials contain only even powers of the skewedness parameter ξ. This follows from time-reversal invariance,

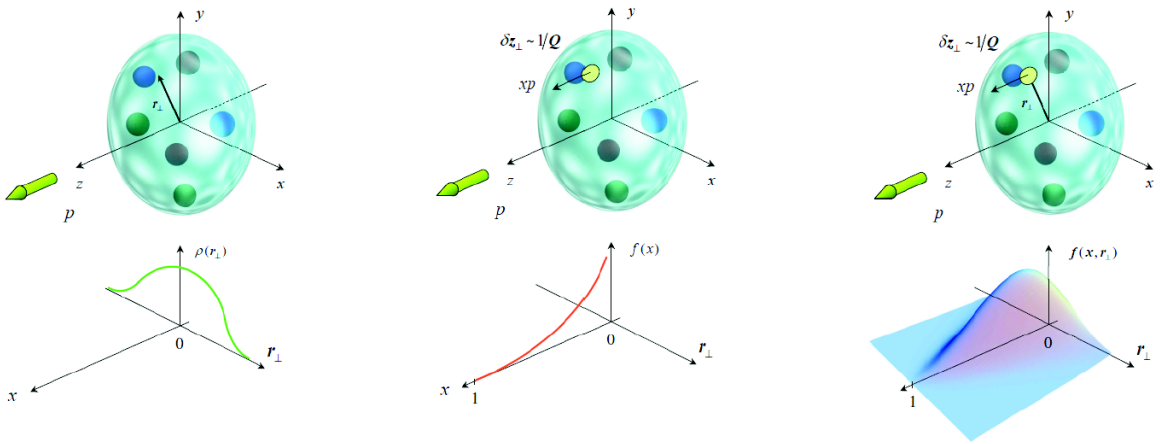

Figure B.3: The links between the GPDs and the ordinary FFs and PDFs. From left to right: the FFs reflect, via a Fourier transform, the two-dimensional spatial distributions of the quarks in the transverse plane; the PDFs give information about the longitudinal momentum distributions of the partons; finally, the GPDs provide a three-dimensional imaging of the partons in terms of both their longitudinal momenta and their position in the transverse space plane. The figure is from [64].

i.e. $GPD(x,\xi,t) = GPD(x,-\xi,t)$ [65]. This implies that the highest power of ξ is $n+1$ for odd n (singlet GPDs) and of highest power n in case of even n (non-singlet GPDs). Due to the fact that the nucleon has spin 1/2, the coefficients in front of the highest power of ξ for the singlet functions H^q and E^q are equal and have opposite signs. This sum rule is the same for the gluons [62].

As a consequence of the polynomiality of the GPDs, the first moments of GPDs lead to the ordinary form factors, as shown previously in this section. X. Ji derived a sum rule [66] that links the second moments of the quark GPDs H^q and E^q, in the forward limit ($t=0$), to the total angular momentum ($J_{quarks} = \frac{1}{2}\Delta\Sigma + L_{quarks}$), where $\Delta\Sigma$ is the contribution of the quark spin to the nucleon spin and L_{quarks} is the quarks orbital angular momentum contribution, as:

$$J_{quarks} = \frac{1}{2}\int_{-1}^{1} dx\; x\,[H^q(x,\xi,t=0) + E^q(x,\xi,t=0)] \tag{B.9}$$

A similar expression exists for the gluons contribution (J_{gluons}).

The spin of a nucleon is built from the sum of the quarks' and the gluons' total angular momenta, $\frac{1}{2} = J_{quarks} + J_{gluons}$. Regarding the experimental measurements, the EMC collaboration [67] has measured the contribution of the spins of the quarks ($\Delta\Sigma$) to the nucleon spin to be around 30%. Therefore, measuring the second moments of the GPDs H and E

will give access to the quarks orbital momentum (L_{quarks}) which will complete the sector of the quarks in understanding the nucleon spin. For the gluon total angular momentum (J_{gluons}), it is still an open question how to decompose J_{gluons} into orbital (L_{gluons}) and spin (Δg) components and to access them experimentally, see reference [68] for more discussions on this subject.

B.1.0.2 Compton form factors

The GPDs are real functions of two experimentally measurable variables, ξ and t, and one unmeasurable variable, x, in the DVCS reaction. Therefore, the GPDs are not directly measurable. In DVCS what we measure are the Compton Form Factors (CFFs) that are linked to the GPDs. As shown in equation B.2, the DVCS scattering amplitude, at leading order in α_s and leading twist, contains x-integrals of the form, $\int_{-1}^{+1} dx \frac{GPD^q(x,\xi,t)}{x\pm\xi\mp i\varepsilon}$, where $\frac{1}{x\pm\xi+i\varepsilon}$ is the propagator of the quark between the two photons. The integrals can be written as:

$$\int_{-1}^{+1} dx \frac{GPD^q(x,\xi,t)}{x\pm\xi\mp i\varepsilon} = \mathcal{P}\int_{-1}^{1} dx \frac{GPD^q(x,\xi,t)}{x\pm\xi} \pm i\pi GPD^q(x=\mp\xi,\xi,t), \tag{B.10}$$

where $\mathcal{P}$ stands for the Cauchy principal value integral. The DVCS amplitude can be decomposed into four complex CFFs, such that for each GPD there is a corresponding CFF. For instance, for the GPD $H^q(x,\xi,t)$, the real and imaginary parts of its CFF ($\mathcal{H}(\xi,t)$) at leading order in α_s can be expressed as:

$$\mathcal{H}(\xi,t) = \Re e(\mathcal{H})(\xi,t) - i\pi \Im m(\mathcal{H})(\xi,t) \tag{B.11a}$$

$$\text{with} \qquad \Re e(\mathcal{H})(\xi,t) = \mathcal{P}\int_0^1 dx [H(x,\xi,t) - H(-x,\xi,t)]\, C^+(x,\xi) \tag{B.11b}$$

$$\text{and} \qquad \Im m(\mathcal{H})(\xi,t) = H(\xi,\xi,t) - H(-\xi,\xi,t), \tag{B.11c}$$

where the term corresponding to the real part is weighted by $C^+(x,\xi)$ ($= \frac{1}{x-\xi} + \frac{1}{x+\xi}$), which appears also in an analogous expression for the GPD $E^q(x,\xi,t)$. The real parts of the CFFs that are associated with the GPDs $\widetilde{H}^q(x,\xi,t)$ and $\widetilde{E}^q(x,\xi,t)$, are weighted by $C^-(x,\xi)$ ($= \frac{1}{x-\xi} - \frac{1}{x+\xi}$).

B.1.0.3 Bethe-Heitler

Experimentally, the DVCS is indistinguishable from the Bethe-Heitler (BH) process, which is the reaction where the final photon is emitted either from the incoming or the outgoing leptons, as shown in figure B.4. The BH process is not sensitive to GPDs and does not carry information about the partonic structure of the hadronic target. The BH cross

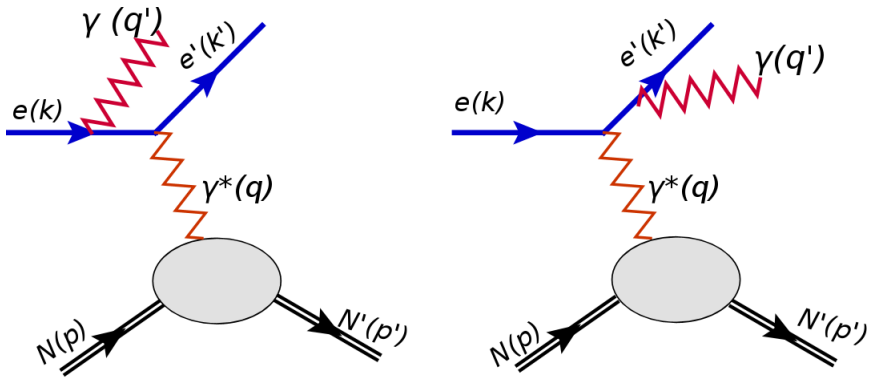

Figure B.4: Schematic for the Bethe-Heitler process. The final real photon can be emitted from the incoming electron (left plot) or from the scattered electron (right plot).

section is calculable from the well-known electromagnetic FFs.

The $ep \to ep\gamma$ differential cross section of a longitudinally-polarized electron beam on an unpolarized proton target can be written as [69]:

$$\frac{d^5\sigma^\lambda}{dQ^2 dx_B dt d\phi d\phi_e} = \frac{\alpha^3}{16\pi^2} \frac{x_B\, y^2}{Q^2\sqrt{1+(2x_b M_N/Q)^2}} \frac{|\mathcal{T}_{BH}|^2 + |\mathcal{T}^\lambda_{DVCS}|^2 + \mathcal{I}^\lambda_{BH*DVCS}}{e^6} \tag{B.12}$$

where λ is the beam helicity, $\mathcal{T}_{DVCS}$ is the pure DVCS scattering amplitude, $\mathcal{T}_{BH}$ is the pure BH amplitude and $\mathcal{I}^\lambda_{BH*DVCS}$ represents the interference amplitude. At leading twist, A. V. Belitsky, D. Mueller and A. Kirchner have shown that these amplitudes can be decomposed into a finite sum of Fourier harmonics, the so-called BMK formalism [69], as:

$$|\mathcal{T}_{BH}|^2 = \frac{e^6(1+\varepsilon^2)^{-2}}{x_B^2 y^2 t \mathcal{P}_1(\phi)\mathcal{P}_2(\phi)} \left[c_0^{BH} + \sum_{n=1}^{2} \left(c_n^{BH}\cos(n\phi) + s_n^{BH}\sin(\phi) \right) \right] \tag{B.13}$$

$$|\mathcal{T}_{DVCS}|^2 = \frac{e^6}{y^2 Q^2} \left[c_0^{DVCS} + \sum_{n=1}^{2} \left(c_n^{DVCS}\cos(n\phi) + \lambda s_n^{DVCS}\sin(n\phi) \right) \right] \tag{B.14}$$

$$\mathcal{I}_{BH*DVCS} = \frac{\pm e^6}{x_B y^3 t\, \mathcal{P}_1(\phi)\mathcal{P}_2(\phi)} \left[c_0^{I} + \sum_{n=0}^{3} \left(c_n^{I}\cos(n\phi) + \lambda s_n^{I}\sin(n\phi) \right) \right] \tag{B.15}$$

where $\mathcal{P}_1(\phi)$ and $\mathcal{P}_2(\phi)$ are the BH propagators. The leading twist expressions of the DVCS, BH and interference Fourier coefficients on a proton target can be found in reference [69].

The $+(-)$ sign in the interference term stands for the negatively (positively) charged lepton beam. In the case of an unpolarized proton target, the coefficients of the $\sin(\phi)$ in the BH amplitude are zeros.

Appendix C

Detailed Experimental Projections

C.1 Kinematic Coverage

Here we present many kinematic plots for the tagged DVCS reactions.

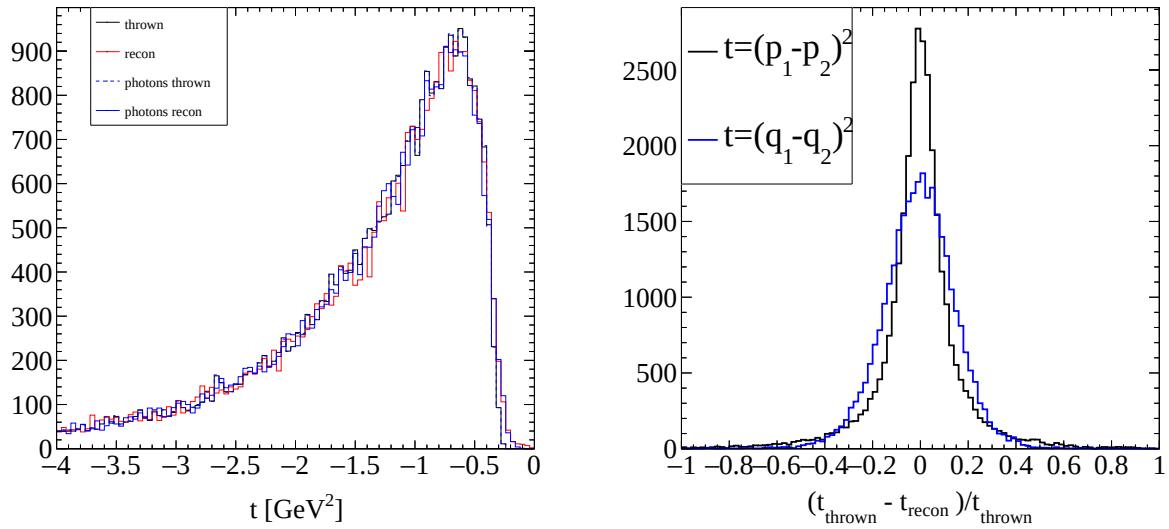

Figure C.1: Left: Thrown and reconstructed t calculated from the photons (t_q) and hadrons (t_p). Right: The corresponding resolutions for the two methods of determining t.

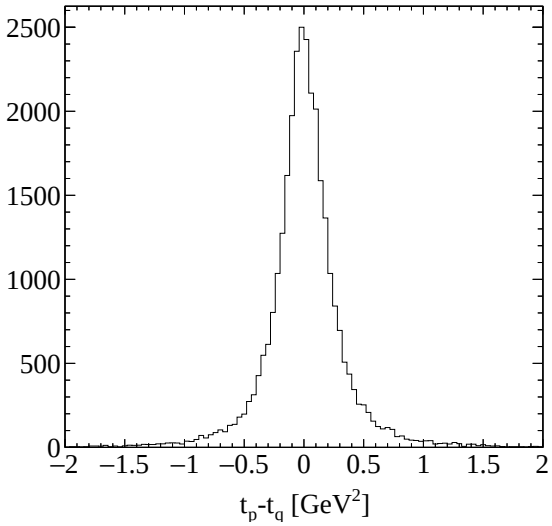

Figure C.2: The difference in the momentum transfers, $\delta t = t_p - t_q$.

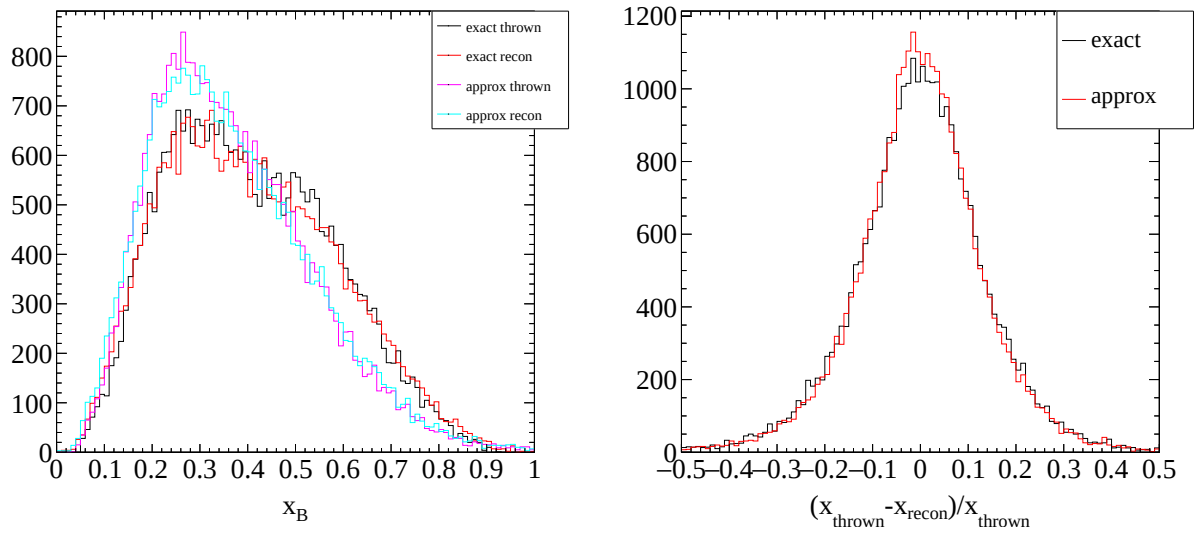

Figure C.3: Left: Thrown and reconstructed x_B where the approximate calculation assumes the struck nucleon is at rest, i.e., $x_{approx} = Q^2/2M\nu$. Right: Relative resolutions expected.

C.2 Projections for $\sin\phi$ harmonic of the BSA

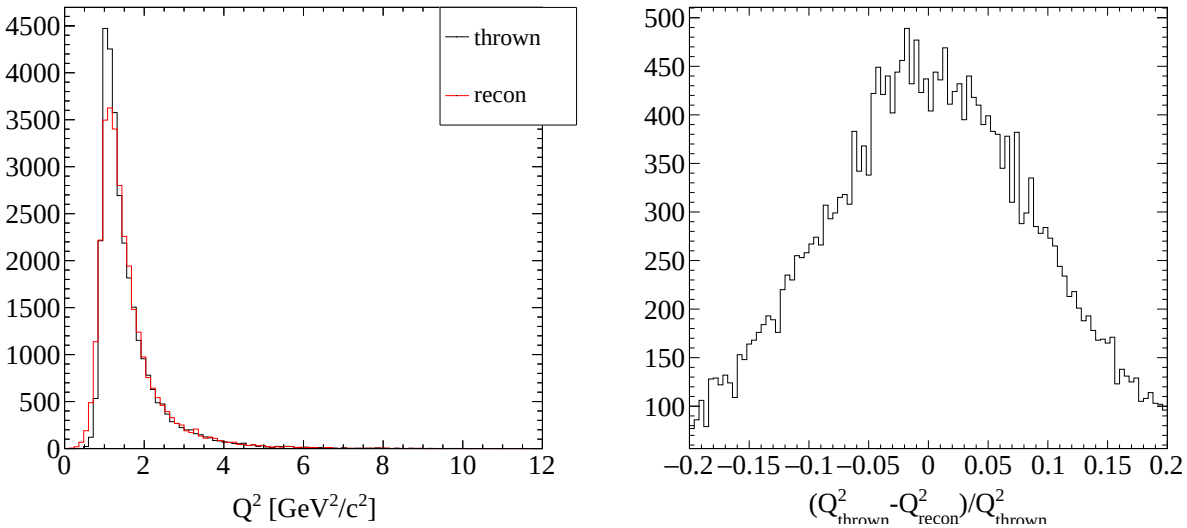

Figure C.4: Reconstructed Q^2 and its simulated resolution.

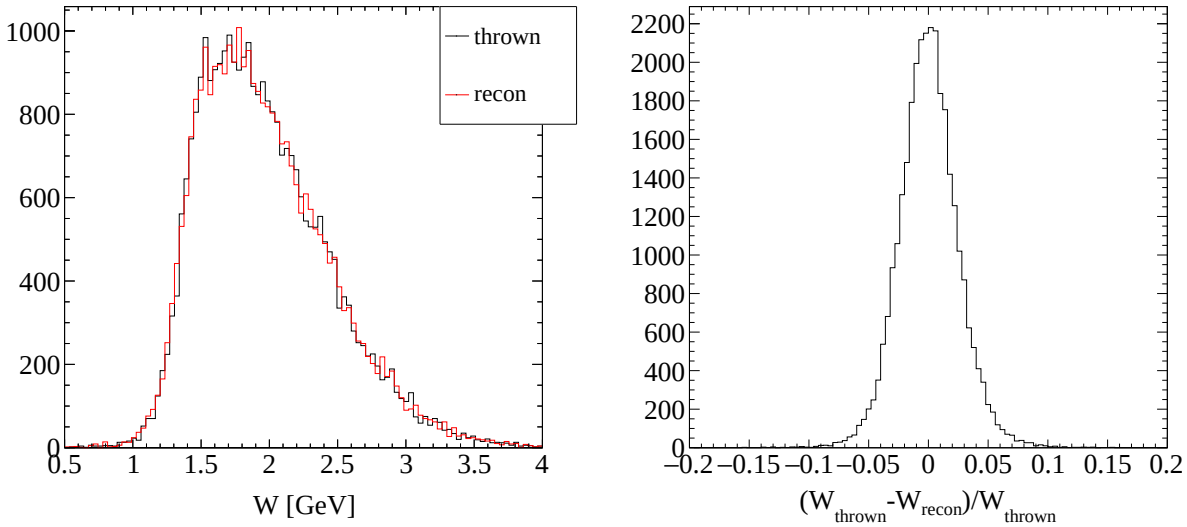

Figure C.5: Reconstructed W and its simulated resolution.

C.2.1 Off-forward EMC Effect Ratio

The projected statistical uncertainties for the off-forward EMC ratio, defined in Equation 4.2, is shown in Figure C.10.

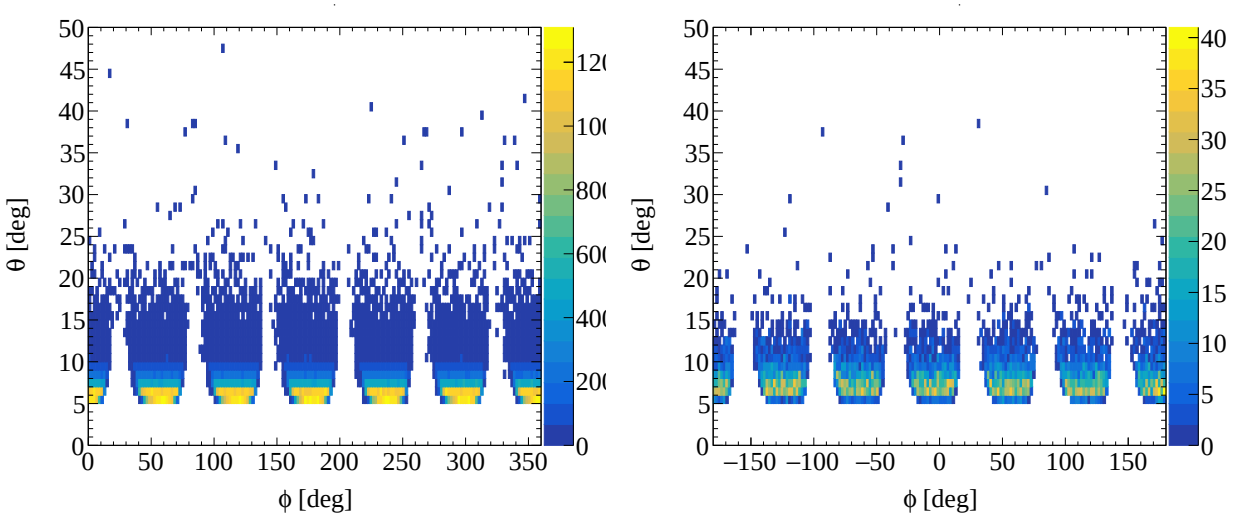

Figure C.6: Electron θ Vs. ϕ, before (left) and after (right) cuts.

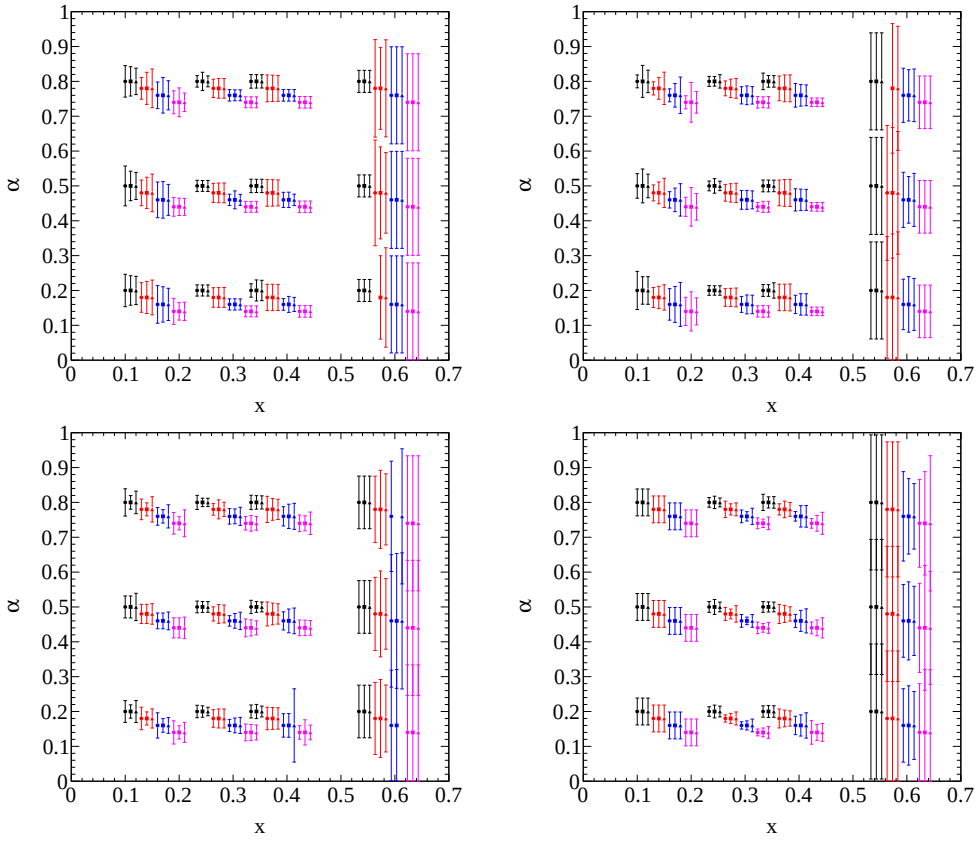

Figure C.7: Projected statistical uncertainty for the n-DVCS α from a ^{4}He target. The points are offset for clarity. Each plot shows the results for different Q^2 bins starting with the lowest in the upper left and the highest in the lower right. The horizontal bands of points starting from low to high are for the three spectator momentum bins (like Figure 4.12) and the different symbols indicate the spectator angle bins. The points color along with points grouped with a slight negative slope are for different t bins starting with black for the lows $|t|$ bin.

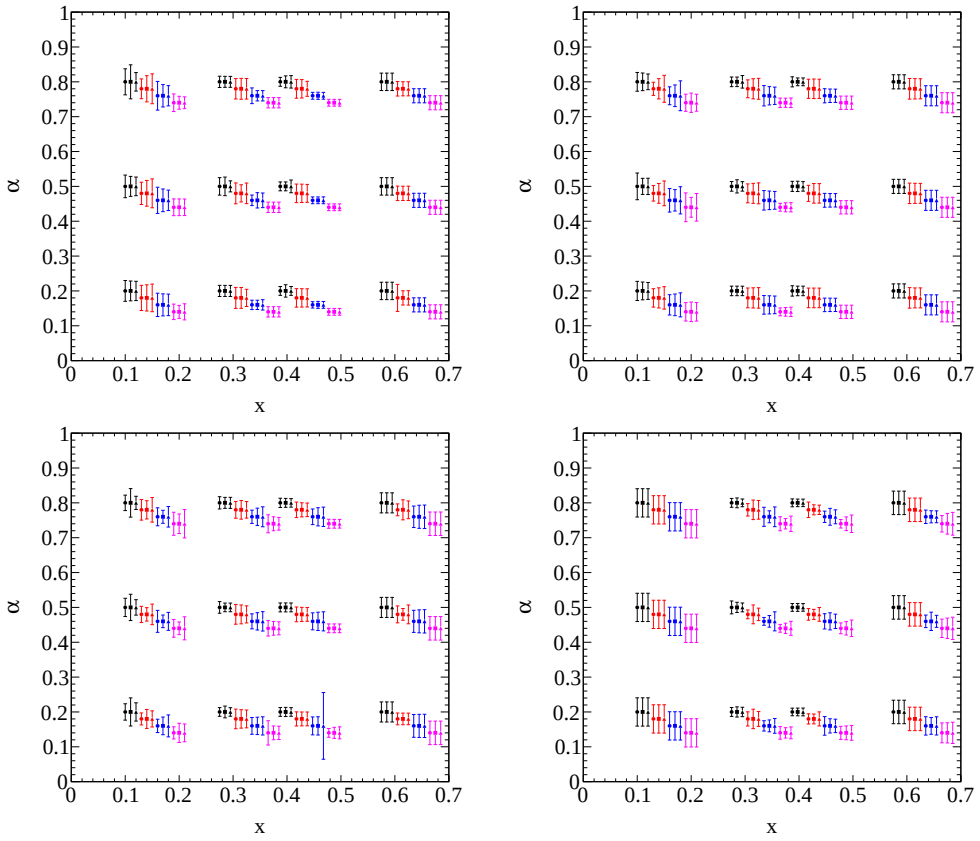

Figure C.8: Same as Figure C.7 except for p-DVCS on a ^{4}He target.

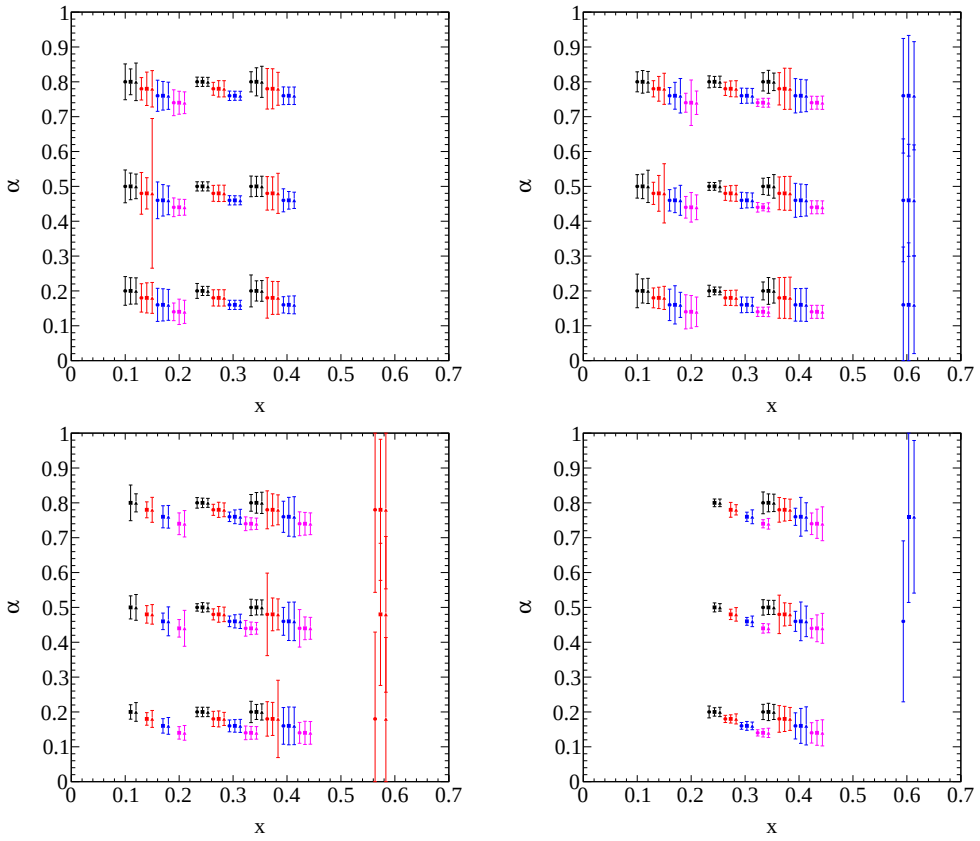

Figure C.9: Same as Figure C.7 except for n-DVCS on a ^{2}H target.

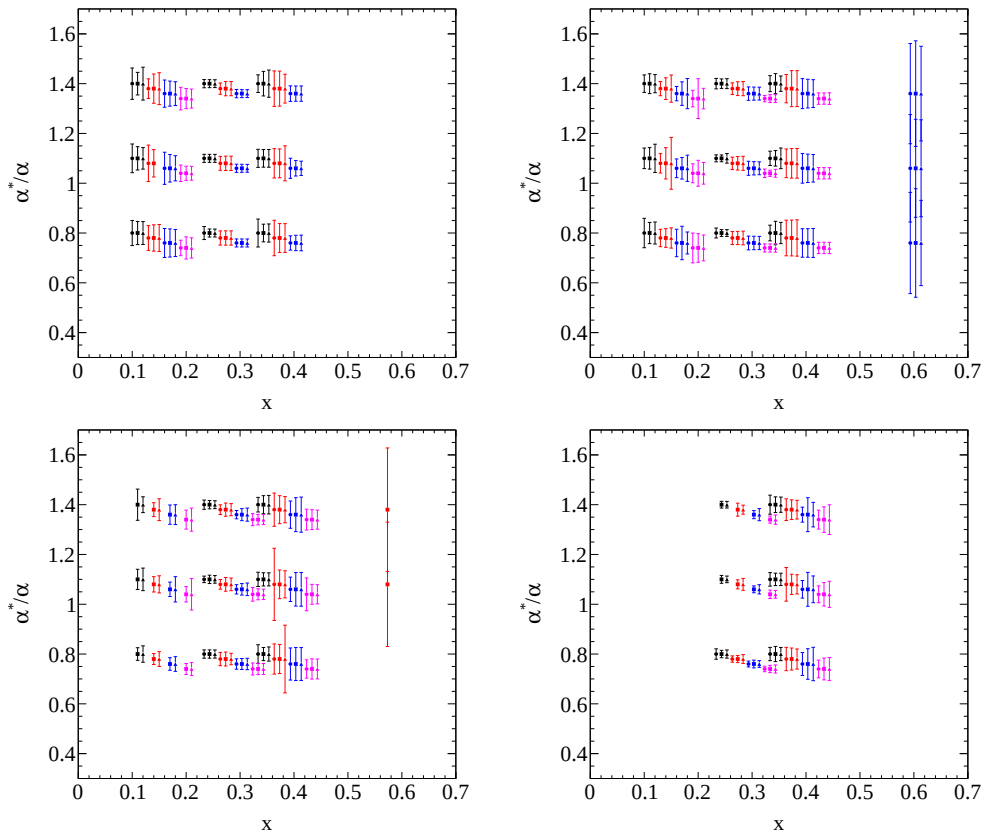

Figure C.10: The off-forward EMC ratio for a bound neutron to a quasi-free neutron (see Equation 4.2) for the same kinematics and binning described in Figure C.9

Bibliography

[1] S. Chekanov *et al.*, "Measurement of deeply virtual Compton scattering at HERA," *Phys. Lett.*, vol. B573, pp. 46–62, 2003.

[2] A. Aktas *et al.*, "Measurement of deeply virtual compton scattering at HERA," *Eur. Phys. J.*, vol. C44, pp. 1–11, 2005.

[3] C. M. Camacho *et al.*, "Scaling tests of the cross-section for deeply virtual compton scattering," *Phys. Rev. Lett.*, vol. 97, p. 262002, 2006.

[4] F. X. Girod *et al.*, "Measurement of Deeply virtual Compton scattering beam-spin asymmetries," *Phys. Rev. Lett.*, vol. 100, p. 162002, 2008.

[5] M. Mazouz *et al.*, "Deeply virtual compton scattering off the neutron," *Phys. Rev. Lett.*, vol. 99, p. 242501, 2007.

[6] M. M. Rvachev *et al.*, "The Quasielastic He-3(e,e'p)d reaction at Q**2 = 1.5-GeV**2 for recoil momenta up to 1-GeV/c," *Phys. Rev. Lett.*, vol. 94, p. 192302, 2005.

[7] M. Paolone *et al.*, "Polarization Transfer in the 4He(e,e'p)3H Reaction at $Q^2 = 0.8$ and 1.3 $(\mathrm{GeV/c})^2$," *Phys. Rev. Lett.*, vol. 105, p. 072001, 2010.

[8] S. P. Malace *et al.*, "A precise extraction of the induced polarization in the 4He(e,e'p)3H reaction," *Phys. Rev. Lett.*, vol. 106, p. 052501, 2011.

[9] S. F. *et al.*, "Deeply Virtual Compton Scattering with CLAS at 11 GeV," *A proposal to PAC 30*, 2006.

[10] C. Hyde *et al.*, "Measurements of Electron-Helicity Dependent Cross Sections of Deeply Virtual Compton Scattering with CEBAF at 12 GeV," *A proposal to PAC 38*, 2011.

[11] J. J. Aubert *et al.*, "The ratio of the nucleon structure functions $F2_n$ for iron and deuterium," *Phys. Lett.*, vol. B123, pp. 275–278, 1983.

[12] L. Weinstein *et al.*, "Short Range Correlations and the EMC Effect," *Phys.Rev.Lett.*, vol. 106, p. 052301, 2011.

[13] Z. E. Meziani *et al.*, "Coulomb Sum Rule for Ca-40, Ca-48, and Fe-56 for $|\vec{q}| \leqslant$ 550-MeV/c," *Phys. Rev. Lett.*, vol. 52, pp. 2130–2133, 1984.

[14] J. Morgenstern and Z. E. Meziani, "Is the Coulomb sum rule violated in nuclei?," *Phys. Lett.*, vol. B515, pp. 269–275, 2001.

[15] Cloët, Ian C. and Bentz, Wolfgang and Thomas, Anthony W., "Relativistic and Nuclear Medium Effects on the Coulomb Sum Rule," *Phys. Rev. Lett.*, vol. 116, no. 3, p. 032701, 2016.

[16] C. Ciofi degli Atti and B. Z. Kopeliovich, "Final state interaction in semiinclusive DIS off nuclei," *Eur. Phys. J.*, vol. A17, pp. 133–144, 2003.

[17] X.-D. Ji, "Gauge-Invariant Decomposition of Nucleon Spin," *Phys. Rev. Lett.*, vol. 78, pp. 610–613, 1997.

[18] H. Fenker *et al.*, "BoNus: Development and use of a radial TPC using cylindrical GEMs," *Nucl. Instrum. Meth.*, vol. A592, pp. 273–286, 2008.

[19] M. Amaryan *et al.*, "The Structure of the Free Neutron at Large x-Bjorken (PR12-06-113)," *A proposal to PAC 30*, 2006.

[20] I. C. Cloet, W. Bentz, and A. W. Thomas, "Spin-dependent structure functions in nuclear matter and the polarized EMC effect," *Phys. Rev. Lett.*, vol. 95, p. 052302, 2005.

[21] M. Burkardt, "Impact parameter space interpretation for generalized parton distributions," *Int. J. Mod. Phys.*, vol. A18, pp. 173–208, 2003.

[22] V. Guzey, A. W. Thomas, and K. Tsushima, "Medium modifications of the bound nucleon GPDs and incoherent DVCS on nuclear targets," *Phys. Lett.*, vol. B673, pp. 9–14, 2009.

[23] S. Liuti and S. K. Taneja, "Nuclear medium modifications of hadrons from generalized parton distributions," *Phys. Rev.*, vol. C72, p. 034902, 2005.

[24] S. Liuti, "Connection between in medium nucleon form-factors and deep inelastic structure functions," 2006.

[25] R. Dupre and S. Scopetta, "3D Structure and Nuclear Targets," 2015.

[26] C. Ciofi degli Atti, "In-medium short-range dynamics of nucleons: Recent theoretical and experimental advances," *Phys. Rept.*, vol. 590, pp. 1–85, 2015.

[27] S. Jeschonnek and J. W. Van Orden, "A New calculation for D(e, e-prime p)n at GeV energies," *Phys. Rev.*, vol. C78, p. 014007, 2008.

[28] C. Ciofi degli Atti, L. P. Kaptari, and B. Z. Kopeliovich, "Final state interaction effects in semiinclusive DIS off the deuteron," *Eur. Phys. J.*, vol. A19, pp. 145–151, 2004.

[29] V. Guzey and M. Strikman, "DVCS on spinless nuclear targets in impulse approximation," *Phys. Rev.*, vol. C68, p. 015204, 2003.

[30] F. Cano and B. Pire, "Deep electroproduction of photons and mesons on the deuteron," *Eur. Phys. J.*, vol. A19, pp. 423–438, 2004.

[31] A. Kirchner and D. Mueller, "Deeply virtual Compton scattering off nuclei," *Eur. Phys. J.*, vol. C32, pp. 347–375, 2003.

[32] V. M. Braun, A. N. Manashov, D. Mueller, and B. Pirnay, "Resolving kinematic ambiguities in QCD predictions for Deeply Virtual Compton Scattering," *PoS*, vol. DIS2014, p. 225, 2014.

[33] A. V. Belitsky, D. Mueller, and A. Kirchner, "Theory of deeply virtual Compton scattering on the nucleon," *Nucl. Phys.*, vol. B629, pp. 323–392, 2002.

[34] A. V. Belitsky and D. Mueller, "Exclusive electroproduction revisited: treating kinematical effects," *Phys. Rev.*, vol. D82, p. 074010, 2010.

[35] Belitsky, Andrei V. and Müller, Dieter and Ji, Yao, "Compton scattering: from deeply virtual to quasi-real," *Nucl. Phys.*, vol. B878, pp. 214–268, 2014.

[36] A. V. Belitsky, D. Mueller, L. Niedermeier, and A. Schafer, "Leading twist asymmetries in deeply virtual Compton scattering," *Nucl. Phys.*, vol. B593, pp. 289–310, 2001.

[37] M. Guidal, H. Moutarde, and M. Vanderhaeghen, "Generalized Parton Distributions in the valence region from Deeply Virtual Compton Scattering," *Rept. Prog. Phys.*, vol. 76, p. 066202, 2013.

[38] M. Hattawy *et al.* (EG6 Working Group), "Deeply Virtual Compton Scattering off ^{4}He," *CLAS internal analysis note*, 2016.

[39] S. Liuti and S. K. Taneja, "Microscopic description of deeply virtual Compton scattering off spin-0 nuclei," *Phys. Rev.*, vol. C72, p. 032201, 2005.

[40] R. B. Wiringa, R. Schiavilla, S. C. Pieper, and J. Carlson, "Nucleon and nucleon-pair momentum distributions in $A \leq 12$ nuclei," *Phys. Rev.*, vol. C89, no. 2, p. 024305, 2014.

[41] "CLAS12 Technical Design Report," 2008.

[42] J. Peyré, B. Genolini, and J. Poutas, "A Full-Scale Prototype for the Tracking Chambers of the ALICE Muon Spectrometer," 1998.

[43] T. Abe *et al.*, "Belle II Technical Design Report," 2010.

[44] E. Etzion *et al.*, "The Certification of ATLAS Thin Gap Chambers Produced in Israel and China," 2004.

[45] S. Biagi, "Monte Carlo simulation of electron drift and diffusion in counting gases under the influence of electric and magnetic fields," *Nucl.Instrum.Meth.*, vol. A421, pp. 234–240, 1999.

[46] C. Ciofi degli Atti *et al.*, "The readout system for the clas12 micromegas vertex tracker," in *2014 19th IEEE-NPSS Real Time Conference*, pp. 1–11, May 2014.

[47] T. C. Collaboration, "Clas12 forward tagger (ft) technical design report." https://www.jlab.org/Hall-B/clas12-web/docs/ft-tdr.2.0.pdf, 2012. Online; accessed 29 January 2016.

[48] "Petiroc-2a." http://www.weeroc.com/en/products/petiroc-2. Accessed: 2017-05-15.

[49] C. Zorn, "A pedestrian's guide to radiation damage in plastic scintillators," *Nucl. Phys. Proc. Suppl.*, vol. 32, pp. 377–383, 1993.

[50] Y. Qiang, C. Zorn, F. Barbosa, and E. Smith, "Radiation Hardness Tests of SiPMs for the JLab Hall D Barrel Calorimeter," *Nucl. Instrum. Meth.*, vol. A698, pp. 234–241, 2013.

[51] Y. Qiang, C. Zorn, F. Barbosa, and E. Smith, "Neutron radiation hardness tests of SiPMs," *AIP Conf. Proc.*, vol. 1560, pp. 703–705, 2013.

[52] S. Ahmad. Private communication, May 2017. Weeroc SAS.

[53] K. Emi *et al.*, "Study of a dE/ dx measurement and the gas-gain saturation by a prototype drift chamber for the BELLE-CDC," *Nucl. Instrum. Meth.*, vol. A379, pp. 225–231, 1996.

[54] S. Stepanyan and A. P. Freyberger. Private communication, May 2017.

[55] S. Niccolai *et al.*, "Deeply Virtual Compton Scattering on the Neutron with CLAS12 at 11 GeV," *A proposal to PAC 38*, 2011.

[56] L. Weinstein, C. T. Whelan, N. J. Mason, *et al.*, "Electron Scattering: From Atoms, Molecules, Nuclei, and Bulk Matter," pp. 300–311, 2005.

[57] M. Diehl, "Generalized parton distributions with helicity flip," *Eur. Phys. J.*, vol. C19, pp. 485–492, 2001.

[58] X.-D. Ji, "Off forward parton distributions," *J. Phys.*, vol. G24, pp. 1181–1205, 1998.

[59] A. V. Radyushkin, "Nonforward parton distributions," *Phys. Rev.*, vol. D56, pp. 5524–5557, 1997.

[60] K. Goeke, M. V. Polyakov, and M. Vanderhaeghen, "Hard exclusive reactions and the structure of hadrons," *Prog. Part. Nucl. Phys.*, vol. 47, pp. 401–515, 2001.

[61] P. Hoodbhoy and X. Ji, "Helicity-flip off-forward parton distributions of the nucleon," *Phys. Rev. D*, vol. 58, p. 054006, Jul 1998.

[62] M. Diehl, "Generalized parton distributions," *Phys. Rept.*, vol. 388, pp. 41–277, 2003.

[63] V. Bernard, N. Kaiser, and U.-G. Meissner, "Nucleon electroweak form-factors: Analysis of their spectral functions," *Nucl. Phys.*, vol. A611, pp. 429–441, 1996.

[64] A. Belitsky and A. Radyushkin, "Unraveling hadron structure with generalized parton distributions," *Physics Reports*, vol. 418, pp. 1–387, 10 2005.

[65] L. Mankiewicz, G. Piller, and T. Weigl, "Hard exclusive meson production and nonforward parton distributions," *Eur. Phys. J.*, vol. C5, pp. 119–128, 1998.

[66] X. Ji, "Deeply virtual compton scattering," *Phys. Rev. D*, vol. 55, pp. 7114–7125, Jun 1997.

[67] J. Ashman *et al.*, "An Investigation of the Spin Structure of the Proton in Deep Inelastic Scattering of Polarized Muons on Polarized Protons," *Nucl. Phys.*, vol. B328, p. 1, 1989.

[68] C. Lorce, "Geometrical approach to the proton spin decomposition," *Phys. Rev.*, vol. D87, no. 3, p. 034031, 2013.

[69] A. V. Belitsky and D. Müller, "Exclusive electroproduction revisited: Treating kinematical effects," *Phys. Rev. D*, vol. 82, p. 074010, Oct 2010.